

**Diffuse Optical Spectroscopy Aided Non-Invasive
Intracranial Pressure Estimation and Cerebral
Autoregulation Assessment**

Submitted in partial fulfillment of the requirements for

the degree of

Doctor of Philosophy

in the

Department of Biomedical Engineering

Alexander Ruesch

B.Sc., Medical Engineering, University of Applied Sciences Bremerhaven

M.Sc., Medical Engineering Science, Universität zu Lübeck

Carnegie Mellon University

Pittsburgh, PA

May 2020

© Alexander Ruesch, 2020

All Rights Reserved

Acknowledgments

First, I would like to acknowledge my committee members, who have guided my progress far beyond the expected, and I am thankful for their honest critique, thoughtful suggestions, and great dad-joke-humor:

Jana M. Kainerstorfer
Keith Cook
Matthew A. Smith
Pulkit Grover
Alberto L. Vazquez

I started to work with Jana Kainerstorfer in January 2016, at which point her lab was a mere half a year old. What started as a small group of 3 students at the time I joined, is now one of the largest research groups in the Biomedical Engineering Department at CMU and the journey to this point has been fascinating, exciting, at times tedious but always fruitful. Jana has not only shaped my scientific thinking, my scientific knowledge but also my scientific curiosity. As a true mentor, she understood how to lift my spirit in times of hardship, was the polar opposite to my often critical point of view, and was always interested in my success beyond my work in her group, for which I admire her. Jana allowed me to work on many projects, with many collaborators from the Pittsburgh area and internationally. She showed me the power of research collaborations and the impact a simple idea can have when applied in the right environment. Through her, I got to know numerous fascinating scientists in the field of biomedical optics, which allowed me to make an impact at international conferences, of which there were many. I am grateful to have been given the opportunity to work with her on exciting research, inspiring collaborations.

Among a large number of collaborators, there is one person in particular who I would like to thank the most. When we started to work with Matthew A. Smith, he was a professor at the University of Pittsburgh, working on learning and adaptation in non-human primates. He later joined us at CMU, making collaborations even easier. I came to know Matt as a person open to new ideas and research opportunities, a person of patience, clear words, and the ability to take a step back to see the bigger picture. Not only did Matt enable us to perform non-human primate research, but he was always willing to discuss data quality, data processing, and physiological implications. I enjoyed our regular meetings and can only give my deepest gratitude to him and his lab for enabling my research. In this, I must also thank Samantha Schmitt, Matt's long term lab manager. Sam was a great help in organizing the experimental setups, design contraptions and extract information. No data could have been collected without her. Spending numerous sleepless hours in the surgical environment with Jana, Matt, Sam and my colleagues Jason and Deepshikha, has brought this research group closer together, creating true friendships.

Over the many years spent working in Jana's group I had the opportunity to connect with many fellow graduate students. I hold in high regard my fellow PhD students and true friends, Constance Robbins, Jiaming Cao, Jason Yang, and Deepshikha Acharya. Conni and Jiaming joined Jana's lab before I did and to this day seem to me as the cornerstones of the group. Shortly after me Jason joined, and we connected early on much past the daily work in the lab to soon became housemates. I need to thank Jason especially for the many past midnight discussions on research, politics

and social life that we had in our little house, which I truly enjoyed. Deepshikha joined Jana's group in Fall 2018 and I quickly bonded with her. She helped to keep me sane in many difficult hours and soon became a constant in my life that I do not want to miss in the future. The five of us worked with and never against each other. The true strength of this quintet is the diversity of expertise and personal interests that made this lab flourish and my time here worthwhile. I hope that the friendships I forged here will last a lifetime and that I will be welcome to an occasional CULT meeting past my graduation.

Additionally, I would like to thank the staff of the Biomedical Engineering Department. You all have enabled my research in ways you might not have realized, especially when you were available for silly last minute requests.

I would not be here without the everlasting support of my family and friends back in Germany. My mom, Jutta, showed me what is important in life, beyond career goals and money and showed me how to stay grounded and yet ambitious. My dad, Joachim, taught me analytical thinking, self reflection, and the ability to see the two sides of every story. In every step of the way, my parents supported my personal goals and dreams, never questioning my decisions, always enabling me. It is thanks to them that I became who I am today. *Mama, Papa, vielen Dank für eure Geduld mit dem ewigen Studenten, euer Verständnis für meine Flucht aus Cuxhaven und für die Liebe und Unterstützung die ihr mir zukommen lasst, auch wenn ich tausende Kilometer entfernt bin. Ohne euch wäre ich nicht hier, ohne euch wäre dies alles*

sinnlos. Ich hab euch lieb!

My brother Maximilian has been a constant companion and friend in my life. I owe him for many lessons he unknowingly taught me, first and foremost that sharing and working together is often more profitable than competition. With him, I can always let go and be the goofy kid I used to be, and for that I love him.

I have to thank my grandparent Ernst and Barbara, and Hannelore and Hans. They have raised me when my parents were busy at work and showed me how one can live a humble life in true happiness. *Oma Hannelore, Opa Hans, Oma Bärbel und Opa Sohni, ich danke euch von ganzem Herzen für eure Unterstützung, euer Zusprechen und eure Lehren. Ihr habt meine Kindheit zu einem wunderschönen Erlebnis gemacht und meine Neugierde geweckt.*

I would like to thank my friends in Germany for keeping in touch despite the long distance, for going out of their way to visit me in the US, and to continuously encourage me towards the final goal. Thank you Stefan and Stephanie, Christian and Esther, Dennis and Jenny, and Matze! I hope that these friendships will remain as strong as they are.

Last but not the least I would like to thank Rini for her love and support along this journey. Her constant encouragements, culinary advice, and adventurous spirit have made my life outside the lab worthwhile. She showed me what wondrous things can be found right around the corner of your doorstep and she allowed me to double the excitement by sharing it with her.

This work was financially supported through the Center for Machine Learning and Health (CMLH) Fellowship, the American Heart Association (AHA) 17SDG33700047, and the National Institutes of Health (NIH) R21-EB024675.

Abstract

In many common brain diseases, including traumatic brain injury, stroke, and hydrocephalus, intracranial pressure (ICP) can rise and lead to malperfusion of brain cells and ischemia. Furthermore, the brain's ability to regulate cerebral blood flow despite changes in cerebral perfusion pressure (CPP) can be impaired. Measuring and controlling ICP to maintain a stable oxygen supply to the brain is therefore of high clinical importance. Current devices for ICP measurements are highly invasive and require lumbar puncture or the placement of a catheter into the brain through craniotomy.

This thesis offers alternative methods to measure ICP using non-invasive, diffuse optical devices to gain information about cerebral blood flow and hemoglobin concentration changes in the brain. We propose to use a non-parametric transfer function approach applied to oxygenated hemoglobin concentration changes in the brain to estimate fluctuations of ICP. Additionally, the cardiac pulse shape of cerebral blood flow was found to be associated with quantitative ICP. A machine learning approach is proposed that uses descriptive morphological features of the cardiac pulse to estimate the underlying ICP. We were able to show that the proposed methods perform well in non-human primates under controlled manipulations of ICP and arterial blood pressure.

The non-invasive ICP assessment further allows for cerebral autoregulation assessment, which otherwise often requires invasive ICP recordings. In order to demonstrate this, we performed a non-human primate study where we were able to show

that impaired cerebral autoregulation is largely driven by CPP, which is a function of blood pressure and ICP, further highlighting the need for non-invasive ICP measurements. The discussed methods have the potential to create a lasting impact on ICP acquisition, not only for intensive clinical care, but also for currently inaccessible research on healthy volunteers. Lastly, a clinical translation to the pediatric intensive care is discussed and preliminary results of translation to human subjects are presented. The methods developed in this thesis have the potential to eliminate the need of invasive ICP sensors and therefore may help clinical decision making for treatment guidance in a variety of diseases.

Contents

- Acknowledgements** **iii**

- Abstract** **ix**

- List of Tables** **xvii**

- List of Figures** **xxi**

- 1 Introduction** **1**
 - 1.1 Cerebral Fluid Dynamics 5
 - 1.1.1 Cerebrospinal Fluid Anatomy and Physiology 5
 - 1.1.2 Monro Kellie Doctrine 7
 - 1.1.3 Intracranial Pressure 8
 - 1.1.4 Cerebral Perfusion Pressure 10
 - 1.1.5 Clinical Significance 12
 - 1.1.5.1 Traumatic Brain Injury 12
 - 1.1.5.2 Hydrocephalus 13
 - 1.1.5.3 Other Diseases with Intracranial Pressure Changes 14

1.1.6	Measurement of Intracranial Pressure	15
1.1.6.1	Invasive Measurements	17
1.1.6.2	Non-Invasive Measurements	22
1.2	Cerebral Autoregulation	26
1.2.1	Mechanism of Cerebral Autoregulation	27
1.2.1.1	Control of Vascular Tone	31
1.2.1.2	Control of Capillary Tone	32
1.2.1.3	Neurogenic Control	32
1.2.1.4	Effects of Blood Gas Levels	33
1.2.2	Clinical Significance	34
1.2.2.1	Traumatic Brain Injury	35
1.2.2.2	Hydrocephalus	35
1.2.2.3	Stroke and Hemorrhage	36
1.2.2.4	Other Conditions and Diseases on Cerebral Autoregulation	37
1.2.2.5	Anesthetics and Other Drugs	38
1.2.3	Assessment of Cerebral Autoregulation	39
1.2.3.1	Static Autoregulation	40
1.2.3.2	Dynamic Autoregulation	40
1.2.3.2.1	Cross-Spectral Analysis	43
1.2.3.3	Pseudo Dynamic Autoregulation	48
1.3	Conclusion	50

2 Optical Imaging for Cerebral Applications 51

2.1	Introduction to Biomedical Optics	52
2.1.1	Optical Nomenclature	54
2.1.2	Optical Properties of Tissue	55
2.2	Diffuse Optics and Tissue Interaction	59
2.2.1	Diffuse Light	59
2.3	Near-infrared Spectroscopy	63
2.3.1	Light Absorption in Non-Scattering Medium	64
2.3.2	Modified Beer-Lambert's Law	65
2.3.3	Multi-Distance Approach	67
2.3.4	Hemoglobin Concentration Calculation	72
2.4	Diffuse Correlation Spectroscopy	74
2.4.1	Electric Field Auto-Correlation	74
2.4.2	Intensity Auto-Correlation	76
3	Non-Invasive Measurement of Intracranial Pressure	81
3.1	Estimation of Intracranial Pressure Fluctuations	82
3.1.1	Materials and Methods	83
3.1.1.1	Animal Model and Intraparenchymal Pressure Probe Placement	83
3.1.1.2	Near Infrared Spectroscopy for Extracranial ICP Measurements	85
3.1.1.3	Signal Processing	87
3.1.1.4	Transfer Function Analysis	89
3.1.2	Results	90
3.1.3	Discussion	98

3.1.4	Conclusion	102
3.2	Quantification of Intracranial Pressure Baseline	102
3.2.1	Materials and Methods	104
3.2.1.1	Diffuse Correlation Spectroscopy	104
3.2.1.2	Experimental Design	105
3.2.1.3	Signal Processing	107
3.2.1.4	Feature Extraction	109
3.2.1.5	Machine Learning	111
3.2.2	Results	112
3.2.2.1	Data Acquisition	112
3.2.2.2	Waveform Extraction	112
3.2.2.3	Regression Forest Learner	113
3.2.3	Discussion	118
3.2.4	Conclusion	123
3.3	Combination of Intracranial Pressure Fluctuation and Baseline Prediction	123
4	Quantification of Cerebral Autoregulation Impairment	127
4.1	Materials and Methods	128
4.1.1	Diffuse Correlation Spectroscopy	129
4.1.2	Experimental Setup	129
4.1.3	Experimental Design	130
4.1.4	Signal Processing	132
4.1.4.1	Static Autoregulation	132

4.1.4.2	Dynamic Autoregulation	133
4.1.4.3	Pseudo-Dynamic Autoregulation	133
4.2	Results	134
4.2.1	Static Autoregulation	134
4.2.2	Pseudo-Dynamic Autoregulation	138
4.2.3	Dynamic Autoregulation	139
4.3	Discussion	140
4.4	Conclusion	143
5	Clinical Translation	145
5.1	Clinical Setup	146
5.2	Measurement Protocol	147
5.3	Signal Processing	149
5.4	Preliminary Results	150
5.5	Discussion	152
6	Summary	153
	Glossary	157
	Bibliography	161

List of Tables

3.1	Defined order and number of full rounds of each induced frequency.	88
3.2	Morphological features extracted from cardiac pulsation in ΔCBF	110

List of Figures

1.1	Cerebrospinal Fluid Circulation	6
1.2	Monro-Kellie Doctrine Examples in Disease	8
1.3	Invasive Intracranial Pressure Monitoring Options	18
1.4	External Ventricular Drain for ICP Measurement	19
1.5	The Circle of Willis	28
1.6	Blood Vessel Composition	29
1.7	Lassen’s Curve	41
1.8	Autoregulation Index	43
1.9	Autoregulation Transfer Function Analysis	46
1.10	Phase Delay under PEEP	47
1.11	Optimal Cerebral Perfusion Pressure	49
2.1	Light Interaction with Biological Tissue	60
2.2	Light Propagation in Scattering vs Non-Scattering Medium	63
2.3	Frequency Domain Multi-Distance NIRS	69
2.4	Molar Extinction Coefficient of Hemoglobin	72

2.5	Diffuse Correlation Spectroscopy	77
3.1	Non-Invasive ICP Monitor Concept	82
3.2	Experimental Setup for ICP Fluctuation Measurement	83
3.3	All ICP measurements for estimation of ICP fluctuations.	86
3.4	Schematic of Narrow Band-Pass Filtering of ICP Oscillations.	88
3.5	Spectral Power of ΔHbO and ICP_{ip} during ICP oscillations.	91
3.6	Example Measurement for ICP Fluctuation	93
3.7	Magnitude Comparison of Induced Oscillations in ΔHbO and $\Delta\text{ICP}_{\text{ip}}$	94
3.8	Signal-To-Noise Ratio of induced oscillations in ICP.	95
3.9	Bode Plot of ICP_{NIRS} Transfer Function	96
3.10	Comparison of estimated ICP_{NIRS} to measured ICP_{ip}	97
3.11	Experimental Setup for CBF Measurement in Non-Human Primated	106
3.12	Example Data for Pulsatile Recordings of ICP, ABP, and ΔCBF	113
3.13	Cardiac Pulse Changes in ICP, ABP, and ΔCBF under ICP Change	114
3.14	ICP Offset Estimation Performance	118
3.15	Non-Invasive ICP Monitor Proof of Concept	125
4.1	Cerebral Autoregulation Experimental Setup	131
4.2	Cerebral Autoregulation Example Measurement	135
4.3	Lassen's Curve Under Isoflurane and Fentanyl	138
4.4	Pressure Reactivity Index Under Isoflurane and Fentanyl	138
4.5	ABP to ICP Phase Delay Under Isoflurane and Fentanyl	139

5.1	Clinical Setup and Probe Design	147
5.2	Preliminary Results of ICP Fluctuation Estimation	151

Chapter 1

Introduction

According to the Centers for Disease Control and Prevention, approximately 2.87 million traumatic brain injury (TBI) related emergency department visits, hospitalizations, and deaths were reported in the United States in 2014 alone [1]. The American Heart Association in conjunction with the Centers for Disease Control and Prevention report that 795,000 people experience a stroke in the United States every year [2]. Approximately one million Americans are affected by hydrocephalus, across all age groups and socioeconomic backgrounds [3]. Furthermore, hydrocephalus is the most common reason for brain surgery in children [3]. These are only three of the most common brain injuries in which information about intracranial pressure (ICP) and the brain's ability to regulate blood flow, known as cerebral or cerebrovascular autoregulation (CA), is helpful to improve patient outcome.

Measurement methods of CA often require the knowledge of arterial blood pressure (ABP) and ICP [4], increasing the importance for ICP measurements further. However, current standards for measuring ICP are highly invasive and require either a lumbar puncture or the placement

of a catheter or a pressure transducer inside the skull [5]. This high degree of invasiveness is the reason why measurements of ICP in less severe cases are not applied and data from healthy volunteers for research applications is not available. Opinions about the use of CA and ICP to improve patient outcome vary, likely due to the lack of standardized treatment across hospitals and countries, but also due to missing healthy volunteer reference studies.

From this deficit arises a clinical need for non-invasive ICP measurement methods for clinical use and research alike. Furthermore, the need for healthy subject reference measurements of CA under varying hydrocephalus, TBI, and stroke like conditions is needed, to confirm or reject hypotheses made by clinical research based on patient data. Many groups have attempted to measure ICP non-invasively [5, 6], but currently available methods are lacking the simplicity of use, bedside compatibility or temporal resolution to find their way into daily routines in the clinic [6].

In this thesis a leap towards non-invasive ICP measurements is made by using diffuse optical devices that utilize non-ionizing near-infrared light to illuminate the human tissue and derive vital information like blood flow, blood volume, blood- and tissue-oxygenation and more. Modelling the hemodynamics in the brain by means of machine-learning will allow me to build the connection between vital hemodynamic signals and underlying ICP. Furthermore, it is shown how common CA evaluation techniques perform in the controlled environment of a healthy non-human primate model under hydrocephalus like conditions to address the need of healthy volunteer reference measurements.

First, an outline of the physiology of blood and cerebrospinal fluid circulation in the brain

(Chapter 1.1) is given, to establish an argumentation basis on which physiological implications of later non-invasive ICP measurement techniques will rely. The need in severe brain diseases to measure ICP is shown and an understanding for the reader for current clinical practice and arguably healthy parameters that are targets in modern treatment practice, specifically for traumatic brain injury, hydrocephalus and stroke is given in Chapter 1.1.5. With such diseases in mind, invasive and non-invasive ICP monitors are discussed in Chapter 1.1.6. For the second goal of this thesis, the evaluation of cerebral autoregulation, a detailed description of which is given in Chapter 1.2. This includes an outline of common measurement methods and the classification of measurement methods used in this manuscript.

To understand the methodology and sensitivity of near-infrared spectroscopy and diffuse correlation spectroscopy, a detailed introduction into diffuse optics is given in Chapter 2. This includes a brief description of the conditions and assumptions necessary to allow the derivation of hemoglobin concentrations (Chapter 2.3) and cerebral blood flow (Chapter 2.4) in turbid media like human tissue.

Chapter 3 will discuss our work to create non-invasive ICP measurement algorithms on the basis of diffuse optical devices. The measurement of fluctuations, or relative changes in ICP are discussed in Chapter 3.1, where a transfer function fitting was applied to the hemodynamic response in oxygenated hemoglobin concentrations to ICP oscillations, and show that a good agreement between invasively measured and estimated ICP exists. Furthermore, an outline of the experimental and computational procedures necessary to estimate baseline ICP values, or the ICP offset to fluctuations, is given in section 3.2. Here, diffuse correlation spectroscopy was used to measure the cardiac pulsation in cerebral blood flow, which undergoes morphological alternations as

a result of increased impedance inside the skull due to ICP changes. A regression forest based machine learning approach is used to relate the shape of these cardiac pulsations to ICP.

To aid the need for unified cerebral autoregulation standards, which might improve patient outcome in numerous cerebral diseases, the application of common autoregulation evaluation techniques in the controlled environment of healthy non-human primates undergoing anesthesia induced cerebrovascular autoregulation impairment is described. The results in Chapter 4 highlight the necessity to measure ICP and emphasize that arterial blood pressure might not be a good sole indicator of intact brain perfusion control.

Chapter 5 attempts to translate the achievements from Chapters 3 and 4 into the clinical environment of pediatric intensive care. For this ongoing project an explanation of the setup and process of data collection is given and preliminary results that show a correlation of invasive ICP fluctuations and hemoglobin concentration based estimates is given.

The studies presented in this thesis will aid not only the large population of severely injured patients but will further open up the field of ICP measurements to healthy volunteer studies, which in turn will help us to better understand brain physiology and the effects of cerebral autoregulation on brain health and patient outcome. The key contribution of this thesis is the development of computational tools and their verification in animal models for non-invasive ICP assessment.

1.1 Cerebral Fluid Dynamics

To understand the dynamics of cerebral blood flow (CBF) and its interplay with cerebrospinal fluid (CSF) production, absorption and its dynamics, we need to understand the balance of volumes in the skull and their relationship to pressure changes. A popular model for this balance is the Monro-Kellie doctrine or hypothesis. Then we can understand the role of ICP and ABP on the oxygen delivery to the brain and their importance in the CBF autoregulatory system.

1.1.1 Cerebrospinal Fluid Anatomy and Physiology

To grasp the mechanical connections between CA and ICP, the anatomy and physiology of CSF production and uptake should be discussed. As shown in Figure 1.1, CSF is produced in the brain's ventricles predominantly by the choroid plexus inside the lateral ventricles. The CSF flows further into the 3rd, *via* the interventricular foramina, and 4th ventricle, *via* the cerebral aqueduct, to then be distributed into the spinal cord and the subarachnoid space (SAS) through the central, median and two lateral apertures. The CSF flow is always outward inside the ventricles but can be multidirectional in the SAS. CSF is suspected to act in this space as a support and shock protection. It reduces the effective weight of the brain through buoyancy, regulates ICP, and performs other minor tasks. Its role in transport of hormones and clearance of proteins and waste products is still widely debated. The fluid is then reabsorbed in the arachnoid villi and transported off through the superior sagittal veins.

This so called "third circulation" is a traditional model introduced by Harvey Cushing in 1923 [8]. While this model is to date widely accepted, many groups have started to present alternative

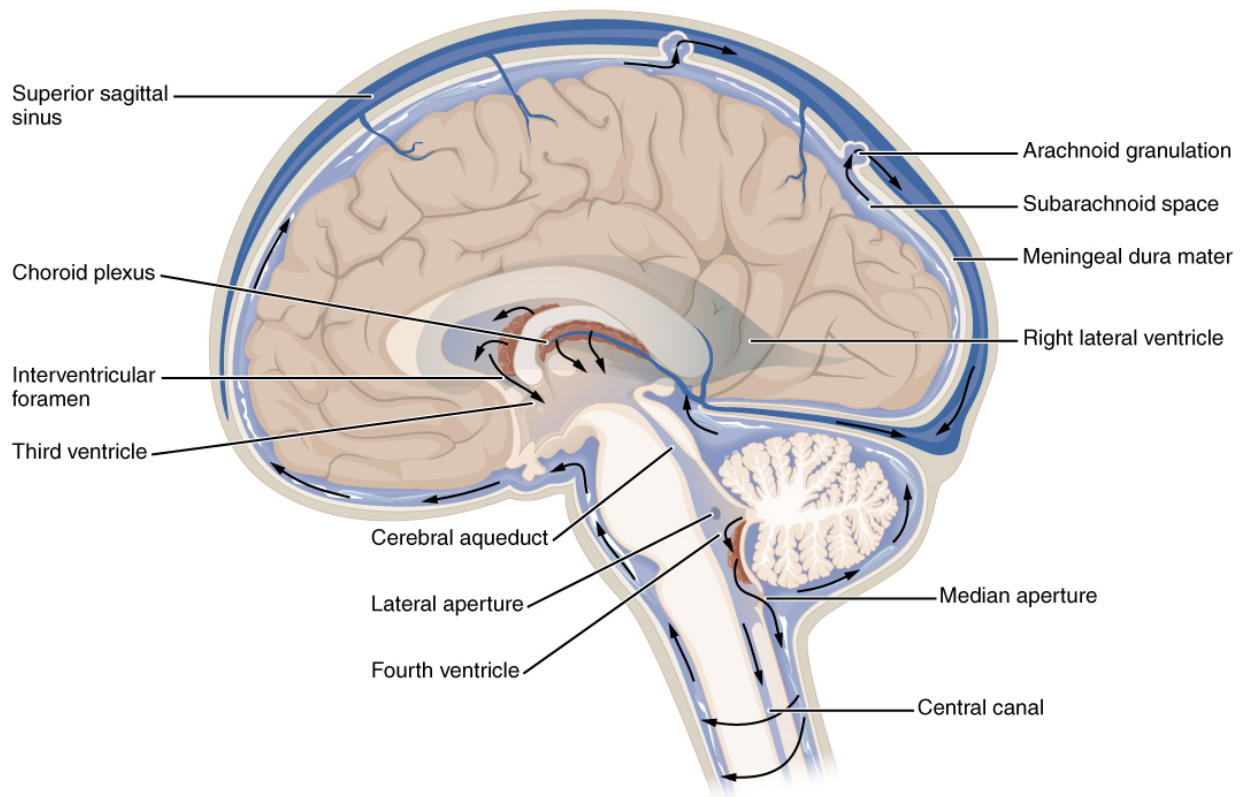


Figure 1.1: The brain tissue is shown in a beige color, the arterial vessels releasing the cerebrospinal fluid (CSF) are colored in red while the CSF itself is colored in blue. Arrows indicate the direction of CSF flow: The CSF is produced predominantly in the choroid plexus, circles the brain through the subarachnoid space and reabsorbed by the sagittal sinus. Figure taken from wikipedia.org [7].

models [9–11]. Especially the advent of microscopic observations and the discovery of additional components like aquaporin has sparked new debates [9]. Although it now seems true that Cushing’s model is a vast simplification of the fluid circulation in the brain, the magnitude of other CSF influencing components needs to be quantified before the old model can be proven wrong or insufficient by modern research. This view is shared with recent review articles on CSF circulation and the Monro-Kellie Doctrine [9, 11]. Thus, the simplified model by Cushing will be the basis of argumentation in this thesis for deriving conclusions on ICP changes and CA activity.

1.1.2 Monro Kellie Doctrine

Named after studies of the Edinburgh physicians Alexander Monro (1783) [12] and his student George Kellie (1824) [13], who first described the skull as a rigid structure with fixed volume, it was Harvey Cushing who founded the modern version of the Monro-Kellie Doctrine in 1923 [8]. The Monro-Kellie Doctrine states that the volume inside the skull is constant, and if one of the major compartments (blood, CSF, or brain tissue) changes, the remaining two have to compensate or ICP will rise. Ever since, the general idea has not been changed, but adjustments have been made. One such adjustment is that blood volume changes play a larger role in the volume and pressure regulation in the brain due to their faster and larger response compared to CSF production and uptake [11]. Under the adapted theories, the most influential volumes are the venous blood compartment, the arterial blood compartment, the CSF compartment and the brain tissue (see Figure 1.2A). Additional volumes can be added in case of tumor growths, brain swelling, or edema. In case of hydrocephalus for example, an excessive amount of CSF is

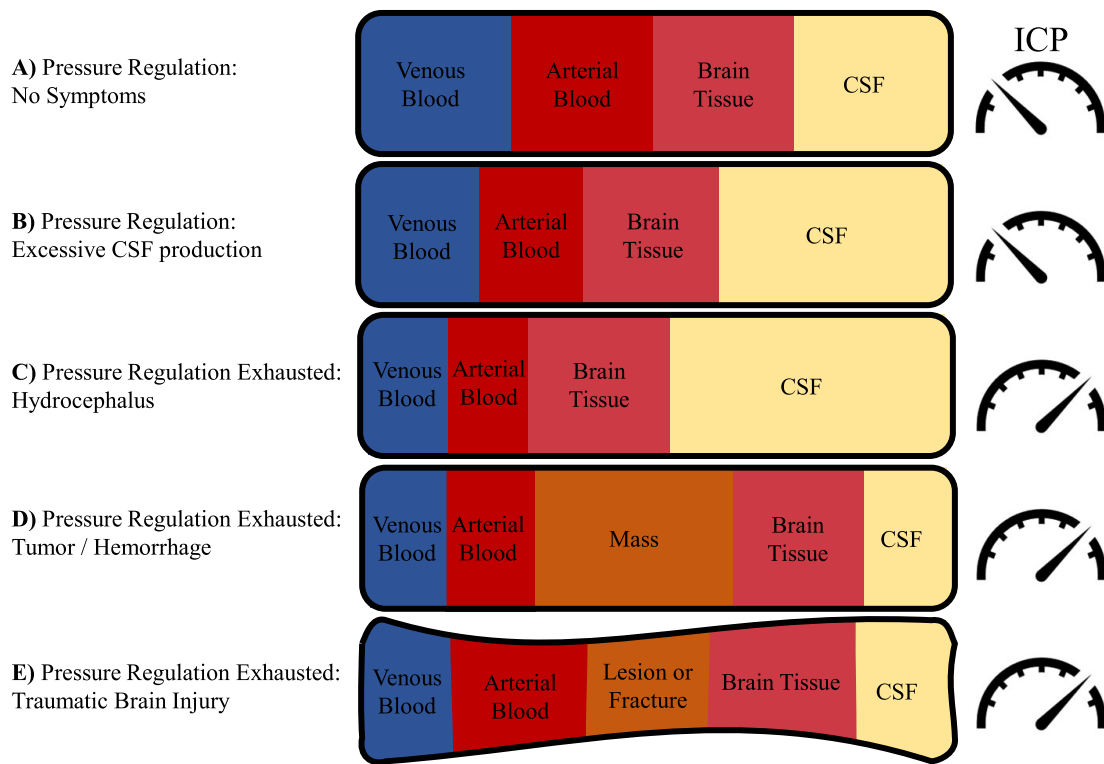


Figure 1.2: The compartments of the largest volumes in the brain, i.e. blood, CSF, and the brain, are shown. The pressure gauge on the right-hand side of every figure indicates the ICP in the brain, where a low pressure is healthy, and a high pressure is experienced upon pressure regulation failure. The top graph shows a healthy brain under no injuries or diseases. CSF and venous blood are reduced in the following disease states due to a significant change in the balance of volumes or due to additional volumes.

produced. If this additional fluid is not exhausting the compensatory capabilities of venous and arterial blood reduction, the ICP stays normal (Figure 1.2B). If the additional fluid overwhelms the autoregulatory system, ICP will rise (Figure 1.2C). This is also true for other diseases in which a new volume is introduced, or the skull is fractured and deformed (see Figures 1.2D-E).

1.1.3 Intracranial Pressure

Intracranial Pressure (ICP) is the pressure inside the human skull and largely determined by the volume balance described by the Monro-Kellie doctrine. A normal ICP in adults is expected to be

approximately 10 - 15 mmHg, with occasional short-term increases due to coughing or sneezing [14, 15]. Longer term (≥ 5 min in children [16] and ≥ 15 min in adults [17]) increases above 20 mmHg are considered pathological [14, 18] and have been correlated to worse patient outcome after disease [19, 20]. The normal ICP value is lower for children (3 - 7 mmHg) and infants (1.5 - 6 mmHg), depending on age [15]. A threshold for a significantly malignant elevation of ICP is not agreed upon, with values reported between 15 mmHg and 35 mmHg [21], and yet there is sufficient evidence that $ICP > 20$ mmHg in pediatric care that correlates with poor outcome [20]. Changes in ICP can occur throughout our daily life, including coughing, sneezing, and posture changes. In a standing up motion, ICP can temporarily drop significantly and even measure negative values without signs of discomfort [22]. There is however an number of diseases in which ICP is permanently increased, including hydrocephalus [23], traumatic brain injury [24, 25], idiopathic intracranial hypertension [26], stroke [27, 28], and others. Countermeasures have to be put into place to avoid secondary injuries such as hypoxia and ischemia. The most relevant injuries for work in this thesis are further discussed in Chapter 1.1.5.

Signs of elevated intracranial pressure include but are not limited to:

- strong headache,
- vomiting,
- blurred vision and vision loss,
- behavioral changes and low alertness,
- nausea,
- tinnitus,
- weakness or problems with moving or talking,
- depression,

and is often confirmed by radiology through magnetic resonance imaging (MRI) or computed tomography (CT) to observe enlarged cerebral ventricles filled with CSF or other signs of volume

increases such as tumors or blood pooling [29, 30]. Measurements of ICP are highly invasive, they often require craniotomy or placement of a spinal tap, and are therefore only performed under certain circumstances in which the benefit outweighs the surgical risk. In 1960 Lundberg was the first to report an organized measurement of ICP in patients of various cerebral injuries. He found three distinct spontaneous fluctuations in ICP, which are today known as the Lundberg A, B and C waves, describing plateau waves of 5 - 20 minutes, 0.5 - 2 minutes, and every 10 seconds, respectively. The A waves have been associated to cerebral compliance and impending herniation, while C waves are associated to coronary-pulmonary coupling, and thus might mostly reflect respiration [31]. The origin of Lundberg B waves on the other hand is still subject to debate. B waves were observed in healthy subjects, ventilated patients and during sleep [31]. With a delay of a few decades, ICP monitoring became a part of the standard care for severe TBI when it was added to the guidelines for brain trauma in 1995 [32]. More information on the risks and methodology of ICP measurements is presented in Chapter 1.1.6.

1.1.4 Cerebral Perfusion Pressure

The human brain resides inside an enclosed environment formed by the skull, encasing it in a unique pressure environment in which blood perfusion is not only determined by ABP, but also by ICP. More specifically, ICP modulates the venous sinus pressure that determines the blood return to the heart. The pressure gradient from arterial to venous pressure is the driving force for blood flow. Similarly in the skull, venous sinus pressure is approximately equal to ICP, which leads to the clinically used simplification that cerebral perfusion pressure (CPP), which drives the blood flow in the brain, can be estimated as the pressure difference between mean ABP (MAP)

and mean ICP (\overline{ICP} in Equation 1.1) [33]

$$CPP = MAP - \overline{ICP}. \quad (1.1)$$

Given a MAP for adults of 70 to 100 mmHg and a typical ICP of 10-15 mmHg, a typical CPP value in adults is anywhere between 55 and 90 mmHg. Children and infants have age dependent smaller MAP and ICP. Typical CPP values for infants can therefore be as low as 30 - 40 mmHg, while older children can reach adult values (≥ 12 years of age) [34].

CPP raises particular interest in the context of CA (see Chapter 1.2). Here it is often used to relate other CA evaluation methods to the current state of the patient. The Lassen's curve for example shows CBF as a function of CPP, which in a healthy subject shows a clear plateau of largely unchanged CBF despite changes in CPP as CA is intact. The pressure reactivity index, a moving correlation between MAP and ICP, can be used to find an optimal CPP value for ideal CA activity in TBI patients that can be used as a target in patient treatment [35] (see Chapter 1.2.3). Because CPP relies on measurements of ICP, it is not readily available in clinics and bound to similar restriction as ICP measurements. CPP is a combination of equal weights between MAP and mean ICP. MAP is about one magnitude larger and therefore the dominant influence. For practical reasons in case of unavailable ICP information, autoregulatory assessments are sometimes only related to MAP, missing the influence of ICP. The relevance of this will be discussed in Chapter 4.

1.1.5 Clinical Significance

Measurements of ICP can make a significant difference in the long-term outcome of patients under many diseases, including TBI, hydrocephalus, and stroke. In severe cases, interventions to regulate ICP are necessary and can be performed, depending on the disease or injury, in invasive and non-invasive ways. In all the below diseases, radio-graphic evidence in combination with a minimum Glasgow Coma Scale (GCS) value of often ≤ 8 are used to indicate the need for ICP measurements [16, 17]. These strict limitations are set in place to ensure that the risk of measurement is lower than the potential benefit this additional monitoring methods can give.

This emphasizes the importance and the potential impact that a less invasive ICP sensor can have on modern medicine. It should be noted that measurement and regulation of ICP are often, but not always, part of the same intervention, due to the common use of intraventricular catheters, which can both drain CSF and measure ICP through the same craniotomy. The implications for ICP measurements in the most relevant ICP alternating diseases is given below.

1.1.5.1 Traumatic Brain Injury

Traumatic brain injury (TBI) is defined as a severe injury of the head, often caused by impacts such as bumps, blows or jolts to the head or in the form of a penetrating head injury. Mild impacts can lead to a temporary change of mental state or consciousness. TBI with severe injuries leads to an extended period of unconsciousness or amnesia after the injury [1]. Injuries are most often caused by falls (approx. 50 %). Other causes are being struck by or against objects, motor-vehicle crashes and intentional self-harm. TBI is a major cause of death in the United States, where in 2014 alone an average of 155 people died from TBI related injuries every day [1]. Sur-

vivors can face impairments related to thinking and memory, movement, vision or hearing, and emotion, such as depression or personality change.

After initial critical or surgical care to address the individual's acute injuries, severe TBI patients are often moved to the intensive care unit to recover. In some cases, it is necessary to regulate ICP and CPP, to maintain a stable blood perfusion of the brain, as CA can be impaired or exhausted due to tissue swelling, fractures or excessive CSF piling, leading to dilation of the lateral ventricles. First studies suggest that TBI treatment based on individualized CPP or ICP treatment is correlated with favorable outcome, and that it performs better than literature-based thresholds [36]. Current treatment guidelines for TBI have suggestions to maintain CPP above 60 - 70 mmHg in adults [17] and above 40 - 50 mmHg in children [16].

1.1.5.2 Hydrocephalus

Hydrocephalus is defined as an abnormal accumulation of CSF in the cavities of the brain [3]. Hydrocephalus can be congenital, i.e. one can be born with it through genetic defect or fetal development disorder, or one can acquire it at a later age. It is further differentiated into communicating hydrocephalus and non-communicating hydrocephalus. Communicating hydrocephalus is an obstruction of the CSF after it has exited the ventricles. It is called communicating due to its ability to exchange fluid between the cerebral ventricles. A non-communicating hydrocephalus, also called obstructive hydrocephalus, occurs when an obstruction of the inter ventricular pathways is given, preventing CSF to flow from the ventricles outward, for example due to aqueductal stenosis [37]. Two further categories are hydrocephalus ex-vacuo and normal pressure hydrocephalus (NPH). Hydrocephalus ex-vacuo describes CSF accumulations in areas where the brain

tissue has shrunk, often by TBI or stroke, but also as a result of age or Alzheimer's disease, to fill the space. NPH is a disease of abnormal CSF increase as an effect to subarachnoid hemorrhage, head trauma, infection, tumor or surgery complications or idiopathic, causing a blockade to CSF-draining pathways. NPH shows no signs of increased ICP and is estimated to affect approximately 375,000 elderly Americans [38].

All hydrocephalus categories, with the exception of NPH, can show increases in ICP that can, if untreated, lead to typical ICP elevation symptoms and further to ischemia and death. A standard procedure to reduce ICP is to drain CSF by implanting a shunt that drains the fluid from the ventricles in the brain into the abdomen. Another option is an endoscopic third ventriculostomy, where a surgeon punctures the membrane in the floor of the third ventricle to create an additional pathway for CSF flow. One last option is the ablation of parts of the choroid plexus to reduce the CSF production rate. [39]

It is apparent that knowledge of ICP in hydrocephalus is fundamental to regulate blood perfusion of the brain and adjust temporary as well as permanent surgical interventions to regulate CSF flow and CPP.

1.1.5.3 Other Diseases with Intracranial Pressure Changes

ICP can be increased to malignant levels through diseases such as ischemic and hemorrhagic stroke, inflammatory diseases such as meningitis or, if no further reason can be found, idiopathic intracranial hypertension, formerly known as pseudotumor cerebri. The name pseudotumor cerebri was chosen due to its similar symptoms to a brain tumor, yet it is defined as an increase in ICP without known causality.

Ischemic strokes are often resolved by reopening the pathway for blood flow after an occlusion. While lesion and infarct regions stop spreading after the intervention, an early neurological deterioration can occur within 24-48 hours following the acute ischemic stroke. This neurological deterioration is associated with poor outcome [40]. Early studies show that the neurological degeneration is caused by an increase in ICP after stroke [27, 41].

Intracerebral hemorrhage describes the growth of a hematoma inside the brain that can, given a certain volume, elevate ICP. In this case, standard ICP lowering interventions, such as hyperventilation and an upright posture, as well as surgical intervention, are needed [42].

Meningitis describes the inflammation of the meninges, which are the three membranes covering the central nervous system, including the spinal cord. It is usually caused by a viral infection, but bacterial and fungal causes are possible. While an inflammation based lesion can easily be associated with increased ICP, many more pathways for ICP increases triggered by meningitis have been identified in the past, including hydrocephalus, loss of CA, and impairment of the blood brain barrier [42]. A detailed overview for these causalities is beyond the scope of this work but can be found elsewhere [42].

1.1.6 Measurement of Intracranial Pressure

The number and severity of diseases influencing ICP show that a vast number of patients is affected by injuries that lend themselves to measurements of ICP, to observe treatment development and to make treatment decisions. While this can have benefits for patient outcome, measurement methods are often invasive and therefore only used with caution. Detailed information on ICP

measurement is offered in this section.

While the concept of ICP was known since at least Cushing's report on the Monro-Kellie doctrine in 1923 [8], the first reported measurement of ICP was done by Guillaume and Janny in 1951 [43]. Back then, a U-tube was used and connected to a ventricular catheter to determine ICP by observing a halt in the CSF outflow at the point of too large backpressure. A more common name in conjunction with the first clinical ICP measurements is Nils Lundberg, who in 1960 established a routine to measure ICP in neurosurgical practice [44], using a ventricular catheter, a string gauge pressure transducer and an ink-writing potentiometer recorder, and soon after reported on first clinical results in TBI [45], in which ICP monitoring is a standard procedure since 1995 [32].

Today's ICP monitors record pressure either as standalone pressure transducers or in combination with an external ventricular drain (EVD) from the brain, or alternatively measure the pressure from a remote location in the spinal cord through lumbar puncture. First approaches have been reported that try to measure ICP non-invasively, using a variety of devices such as ultrasound sonography, computed tomography, near-infrared spectroscopy, diffuse correlation spectroscopy and many others. Despite the variety of non-invasive alternatives, the gold standard as of today is still invasive. This is likely due to the signal quality and resolution of invasive devices, that are unmatched by alternative devices that further lack in accuracy, ease of use, or bedside compatibility. A comprehensive overview of invasive and non-invasive ICP measurement devices is listed below, to grasp the far and wide of this competitive field.

1.1.6.1 Invasive Measurements

Measuring intracranial pressure invasively is to this day the gold standard, but advances in the measurement method have been made since the early days of Lundberg's ICP measurements in the 1960s. The most common measurement today is still the placement of a ventricular catheter into the lateral ventricle of the brain, as it allows to drain and measure ICP through one single craniotomy. The intraparenchymal pressure transducer is likely number two. ICP can also be measured epidurally and subdurally, directly from the head (see Figure 1.3a). If CSF is communicating between the ventricles, lumbar puncture can be used to measure ICP (Figure 1.3b). Recently, telemetric, implantable devices have made it to the market, that allow continuous measurements of ICP for days without a direct connection of the head to a device via electric or fiber optic cable or an EVD. One example is shown in Figure 1.3c.

Intracranial ICP Monitoring The most commonly used ICP monitor is a pressure transducer that is attached to a catheter leading into one of the ventricles through a burr hole (see Figure 1.4) [48]. This EVD based design additionally allows for CSF draining and administration of medicine, such as antibiotics, intrathecally, i.e. into the CSF [48]. Due to the incompressible nature of CSF, that consists mainly of water, the pressure transducer reading through EVDs are very accurate and can be of high sampling rates and resolution. An external calibration and recalibration of EVDs already in place count towards further benefits of this method, which can further avoid baseline drifts [31]. The major draw backs however are the risk of infection (in approx. 11% cases), post-operative hemorrhages (5.7%), the formation of edema, and bacterial colonization of the catheter, but reported likelihoods vary [31, 48].

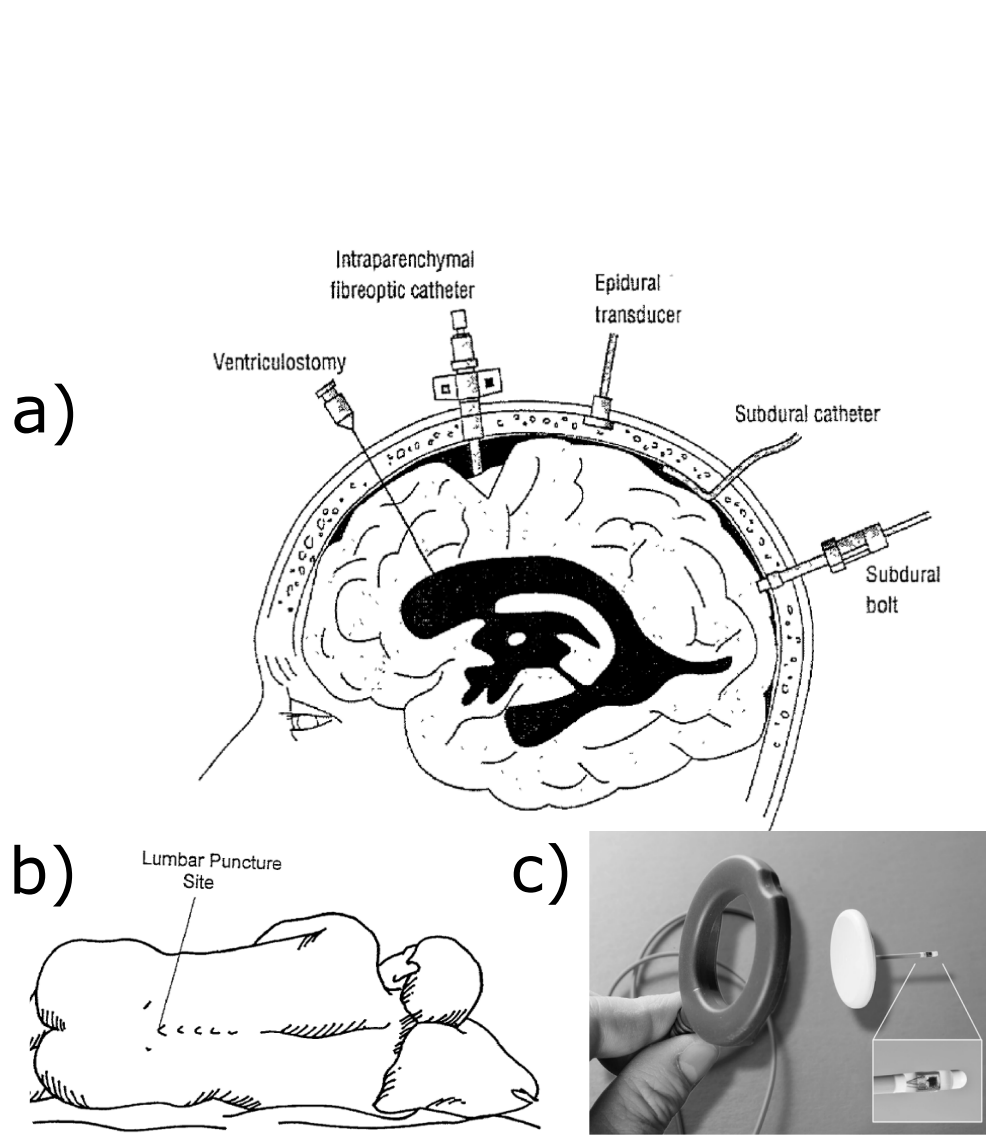


Figure 1.3: Illustration a) various invasive types of invasive ICP monitors for the head are shown in a cross-section of the head, showing the degree of invasive intervention necessary. b) shows the position of the human body preferred for lumbar puncture. ICP can be measured by placement of a spinal tap. In illustration c) the Raumedic Neurovent P-tel is shown, an implantable, telemetric ICP monitor with pressure sensor and transmitter (right) and the radio frequency power supply and receiver (left). Illustration a,b taken from [46], photography in c taken from [47].

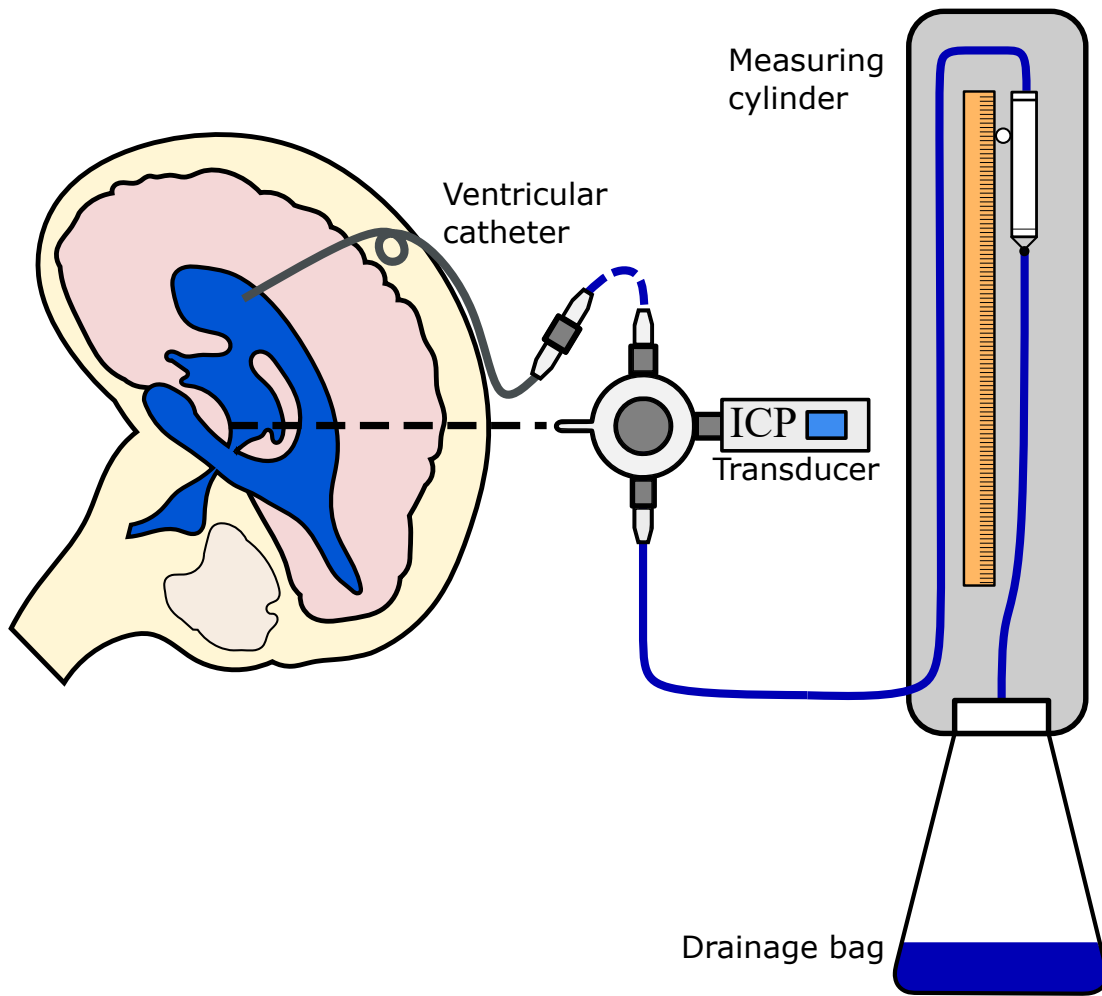


Figure 1.4: The external ventricular drain (EVD) for is connected to a drainage bag. The height of the measuring cylinder determines the ICP at which CSF is drained. The drain can be blocked of via a stopcock to measure the pressure inside the EVD via a pressure transducer. Draining and ICP measuring are exclusive.

Intraparenchymal pressure sensing devices can have a variety of mechanisms. Fiber optic based devices shine light on a movable mirror. The mirror is moved due to applied pressure and the reflected light intensity change can be used to measure this displacement and translate it into a pressure value. Strain gauges such as piezo-elements return a resistance changes in an electric circuit, depending on the applied mechanical stress originating from ICP, which can be measured and correlated to ICP values. A third method is to use a small balloon at the distal end of the device, in which air pressure can be measured [48]. Parenchymal probes bear a lower risk of infection and offer easier placement, which puts them at a slight advantage over catheters, but suffer from baseline drifts and can only be calibrated before placement into the brain [31]. Additionally, parenchymal probes measure a local ICP, due to pressure gradients across the brain tissue, while EVDs measure the global ICP inside the ventricles.

Epidural and subdural pressure transducers are rarely used, as they have proven to be unreliable in clinics [31, 48].

Lumbar Puncture Manometry If CSF is communicating, i.e. if the flow of CSF from the ventricle outward is not obstructed, ICP can be measured in the spinal cord via lumbar puncture. Once the spinal tap is placed and CSF can flow out into the catheter, the measurement technique is similar to the EVD in that an external pressure transducer can be used. The lumbar drainage is superior to the EVD in reduced invasiveness and simplicity of application. However, it is limited by communicating CSF and the posture of the patient [49].

Given an unobstructed flow, lumbar puncture derived ICP and EVD measured ICP correlate very well for baselines, while cardiac pulsatile information shows a much lower amplitude at a longer

delay from diastolic minimum to systolic maximum in the spinal cord ICP. [49]

Implantable Devices All the above methods are tethered methods in the sense that the patient is connected externally to a recording device. For long-term and outpatient monitoring, untethered implantable devices are available, that send the information about ICP wirelessly to a receiver unit, which can be useful in the long-term observation of hydrocephalus patients and to monitor shunt-failure [31].

The Raumedic Neurovent P-tel (Helmbrechts, Germany) is a telemetric version of the intraparenchymal micro-transducer. The implantable part is rested on top of the skull and held in place by the closed scalp above it. A 4 cm long needle with a piezo-element based pressure sensor is inserted into the brain tissue. A micro-chip in the circular top (see Figure 1.3c) converts the resistance change into a pressure value. The device is powered by the external antenna that generates an alternating electric field at radio frequencies, which allows both powering of the pressure sensor and data transmission [47].

A different approach for telemetric ICP monitoring is offered by the OSAKA telesensor (Nagano Keiki Seisakusyo Co. Ltd., Tokyo, Japan), which is placed inside the ventricular shunt for patients with hydrocephalus [31]. The device can not only measure ICP accurately but also detect shunt failure and be calibrated with respect to puncture pressure on the shunt valve [31].

These telemetric implantable ICP sensors can help patients that need long-term ICP monitoring but are not suitable for acute measurements or short-term measurements in the intensive care, which limits the number of applicable diseases to varieties of hydrocephalus discussed in Chapter 1.1.5.2 [31].

1.1.6.2 Non-Invasive Measurements

The surgical and long term infectious risks of invasive ICP monitoring prevents the application to be used in healthy volunteers and less severe disease states. Therefore, a lack of reference data for clinical studies exists. This clinical need founded a competitive research field, with the goal to increase the access to ICP monitoring, to minimize risk of complications in clinical intensive care routines, and to improve the understanding of pressure and fluid dynamics in the brain. The approaches can roughly be divided into measurement of displacements or deformations, measurement of the hemodynamic system, and others. This section will give an overview of selected approaches for non-invasive ICP monitoring. It should be noted that none of the methods mentioned below are regular contestants in clinical settings at this point in time. Aside from the methods discussed here, further approaches can be found in numerous sources elsewhere [25, 48, 50–53].

Displacement Measurements In 1990 Reid et al. suggested that ICP can be measured by measuring the displacement of the tympanic membrane. The perilymphatic pressure in the cochlea is linked to ICP because of CSF communication across the cochlear aqueduct into the SAS, given that the aqueduct is patent, meaning CSF can flow through it [54]. The ICP is strong enough to cause a measurable displacement of the tympanic membrane from its resting position that can be linked to ICP. Displacement is measured through an air displacement sensor that seals the ear and measures volume changes (in nanolitre) [54] or as a piezo disc displacement [55]. A high ICP causes an inward motion and a negative volume change, while low ICP causes outward motion. The method relies on a baseline measurement and can only detect ICP elevation but no

quantitative pressure values [56]. Furthermore, histological studies have shown that the aqueduct is not always open to the SAS, especially in the elderly [54].

The optical nerve sheath diameter can be measured by means of ultrasound imaging, MRI or CT. Due to the connection of the optical nerve sheath to the SAS and the dura mater around the brain, changes in CSF pressure affect the nerve sheath and lead to diameter changes [57, 58]. Until recently, a widening of the sheath was used to evaluate whether ICP is elevated, but it did not allow for quantitative information. Robba et al. have since shown that a linear regression can be used to calculate ICP from the measured diameter. However, the study was performed on a very small cohort of 10 pediatric patients and further clinical testing was needed [59]. Even without quantitative numbers of ICP, this method has the benefit of requiring no extra device, as standard clinical imaging tools such as ultrasound sonography are readily available and able to image the sheath diameter fast and cost effectively. It should be mentioned that a widening in the optical nerve sheath diameter is not only caused by ICP increases, but can also be a consequence of other diseases such as inflammation and tumor, and thus requires further examination [48].

Hemodynamic Measurements Because of the closed skull environment, it is a quick thought to measure the blood flow and volume changes that occur as the blood enters and flows through the brain. A change in ICP will naturally influence the way CBF progresses through thin blood vessels. Many models and theories have been proposed to quantify this change and relate it back to ICP. One of the earliest was the pulsatility index (PI) derived from transcranial Doppler sonography (TCD), which measures cerebral blood flow velocity (CBFV) in the middle cerebral artery. The PI is the difference between systolic and diastolic CBFV, normalized by the average

CBFV across one cardiac cycle [48]. While PI can be measured easily with ultrasound devices available in clinics, it shows conflicting results, with reports about poor [48, 60, 61], moderate [59], and good [62] correlations with ICP. The largest drawback seems to be the variation a PI can have across subjects. A PI of 1 has been associated with ICP of a few mmHg to highly elevated pressures of 40 mmHg [48]. This unreliability makes translation into the clinical routine impossible.

Another way to use the pulsatile information from TCD is to calculate the critical closing pressure (CrCP), which is the pressure threshold at which the arterioles in the brain collapse and CBF ceases. The CrCP value can be approximated in many ways, including frequency domain analysis and lumped parameter modelling, yet the most intuitive way is by plotting CBF over ABP for a cardiac pulse, especially capturing the systolic and diastolic extremes. Extrapolating this curve to a CBF of 0, i.e. the x-axis intersection, will yield an approximation of the CrCP as the blood pressure where $CBF = 0$. It should be noted that this linear simplification is not necessarily reporting the true CrCP, but is a good and fast to calculate approximation. Reports of correlations between ICP and CrCP have shown a good correlation [63]. It has recently been shown that CrCP can also be measured with optical methods such as diffuse correlation spectroscopy [64, 65], with first results shown towards ICP prediction [66]. A potential drawback of this ICP estimation approach is, aside from a current lack of clinical trials, that CBF or CBFV have to be measured in alignment with pulsatile ABP.

Many groups have tried to model the hemodynamics in the brain to extract ICP. The first comprehensive model goes back to 1988, when Ursino described the fluid and pressure dynamics in a lumped parameter model [67]. While the goal of Ursino's publication was not to measure ICP

non-invasively, it has been the basis for many reports on ICP estimations using derivatives of the Ursino-model. One direct successor to the model was presented by Lee et al., who suggested a simplification and remodeling for direct ICP estimation [68], but clinical studies are needed to confirm this theoretical model in the field. Fanelli et al. recently showed how measurements of TCD derived CBFV and ABP pulse waves in a lumped parameter model can be used to estimate ICP [69]. Good ICP estimation was shown, though the cohort of 12 pediatric and young adult patients undergoing invasive ICP monitoring is small and further clinical studies are needed.

Swoboda et al. compared the ABP wave form at the carotid artery, which leads into the head and is influenced by the cranial pressure environment, with a peripheral artery (e.g. the finger) [70]. They hypothesized that the waveform in the carotid artery deforms due to pressure reflection as the wave experiences an impedance change upon entering the skull. How different the waveform is, can be determined by comparison to a systemic ABP waveform. A mathematical model of the blood flow in the brain is then used to calculate ICP based on the waveform distortion. While this device has been patented [70], a clinical study using this method has not been published to the best of my knowledge.

It was suggested before that changes in total hemoglobin concentrations, which are correlated with cerebral blood volume (CBV) in the brain, are correlated with ICP oscillations [71]. Yet there was no report to my knowledge on the direct translation of hemoglobin changes to ICP changes. The feasibility of this approach is discussed in great detail in Chapter 3.

It has also been suggested that the CBF waveform, measured inside the skull with TCD or diffuse correlation spectroscopy, changes its shape due to an impedance change in the brain, caused through ICP changes. Preliminary data has been reported by us and others [72], and a detailed

description of how to use these waveforms can be found in Chapter 3.

1.2 Cerebral Autoregulation

The measurement of ICP in clinical care can not only be used by itself, but also to derive information about cerebral autoregulation. Here it is mostly CPP that generates high correlations between common assessment techniques of CA and patient outcome.

To maintain stable blood flow despite changes in either ABP, induced for example by exercise, or ICP, induced by posture changes, the arteries and arterioles of the brain can dilate and constrict [33]. The vessel diameter change then allows to regulate CBF, keeping it approximately equal despite CPP changes. This mechanism is known as cerebral autoregulation (CA), or cerebrovascular autoregulation, and its dependence on pressure has been described as early as the 1950s by Lassen et al. [73]. Lassen showed that CBF has a plateau at which it is no longer changing despite changes in ABP. His observation was later revised to CBF be a function of CPP (see Figure 1.7).

The ability to regulate blood flow locally in the brain can be exceeded or impaired in many diseases, including TBI [74, 75], hydrocephalus [76], and stroke [77]. The clinical need to evaluate and maintain CA is obvious but reliable information is rare. In this section, the mechanics and functionality behind CA are described, including the anatomy and pressure balances that control it. A short description of diseases with known CA impairment is given, followed by a comprehensive overview of assessment methods. This is to understand what makes CA evaluation challenging and what puts the CA community in dispute over the different evaluation techniques

and the value of CA assessment in general for guidance of therapeutic decisions.

1.2.1 Mechanism of Cerebral Autoregulation

The blood supply to the brain is achieved through the internal carotid arteries and the vertebral arteries coming from the aorta. The internal carotid arteries connect together in the circle of Willis with the anterior and posterior communicating arteries and the anterior and posterior cerebral arteries. The circle of Willis further connects to all major arteries in the brain, as seen in Figure 1.5, including the middle cerebral arteries supplying the brain. In extension by the Basilar artery, additional blood is supplied from the aorta through the vertebral arteries. A complex network of interconnected arteries is thus responsible for the blood supply to the brain, which allows for compensation if one of the supplying arteries is blocked [4]. Figure 1.5 shows the ideal configuration of arteries, but it is worth noting that the circle of Willis is highly variable. A study from Papantchev et al. [78] showed that 58.6% of their test subjects had a variability, with the most common being a hypo- or aplasia of the left posterior communicating artery, thus not completing the circle of Willis. The role of this variability is suspected to have a significant influence on perfusion control, which might contribute to the inter-subject variability. The major arteries then, much like systemic arteries, branch out into more and smaller arteries, arterioles and finally into complex networks of capillaries. Here, oxygen and nutrients are transported out of the blood stream and metabolic products enter. The blood vessels then merge again to venules and larger veins that drain into the cerebral venous sinus (see Figure 1.1) and back to the heart. Arteries, veins, and capillaries have vastly different compositions of elastin fibers, collagen fibers, smooth muscles, and others, as depicted in Figure 1.6. The veins in the brain hold the

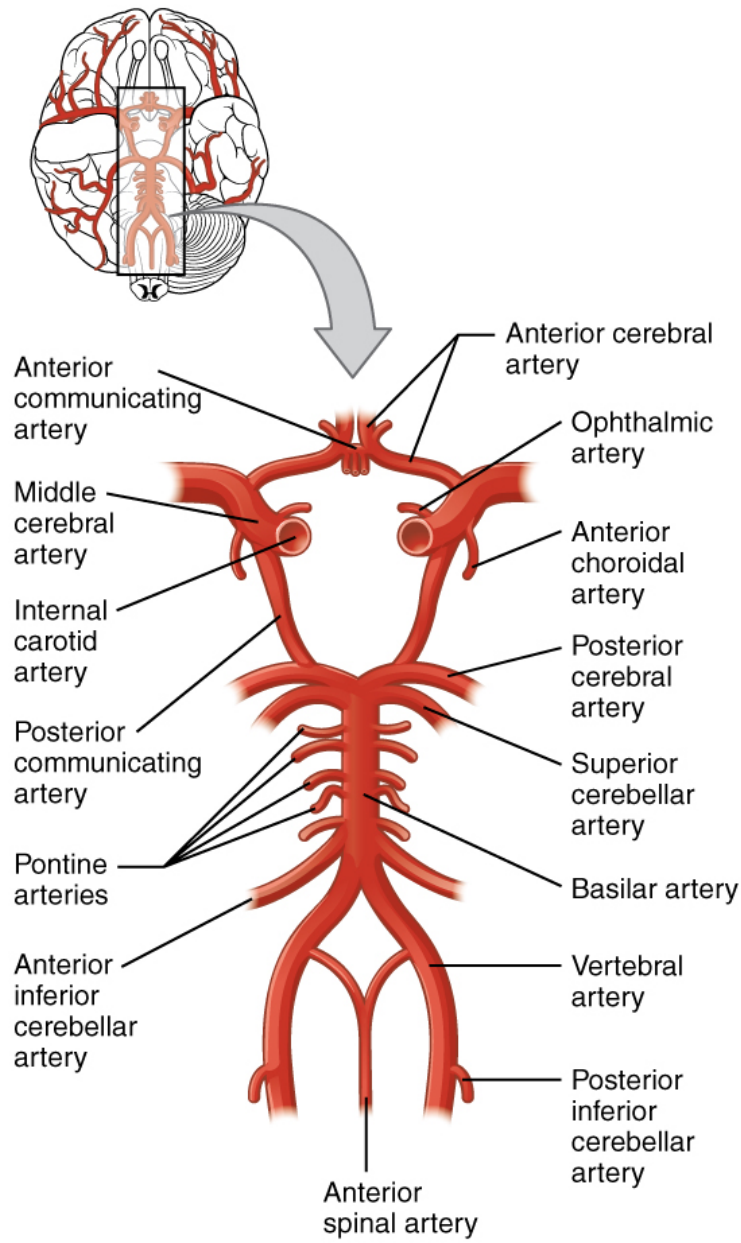


Figure 1.5: The circle of Willis, located at the base of the brain, connects all major arteries in the brain and supplies the entirety of the brain with oxygenated blood. Image taken from [79].

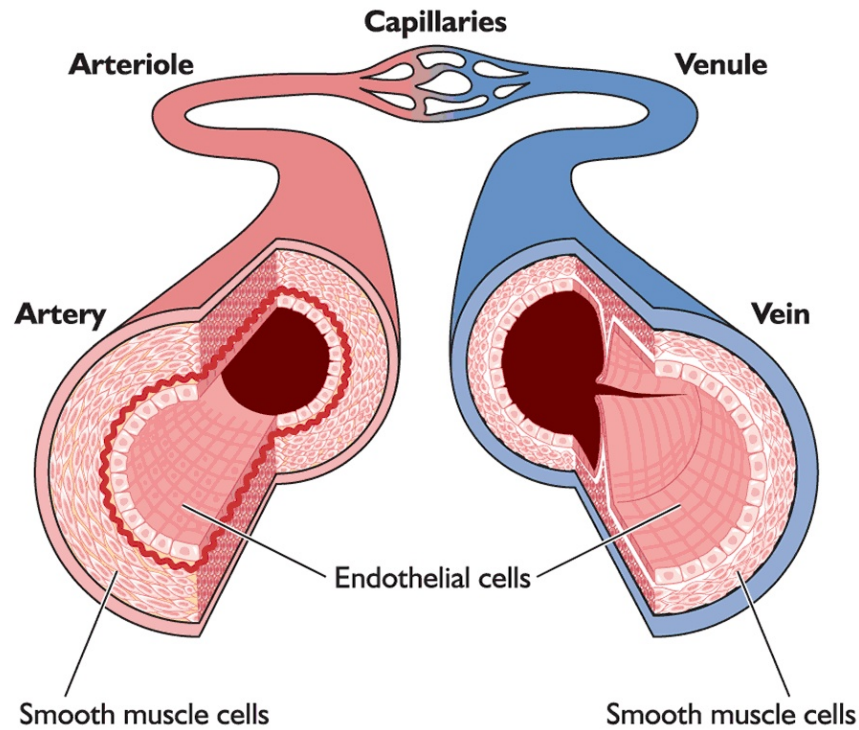


Figure 1.6: Arteries (red) show a thicker layer of smooth muscle elastin fibers, while veins (blue) are thinner walled and show valves that stop blood flow from flowing backward, thus aiding blood return to the heart. This valve does not exist in cerebral venules and veins. Image taken from [81].

majority of the blood volume [80] and are therefore the most significant contributor to CBV control in the brain, which can have influences on ICP control via the Monro-Kellie doctrine (Chapter 1.1.2). While this allows global control of CBV, local adjustments in CBF are driven by thick walled arterioles, which have a large layer of smooth muscle cells that can dilate and contract the blood vessel to change its diameter. Smooth muscles are a part of all types of blood vessels, with exception of the capillaries and small venules, but they are the most prominent component in arterioles [82], which can therefore change their cross-sectional area significantly and modulate the resistance to blood flow. How influential a diameter change is to CBF, is shown

by the Hagen-Poiseuille flow equation

$$Q = \frac{\Delta P}{R}, \quad (1.2)$$

$$R = \frac{128\mu L}{\pi D^4}, \quad (1.3)$$

where Q is the flow through a rigid pipe, ΔP is the pressure gradient across the pipe and R the resistance to flow. R is dependent on the length of the pipe L , the viscosity of the fluid (here blood) μ , and on the 4th power of the diameter of the vessel D [82]. This equation assumes a rigid vessel, a Newtonian fluid with laminar flow and a constant viscosity, all of which are not necessarily true in cerebral blood vessels, as it is a simplified model after all. Yet, the assumptions are good enough to be used in model designs and to understand that even a small diameter change of the vessel wall can have a large effect on local blood flow. Therefore, a fine control of CBF in the brain is possible. The complexity and inter-connectivity of the cerebral vascular system, with many individually regulating arteries and arterioles, makes measurement and modelling of CBF and CA challenging and contributes to the reason why blood flow control in the brain is not yet fully understood [82].

The dependency of Q (here CBF) to the pressure gradient ΔP (CPP) is linear in this simplified model and it is apparent that a drop in ABP, leading to a drop in CPP, will reduce CBF. In this case, the CA mechanisms will expand blood vessels to reduce the resistance to flow. In a passive system, a reduced pressure inside blood vessels would lower flow. Because the regulatory mechanism can only react to a sudden ABP change with a certain delay time, a typical bi-phasic reaction between ABP changes and CBF recovery is seen [82]. In case of an ICP change, the pressure on the venous sinus is increased, decreasing the pressure gradient for CBF that is CPP.

The reaction then is opposite of the reaction for ABP increases. The recovery time in either case can be measured and describes the principle of dynamic CA assessment (see Chapter 1.2.3). Blood vessels have a maximum dilation and constriction limit, which defines the CPP range in which CBF can be controlled.

The regulation of CBF described above is activated by multiple control mechanisms that operate individually or in conjunction with each other. They are categorized in control of vascular tone, capillary tone, neurogenic control, and the effects of blood gas level.

1.2.1.1 Control of Vascular Tone

The control of arterioles can be separated into local factors, neuronal factors, and hormonal factors. The local factors are arguably the most important factors, as they drive the CA response. One example of a local response is hypoxia, which leads to vasodilation, triggered by the release of Adenosine [83]. Numerous other metabolites [84] are suspected to have a combined effect on vasodilation, such that a metabolic increase or a decrease in CBF would cause an accumulation of metabolites and a vasodilation to increase CBF. Potentially best understood today is the role of nitric oxide (NO) [85], which is created in the endothelial cells through nitric oxide synthase enzymes and diffuses into the smooth muscle cells. Here it engages a chain reaction that leads to the uptake of Ca^{2+} and the opening of calcium-activated K^{+} channel, ultimately leading to vasodilation [4]. One trigger for the release of NO is believed to be the change in shear-stress on the endothelial cells upon CBF changes [86]. NO is also produced in other processes, including neuronal activity [87], and autonomic nitrergic nerves that use NO as neurotransmitter to control

vascular tone [85, 88].

1.2.1.2 Control of Capillary Tone

Recent publications have pointed out the role of pericytes, an isolated contractile cell located in the brain on the capillaries, in the blood flow control. While capillaries do not have smooth muscles, the pericytes allow for blood flow control through constriction of the capillaries itself [89]. It has also been reported that the pericyte dilation is faster than arteriolar dilation, especially as a reaction to neuronal activation [90]. The magnitude of their contribution with regards to CA, as opposed to hemodynamic responses to neuronal activation, is still up for debate.

1.2.1.3 Neurogenic Control

While there is a significant amount of research done on neurogenic control of blood flow regulation, most of it has been done with regards to neuro-vascular coupling as a response to neuronal stimulation [4]. In general, the sympathetic nervous system, the part of the autonomic nervous system that is responsible for alertness and reaction, plays a larger role in autoregulation as it can adjust vascular tone as described above and shift the upper limit of autoregulation [4]. It is however suspected that the sympathetic nervous system's role in CA is only significant under extreme conditions such as disease [91]. More research towards CA rather than neuro-vascular coupling is needed to confirm or deny these early research results.

1.2.1.4 Effects of Blood Gas Levels

It has been known that changes in arterial blood gas level, namely the partial pressure in oxygen (PaO_2) and carbon-dioxide (PaCO_2), modulate vasomotor tone [91]. CO_2 influences vasomotor tone by changing the pH, which affects NO synthesis [92]. Further research is necessary to determine if CA as a response to pressure changes and the response to CO_2 and O_2 are considered the same or if they are independent mechanisms [93]. For this, conflicting results can be found, showing that CA is modulated by CO_2 [94, 95], while others found them to be uncorrelated [96]. As of today, the following relationships of CA assessments and blood gas level have been reported:

Hypocapnia has been shown to reduce overall blood flow, with little changes to lower limit of autoregulation (LLA) and no change to its upper limit of autoregulation (ULA), with respect to CPP [97]. It has been shown however, that the response time or autoregulatory reactivity improves [98].

Hypercapnia increases blood flow, and narrows the autoregulation limits (LLA and ULA) with respect to CPP, making it more likely to exceed CA capabilities [97, 98]. It was further reported that the reactivity of CA worsens [93]. Many reports on Hypercapnia are in general agreement with these, and can be found elsewhere [4].

Hypoxia is known to reduce autoregulatory reactivity, alongside of a decrease in CBF if CO_2 is unchanged, i.e. isocapnic hypoxia [99, 100]. In hypocapnic hypoxia CA is improved, measured by the rate of recovery to normal flow after a blood pressure challenge, as compared to isocapnia [98, 101] and even as compared to normoxia [98], showing that the effect of CO_2 is stronger than O_2 .

Hyperoxia in isocapnic conditions shows no signs of CA improvement [98].

1.2.2 Clinical Significance

It is clear from the previous chapter, that many influencing mechanisms make evaluation and interpretation of CA challenging. Yet a clinical need for reliable measurements and a need for further research to better understand cerebral blood perfusion control is given.

Cerebral autoregulation is impaired in many diseases, implying that spontaneous changes in CPP can have an effect on brain perfusion. This can for example lead to subsequent ischemia after TBI or stroke. To prevent subsequent injuries the perfusion of the brain is regulated by clinicians through manipulation of ABP and ICP, thus CPP is maintained in a literature-based range to improve CBF. Current treatment guidelines for TBI for example suggest to maintain CPP above 60 - 70 mmHg in adults [17] and above 40 - 50 mmHg in children [16]. An alternative method, that has shown to improve patient outcome in TBI, is to evaluate the CA impairment through measurement of pressure reactivity, an assessment technique of CA (see Chapter 1.2.3.3), and adjust CPP accordingly [74, 102, 103]. Despite preliminary data suggesting positive effects on patient outcome, the evaluation of CA in TBI is not yet a clinical standard. Similar observations can be made for other diseases, in which early clinical studies show that CA is impaired but clinical adaptation is slow. This Chapter will give an overview of the most common diseases that impair CA and have been studied in relation to it.

1.2.2.1 Traumatic Brain Injury

TBI, as described in Chapter 1.1.5.1, is a severe injury, often including fractures and lesions, to the brain after impact. CA impairment in TBI has been reported by numerous groups, reviewed in detail [4, 104], using numerous evaluation methods further described in Chapter 1.2.3. The conclusions suggest that a lack of gold standard in CA assessment makes comparison of different studies complicated and variations in CA assessment methods and data processing occasionally leads to conflicting results [104]. Nonetheless, evidence that impaired autoregulation is associated with worse outcome, as measured by the Glasgow Outcome Score [105], has been presented by many groups for both adults [106–109] and children [74, 110, 111]. It has been reported by Steiner et al. that autoregulation can be used to determine an optimal CPP value at which autoregulation is most active, known as CPP_{opt} (see Chapter 1.2.3.3) [112, 113]. Additional clinical studies are needed to support this finding, which is why a minimum CPP value is recommended by the Brain Trauma Foundation [17], but not yet a CA guided, individualized value.

1.2.2.2 Hydrocephalus

Hydrocephalus, as described in Chapter 1.1.5.2, is not widely studied in the field of CA. While hydrocephalus with elevated ICP has an effect on CPP and can lead to reduction of CBF, it was found that even NPH shows a significant reduction in CBF in the white matter as measured by MRI [114]. It was further identified that NPH results in an increase of resistance to flow, which was correlated with intact CA, while hydrocephalus with atrophy shows disturbed CA in the middle cerebral artery territory [115]. Further research is needed to draw firm conclusions on hydrocephalus induced CA impairment. It is worth mentioning that hydrocephalus can lead to

secondary diseases which can induce dysautoregulation, such as ischemia which is discussed in the next section.

1.2.2.3 Stroke and Hemorrhage

Stroke is typically divided into ischemic and hemorrhagic, where the former is much more common and caused by a blockage of an artery, starving the brain from oxygenated blood. The latter on the other hand describes a rupture of a blood vessel inside the brain, leading to blood pooling. While the stroke death rate is reducing today due to fast intervention and restoration of normal blood flow, a high level of disability is still associated with stroke [4]. The time to re-perfusion of brain tissue and the size and location of the infarct region vary strongly across patients, which can make comparison on CA reports in stroke complex.

In acute *ischemic stroke* it has been shown that dynamic autoregulation is impaired, as measured by the phase information of a transfer function between ABP and CBFV and the autoregulation index (see Chapter 1.2.3), while the CPP range of CA activity remains the same [77, 116]. While these early results suggested a global impairment for all stroke types, it is known that CA is impaired differently in different sub-categories of ischemic stroke, varying both with location of the occlusion [117], and the vessel size affected [118]. It was found that stroke severity is influencing CA impairment, where transient ischemic attacks do not show signs of dynamic CA impairment [119]. Aries et al. reviewed stroke literature and came to the conclusion that CA is impaired in even minor strokes and that the impairment worsens in the first 5 days after acute stroke, followed by a recovery over the next 3 months [120]. Worsening and spread of dysautoregulation to the contralateral side over the first days post-stroke was later confirmed by Reinhard et al. [121],

associating it further to poor outcome.

In *hemorrhagic stroke* dynamic CA was found to be impaired as well, with the largest cohort of studies targeting subarachnoid hemorrhage (SAH). Here it was found that early impairment of CA in SAH is indicative of delayed cerebral ischemia, manifested as unilateral CA failure after 3 days or a bilateral failure seen after 1 to 2 days [122, 123]. Autoregulation is also indicative of delayed cerebral ischemia if seen in combination with vasospasm, i.e. the sudden contraction of arteries, while vasospasm alone is not [124].

It is apparent that autoregulation in stroke has been studied in greater detail than in other fields and more conclusive diagnostic value has been assigned to it. The large variety of CA evaluation methods and the mix of stroke sub-categories makes comparison challenging and gives rise to occasionally conflicting results [4, 123].

1.2.2.4 Other Conditions and Diseases on Cerebral Autoregulation

The list of diseases and conditions that affect cerebral autoregulation or are suspected to impair it is long. A selected few diseases not already mentioned above, with known effects on CA are listed below:

- **Diabetes** has been reported to impaired CA in both type 1 [125] and type 2 [126] diabetes, though type 1 diabetes only shows impairment during diabetic ketoacidosis, with a reducing effect over time, hypothesized to be caused by vasogenic cerebral edema.
- **Alzheimer's disease** is a degenerative disease of the brain, which has conflicting results about CA impairment, with strong reports claiming intact [127] and impaired [128] CA alike. A conclusion can only be drawn if further clinical studies are conducted.

- **Stenosis** describes an abnormal narrowing of a vessel, resulting in an increased resistance to flow, typically seen at the division point of the carotid artery into internal and external carotid artery, caused by plaque build-up [4]. The loss of CA in otherwise asymptomatic carotid stenosis has been shown [129], and CA recovery after stenting was reported [130]. Untreated stenosis is a high risk factor for ischemic stroke as plaque can travel upstream and block cerebral arteries, cutting off blood supply and causing subsequent CA impairment.
- **Obstructive sleep apnoea syndrome** is caused by an obstruction of the upper airway and a subsequent pause in breathing, lasting tens of seconds. It has been shown that this syndrome impairs CA and that it is correlated with the severity of the disease [131, 132].
- **Orthostatic hypertension** is one of many conditions related to impaired CA as a response to global challenges. Orthostatic hypertension describes a low pressure response to posture changes. Impairment in patients was confirmed through a head-up-tilt challenge [133]. CA impairment was also found in people with postural tachycardia syndrome, for both static and dynamic autoregulation [134].

1.2.2.5 Anesthetics and Other Drugs

CA is not only impaired in disease or injury, but can also be affected by pharmaceutical products. Due to surgery and intensive care needs, the effect of CA on anesthesia is of special clinical interest.

Inhaled and intravenous anesthetic effects on cerebral physiology are very different with respect to CBF and CBV, which can be translated to their effect on vasodilation and cardiac output

modulations in a dose related manner, and on cerebral metabolic rates [135]. Isoflurane and desflurane, as examples for volatile anesthetics, have a dilatory vascular effect, which leads to an increase in CBF and CBV [135], while at the same time reducing ABP significantly, and thus cardiac output [136]. This forced dilation in cerebral vasculature is presumably the reason why CA is no longer able to control blood flow. Intravenous anesthetics like Propofol [137], and especially opioids such as fentanyl, generally have smaller effects on cardiac output and do not cause vasodilation or -constriction [136], which will largely maintain CA ability. These findings are confirmed by studies with respect to intra-operative maintenance of CA and cerebral perfusion [138].

1.2.3 Assessment of Cerebral Autoregulation

CA can be evaluated by perturbation of the regulatory system and measurement of the response time and magnitude, for which a variety of signals can be measured, and perturbations can be performed. A perturbation here can either be an active change in conditions such as underlying ABP or a naturally occurring drift or response to environmental inputs [4]. Invasive and non-invasive ways to evaluate CA impairment has been shown, which is commonly separated into two groups: static and dynamic CA [139]. Static CA, or sometimes steady-state CA, refers to autoregulatory responses to steady-state changes in ABP or ICP, giving information about the range of CPP in which CA is active. Dynamic CA refers to rapid changes, typically in ABP, where the response time in blood flow recovery is indicative of CA. While the two are related, differences [140] and similarities [141] between the two approaches have been reported. Aside from the classic groups, a third group of pseudo-dynamic autoregulation can be defined. This

group uses moving correlations to describe the current state of CA but is often reported with a CPP dependent trend line. It is thus put in between static and dynamic CA.

1.2.3.1 Static Autoregulation

Static autoregulation is described by Lassen's curve [73, 142], which is constructed by plotting steady state (baseline) CBF vs. CPP. This curve shows a characteristic shape of monotonically increasing CBF with CPP, and a distinct CBF plateau in a range of CPP where autoregulation is intact and vessel constriction can compensate for increased pressure (see Figure 1.7). For this method both ABP and ICP need to be measured such that CPP can be calculated. CBF can be measured non-invasively with either transcranial Doppler sonography (TCD) or diffuse correlation spectroscopy (DCS). Alternatively, under the assumption that ICP remains constant or changes negligibly, Lassen's curve has been reported based on MAP vs. CBF, e.g. in stroke [143]. If autoregulation is impaired, the lower limit of autoregulation (LLA) and upper limit of autoregulation (ULA), defined as specific CPPs at which Lassen's curve changes from plateau to slope and vice versa, can shift and narrow the plateau. Alternatively, upon complete loss of CA, the plateau can be lost entirely, assuming that blood vasoconstriction or dilation is impossible.

1.2.3.2 Dynamic Autoregulation

Dynamic autoregulation is described based on transient changes in CBF in response to pressure changes and allows for the measurement of a degree of impairment. Numerous assessment methods have been proposed and the most notable will be explained below.

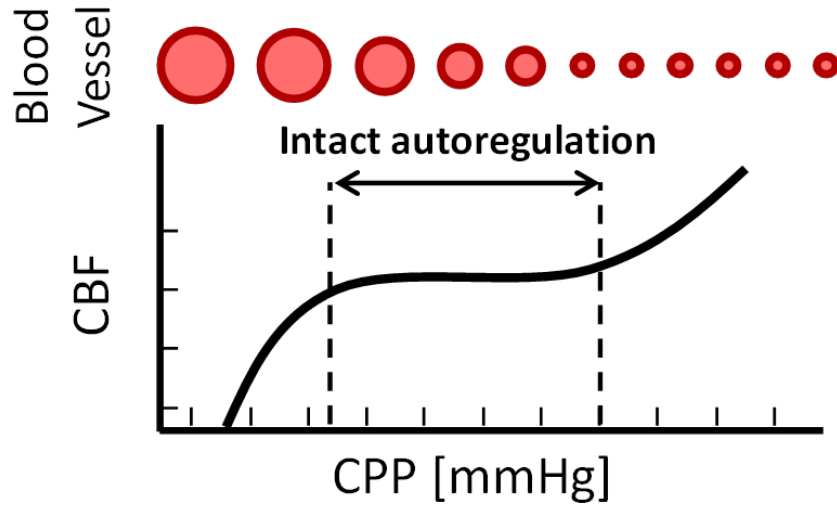


Figure 1.7: Lassen's curve shows the relation between CPP and CBF. A plateau of constant blood flow despite changes in CPP is expected if autoregulation is intact. Blood vessel diameter are shown in red on top and indicate the vascular reaction to the CPP change.

Rate of Regulation The potentially most visual way to describe how fast CBF is recovering, therefore how well the system is regulating, is by means of rate of regulation (RoR) introduced by Aaslid et al. [144], which also is the first documented evaluation of dynamic CA in humans. They introduced a step function like deflation of thigh cuffs after a 2-minute inflation time, causing a pooling of blood in the upper body and a rush of blood into the legs upon release. CBFV was measured from the middle cerebral artery while ABP was monitored in the arm. The cuff release led to a drop in ABP and CBF. The recovery time of CBFV back to baseline was measured and

the RoR calculated as shown in equation 1.4. RoR is defined as

$$\begin{aligned}
 \text{RoR} &= \frac{\Delta\text{CVR}/\Delta T}{\Delta\text{ABP}}, \\
 \Delta\text{ABP} &= \frac{\text{ABP}}{\text{ABP}_0}, \\
 \Delta\text{CVR} &= \frac{\text{CVR}}{\text{CVR}_0}, \\
 \text{CVR} &= \frac{\text{ABP}}{\text{CBFV}},
 \end{aligned}
 \tag{1.4}$$

with CVR being cerebrovascular resistance to flow, CVR_0 and ABP_0 denoting the baseline values of CVR and ABP respectively and $\Delta\text{CVR}/\Delta T$ showing the rate of progression of ΔCVR over the time window of recovery ΔT (between 1 to 3.5 seconds). A better autoregulation is thus shown by a faster RoR, with a normal rate of 0.2/s, where hypocapnic volunteers showed an average rate of 0.38/s and hypercapnic volunteers showed 0.11/s. This measurement however is not without deficits, which include the vulnerability to noise and artifacts, it requires precise measurements, and not every patient or volunteer is compliant with a 2-minute thigh occlusion [4].

Autoregulation Index To overcome some of those challenges Tiecks et al. developed a model based on quantification of the RoR, which was divided in to 10 degrees of impairment, named Autoregulation Index (ARI) [141]. The ARI describes the CBF recovery time to an ABP drop, induced by rapid deflation of thigh cuffs after arterial occlusion, much like the RoR. The model's step response, similar to a second order control system, was solved specifically for its parameters of gain and damping factors, for which 10 arbitrary states were assigned. The ARI of a subject's

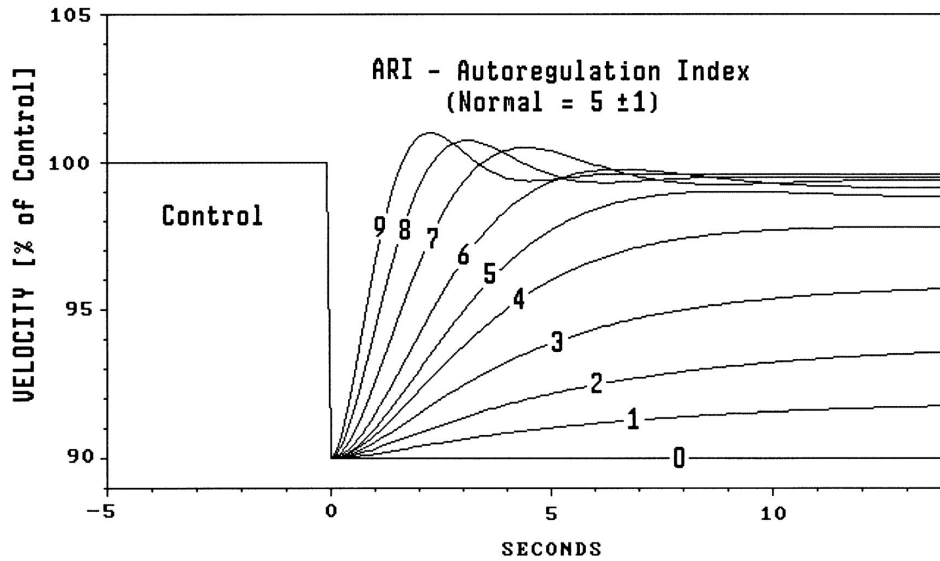


Figure 1.8: The autoregulation index (ARI) is a measurement of dynamic autoregulation. It is calculated by measuring the CBF response after an ABP step down induced by thigh cuff release. The response is fitted to a theoretical model and grouped into 10 categories from no response (0), over normal response (4-6) towards overcompensation (9), as marked in the image. This illustration was taken from [141].

autoregulatory system was then determined by root-mean-squared error fit to the 10 different model predictions (see Figure 1.8). ARIs between 0 and 9 is assigned to the response, where 0 is no response in CBF (no recovery), 4 to 6 is normal, and 9 is an overshoot above the previous normal as seen in Figure 1.8. The fitting allows to overcome the limitations of noisy data, yet the ARI relies on cuff inflations around the thighs and precise measurements used TCD for the middle cerebral artery, and is therefore limited in its application.

1.2.3.2.1 Cross-Spectral Analysis The benefit over ARI is, that it can express the CA response in greater detail than a single index can, avoiding the risk of missing details at the cost of increased complexity. When impulse and step-function responses can be measured in the time domain it is only natural to also observe them in the frequency domain. The first reported fre-

quency analysis was done by Gillert et al. [145], even though they only looked at coherence of ABP and CBFV. Analysis of gain, phase and coherence in combination is today's standard transfer function assessment and was first reported by Zhang et al. [146], as shown in Figure 1.9. Sections of resting state time domain data in a moving window is converted into frequency domain by means of Fourier transform. The power spectrum is then calculated for CBFV and ABP individually. From here, cross spectral analysis can be done to calculate gain, phase and coherence between the two signals.

$$\begin{aligned}
 S_{xx}(f) &= E[X(f)X^*(f)] \\
 S_{yy}(f) &= E[Y(f)Y^*(f)] \\
 S_{xy}(f) &= E[X(f)Y^*(f)]
 \end{aligned}
 \tag{1.5}$$

The power spectrum S is given as the expectation value (E) of the multiplication of the frequency (f) dependent spectra of input signals X and Y , here used as $X = \text{ABP}$ and $Y = \text{CBFV}$, as seen in equation 1.5. From here the transfer ($H(f)$) function can be calculated as

$$H(f) = \frac{S_{xy}(f)}{S_{xx}},
 \tag{1.6}$$

which allows the calculation of phase $\Phi(f)$ and gain $|H(f)|$ as

$$\begin{aligned}
 |H(f)| &= \sqrt{H_R(f)^2 + H_I(f)^2}, \\
 \Phi(f) &= \arctan\left(\frac{H_I(f)}{H_R(f)}\right).
 \end{aligned}
 \tag{1.7}$$

Here H_I and H_R denote the imaginary and real parts of the complex frequency domain signal, respectively. Finally, the magnitude squared coherence (MSC(f)) is calculated as

$$\text{MSC}(f) = \frac{|S_{xy}|^2}{S_{xx}S_{yy}}. \quad (1.8)$$

A typical result for this analysis is shown in Figure 1.9, which shows how the autoregulation response is similar to a high-pass filter, with low gain and large phase lead at (<0.07 Hz) then rising to large gain and minimal phase lead at high frequencies (>0.2 Hz). Special attention is given to 0.1 Hz, which tends to show high spectral power in both signals, making it a robust analysis, with a phase shift increase in hypocapnia (improved CA) and a significant decrease in hypercapnia (decreased CA) [147]. After significant differences have been found in the way transfer function analysis has been applied to evaluate CA by numerous different groups, especially in relation to data processing, and acquisition [148], the Cerebral Autoregulation Network (CARNet) published a white paper to give recommendations on how to perform transfer function analysis and improve comparability across research groups in 2016 [149], making it likely the best documented and standardized approach to CA evaluations.

Direct Phase Lag Measurements Some groups performed frequency domain dynamic CA analysis in a way different from transfer function analysis. If the phase information is most valuable for CA assessment, as determined above, one can directly induce oscillations into ABP via paced breathing or modulation of the positive end-expiratory pressure (PEEP) in the lungs for animals connected to a ventilator. Then, phase delays between relevant physiological parameters can be calculated. Fraser et al. [150] induced oscillations in a swine model by changing

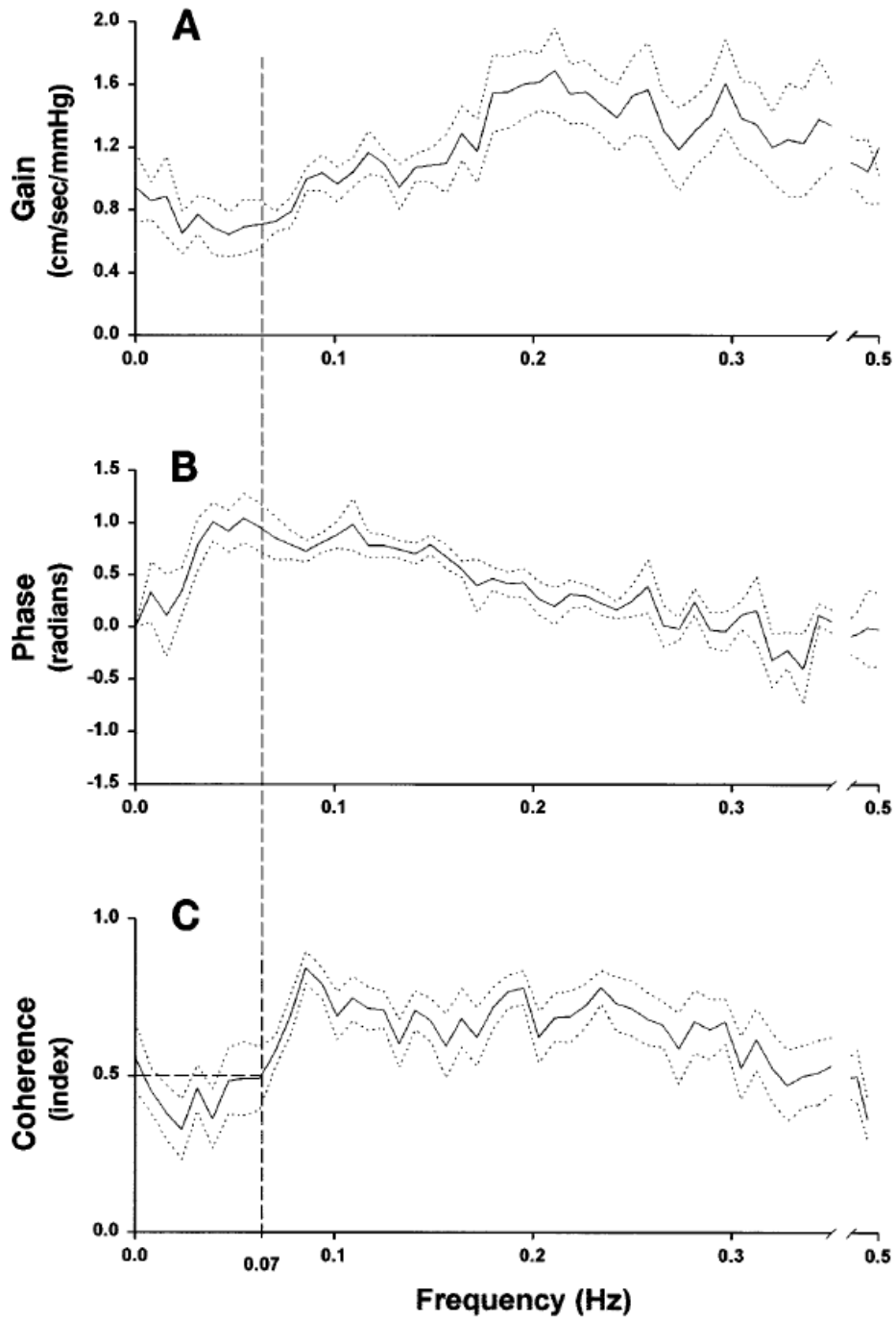


Figure 1.9: Group averaged transfer function between changes in ABP and changes in CBFV shown as solid lines, with standard error plotted as dotted lines. The signal segments of 1 second yield a frequency range of 0 to 0.5 Hz for Gain (A), Phase (B), and Coherence (C). This illustration was taken from [146]

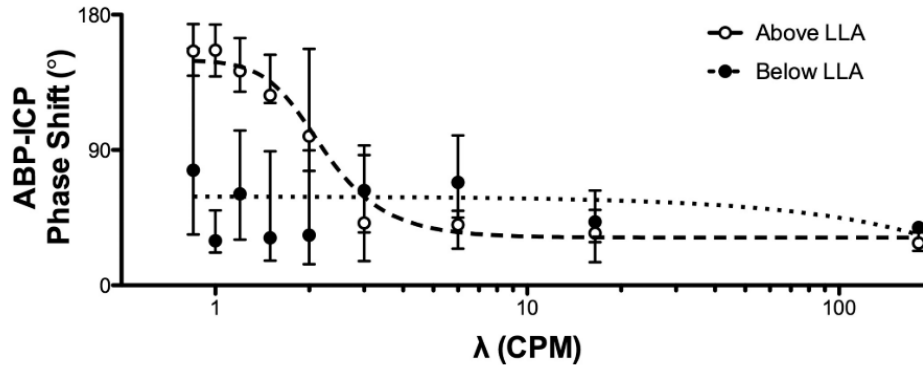


Figure 1.10: Pressure reactivity is shown as the phase delay between ABP and ICP for oscillations of PEEP in swine. If CA is intact (above LLA shown as circles) a frequency dependent phase delay is observed. This is not the case for not autoregulating measurements (below LLA shown in filled dots). This illustration was taken from [150].

PEEP, which has a strong effect on MAP, and measuring the pressure reactivity (see also Chapter 1.2.3.3). Inducing PEEP oscillations at various frequencies, they found a significantly larger phase delay to ICP for low frequencies (< 0.03 Hz) in autoregulating subjects as compared to dysautoregulation as measured by Lassen's curve (see Figure 1.10).

Similarly, Kainerstofer et al. [151] showed that a cutoff frequency ($f_c = 0.03$ Hz) can be found above which the CA response decreases. They performed a paced breathing task in human volunteers, measuring hemodynamic signals using Near-Infrared Spectroscopy (NIRS). Both groups reported independently that below f_c , CA can be evaluated via the phase difference of ABP and ICP [150] or modeled by a high-pass filter applied to the Grubb's exponent [152] that relates CBF and CBV [151].

Other Dynamic Autoregulation Measurements This active research field has seen many approaches that are summarized elsewhere [153–155]. These methods include attempts to evaluate

CA through multivariate transfer functions that include CO₂ and O₂ inputs [156], non-linear approaches [156, 157], non-stationary approaches [158], and many more that will exceed the scope of this thesis.

1.2.3.3 Pseudo Dynamic Autoregulation

The third category describes approaches that rely on windows of moving correlations between two signals. These approaches are similar to dynamic autoregulation, in that they measure a degree of impairment at any given time. However, they are also often reported as a function of CPP, describing a range of intact autoregulation to help find an optimal CPP for treatment guidance. This makes them similar to static CA as well, putting this category in between the two previous sections.

The first correlation based CA assessment has been introduced by Czosnyka et al. [159], which relates ABP and ICP dynamics. For this, a moving Pearson's correlation of ICP and ABP during naturally occurring changes of pressures, is calculated. This method is known as the pressure reactivity index (PRx), and the CA assessment as a comparison of ABP and ICP is commonly referred to as *pressure reactivity*. If PRx is low (<0.3) or negative, the autoregulatory system is intact, while high correlations show impairment. PRx assumes that a change in ABP will lead to vasoconstriction or -dilation and that this effect is significant enough to change ICP as the blood volume in the brain is changed. An increase in ABP for example leads to vasoconstriction. The smaller volume of blood resulting from the constriction then reduces ICP, making ABP and ICP negatively correlated. If CA is impaired and vascular diameter change is no longer possible, the system becomes passive and ICP will rise as ABP rises, due to increased CBV, making the PRx

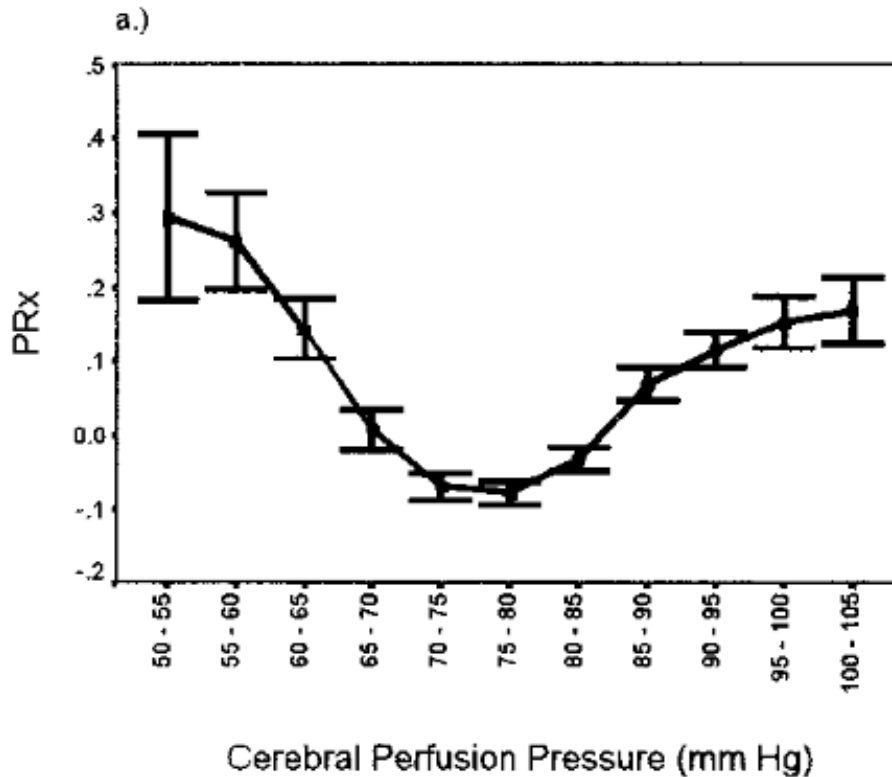


Figure 1.11: Average PRx for one example subject plotted as a function of CPP. Error bars showing the 95% confidence interval. The minimum of the curve shows highest pressure reactivity and is termed optimal perfusion pressure. This illustration was taken from [112].

value positive. This method has been used to determine the optimal CPP (CPP_{opt} , see Figure 1.11), which is where PRx is smallest, in order to optimize CA intactness and patient outcome [112].

Additionally, Steinmeier et al. performed cross-correlation of ABP and CBFV as well as between ABP and ICP, observing larger time delays in intact CA larger than in impaired [160].

Many less invasive alternatives to the PRx have been proposed, using the same strategy of moving Pearson correlation. The Systolic index (Sx) and mean index (Mx) use systolic and mean ABP, respectively, to correlate it to CBFV [94] with good relation to CA impairment while being non-invasive in nature. In some cases Mx is calculated as the correlation between CPP and CBFV and

is distinguished from M_x calculated from just ABP as M_{xa} [161]. The total hemoglobin reactivity index (THx) was calculated as a moving correlation between total hemoglobin concentration measured with NIRS and ABP, and showed good agreement with PRx [162]. Even more options have been proposed using cerebral oximetry index (COx) as a correlation of NIRS-derived tissue oxygenation and ABP [163]. The list continues further but the idea of correlation between pressure input and hemodynamic output persists.

1.3 Conclusion

ICP is an important metric for patient treatment, in case of both pressure maintenance and CA evaluation, for numerous cerebral diseases and injuries. Current measurement methods of ICP are often invasive and bear a risk when used in clinics. To counter this issue, non-invasive alternatives for ICP measurements are presented in this thesis. CA assessments rely on ICP as well. Modern CA evaluation methods are to this day verified by pressure reactivity or CPP measurements. Results for outcome correlation and CA impairment in various diseases are not cohesive and further research in clinical trials is needed. It is hypothesized that a large number of discrepancies are rooted in data relying on hospitalized patients with many different disease states and conditions and a lack of good control groups from healthy volunteers. All these needs are addressed with the development of an animal model with controlled CA impairment. Non-invasive measurements will be introduced using diffuse optical methods. To understand the physical and mathematical background, an extensive introduction into the light based diagnostics of the human body is given.

Chapter 2

Optical Imaging for Cerebral Applications

Light in its various forms has been a natural choice as a diagnostic tool for a variety of medical applications. Starting at the use of red coloring of tissue in the case of inflammation and rashes, or yellow colored eyes indicating liver disease, over microscopic applications and the advent of histology, to the application of X-rays (highly energetic light) in computer tomographic (CT) scanners to reconstruct 3D models of tissue structures inside the body, all use the diagnostic power of light. In this thesis the non-ionizing spectrum of visible to near-infrared light is used to measure hemodynamic changes and thus blood transport and oxygenation through the body. One of the earliest success stories of this field is pulse-oximetry, which uses two wavelength of light to measure the cardiac pulse driven changes in arterial blood, which can be used to calculate the percentage of oxygenated hemoglobin in arteries and consequently give information about sufficient oxygen supply to the tissue [164, 165]. Today, this device is a standard equipment in every hospital and ambulance.

This chapter shows how light can be used to measure tissue oxygenation and blood flow in

centimeters deep organs such as the brain in a non-invasive and non-ionizing way. For this reason, description of light, its properties and nomenclature, and the theory of diffuse light travel in highly scattering media such as human tissue is described first. The role of the *diffusion equation*, describing the movement of light in turbid media mathematically, is shown. It builds the basis for devices used in this thesis for the non-invasive estimation of ICP and assessment of CA. Two diffuse optical devices are used, near-infrared spectroscopy (NIRS) and diffuse correlation spectroscopy (DCS), which are measuring hemoglobin concentration and blood flow in biological tissue, respectively. If not otherwise marked, all mathematical descriptions are taken from Bigio and Fantini's "Quantitative Biomedical Optics" (2016) [166] for nomenclature consistency.

2.1 Introduction to Biomedical Optics

Light is the common term for electromagnetic radiation, which is defined by an electric field (**E**) that is linked to a magnetic field (**H**) through Maxwell's equations. In that, the field vectors for **E** and **H** are orthogonal to each other and to the angle of propagation of the light wave. The square of the electric field magnitude and the square of the magnetic field magnitude are both proportional to the energy density (and thus intensity) associated with optical radiation [166]. The energy associated with light is dependent on the oscillation frequency, or inversely the period of oscillation, which is commonly described as the wavelength in nanometer (nm). This is expressed through the following equation

$$E = hf = \frac{hc}{\lambda}, \quad (2.1)$$

where the energy (E) is dependent on the oscillation frequency of the wave (f) and Planck's constant ($h = 6.63 \times 10^{-34}$ Js). Here,

$$f = \frac{c}{\lambda}, \quad (2.2)$$

with c describing the speed of light (assuming vacuum approx. 3×10^8 m/s) and λ is the wavelength of the light. The typical wavelengths range for the visible spectrum is 400 nm (blue) to 750 nm (red), which corresponds to an oscillation frequency of about 750 THz to 400 THz, yielding a quantum energy of 3.1 eV to 1.65 eV, respectively. In this thesis, longer wavelengths will be used, going up to 850 nm and entering a range of the optical spectrum that is known as "near-infrared". These higher wavelengths have a lower frequency, thus a lower energy and a lower potential to harm tissue through ionization or heat accumulation.

In classical physics, a wave can be characterized by its frequency and amplitude. This, however, is not necessarily true in the quantum world. If the power of the light source is reduced very low, light detectors will not be able to detect continuous waves any longer. Instead, the light would reach the detector in small quantized packages known as photons. Photons have particle like characteristics and represent the smallest amount of energy at a given wavelength that can represent light [166]. The energy of one photon is described by equation 2.1. Because fractional photons cannot exist, the energy level for N photons is equivalent to $N \cdot hf$. When the number of photons detected becomes significantly large, i.e. $\sqrt{N} \ll N$, where \sqrt{N} is a noise estimate, the measured light characteristics starts to lean towards the classical physics regime [166]. The noise in this case is a detection variability from measurement-to-measurement known in the field as shot noise, following a Poisson distribution. It can be thought of as flipping a coin in sets of 10 flips. You are not guaranteed to receive 5 heads in every set. Likewise, you are not guaranteed

to measure the same amount of photons in a given time window, creating a measurement noise originating from the particle property of light.

2.1.1 Optical Nomenclature

To discuss the interaction of light with tissue and appreciate the functionality of modern optical devices to measure medical and biological information, the following nomenclature is defined.

Intensity describes the amount of optical energy delivered per unit time, and per unit area, on a surface. The unit is W/m^2 . It should be noted that the name "intensity" in the field of biomedical optics is often used to describe the power (P) of light, neglecting the spatial aspect. This is likely attributed to the fact that a high number of approaches and models assume point sources for light generation. The physically correct definition is:

$$I(t) = \frac{P(t)}{A}, \quad (2.3)$$

where A is the illuminated surface area.

The **fluence rate** Φ is a highly relevant metric in biomedical optics as it describes the optical energy per unit time, per unit area, incident from any direction. The direction is of particular concern in turbid media such as biological tissue, as opposed to surface illumination, for which the intensity is the equivalent. Fluence rate is defined as

$$\Phi(r, t) = \int_{4\pi} L(r, t, \hat{\Omega}) d\Omega, \quad (2.4)$$

with r indicating the point of interest, t indicating the point in time, $\hat{\Omega}$ the direction of propagation and L being the radiance.

Radiance is the light traveling through a medium per unit area along the direction $\hat{\Omega}$. It is dependent on the power (P), area (A), direction ($\hat{\Omega}$), and defined as

$$L(\hat{\Omega}) = \frac{d^2P}{d\Omega dA \hat{\Omega} \cdot \hat{n}} \quad (2.5)$$

where \hat{n} denotes the unit vector. Radiance can be thought of as directionally diverging intensity, giving it increased relevance in biomedical optics. By accounting for light divergence and the area of interest, it can for example be used to calculate the coupling efficiency of light from a light source into an optical fiber [166].

2.1.2 Optical Properties of Tissue

In a given volume inside a medium, the number of photons can be changed as photons can be emitted by a light source, delivered into, reflected out of, and transmitted through the volume or finally be absorbed. For biological tissue, these effects are due to interaction of the photon with the molecules and larger structures in the volume, or the lack thereof in the case of transmittance. Absorption of light describes the process of absorbing the electromagnetic wave energy by electrons in the atomic structure of the medium with the same or similar energy level. The absorbed additional energy lifts the electron to an elevated energetic state. From here, the energy can be dissipated as heat through vibration, in which case the photon is "permanently lost".

Scattering is governed mostly by two different processes. If the scattering particle diameter

$d \ll \lambda$, the particle's charge effectively acts like a dipole. The oscillating electric field of light is causing the particle to oscillate at the same frequency, which in turn becomes a radiating dipole. The radiated energy is an electromagnetic wave with the same frequency, or in other words the same wavelength of light. This is known as Rayleigh-scattering [167].

The main scattering events observed in biological tissue originate from refraction index mismatches of different tissues, organs, organelles, membranes and many more where $d \geq \lambda$, and not the Rayleigh-scattering mentioned above [166]. Similar to light scattering of water in clouds, with water droplet diameters of a few μm , the μm to mm sized structures in biological tissue cause refraction based scattering known as Mie-scattering [167]. The heterogeneous distribution of water droplets and air in the clouds equals the heterogeneity of different small structures in the human tissue with different refractive indices. The origin of Mie- and Rayleigh-scattering and their mathematical derivation from Maxwell's equation of electromagnetic wave scattering with dielectric spheres is beyond the scope of this introduction, but can be found elsewhere [167].

The main characteristics necessary to describe the light tissue interaction are the refractive index, the absorption and scattering coefficient, and in the case of diffuse light tissue spectroscopy especially, the reduced scattering coefficient, which are defined here:

Index of refraction is a ratio of the speed of light in a medium compared to vacuum. The speed of light in vacuum is $c = 299,792,458 \text{ m/s} \approx 3 \times 10^8 \text{ m/s}$, at a defined refractive index of $n = 1$. For water the refractive index is $n = 1.3$, reducing the speed of light to $c_{n=1.3} = c/n \approx 2.3 \times 10^8 \text{ m/s}$, and in glass $n = 1.5$, leading to $c_{n=1.5} \approx 2 \times 10^8 \text{ m/s}$. The effect of refraction is the change of propagation direction when light passes through a boundary of two media with

different refractive indices. If the light comes from a lower to a higher n , i.e. from a faster to a slower medium, the light bends towards the normal of the boundary area and vice versa. This effect can be attributed to the different arrival times of the electromagnetic wave front sides at the boundary, making refraction dependent on the incident angle, and eliminating the effect for light orthogonal to the boundary area.

The **absorption coefficient** (μ_a) describes the medium specific probability for a photon to be absorbed in a given unit distance. A typical value for perfused brain and muscle tissue is about 0.1 cm^{-1} . The average distance a photon can travel before being absorbed is called the absorption mean free path and is defined as

$$\text{mfp}_a = \frac{1}{\mu_a}. \quad (2.6)$$

The absorption coefficient of a macro scale medium is dependent on the concentration and combination of molecules that it is made of. By isolating molecules, the molar extinction coefficients for many materials have been empirically determined. Using this knowledge, we can calculate μ_a as

$$\mu_a(\lambda) = \sum_i C_i \varepsilon_i(\lambda), \quad (2.7)$$

where C_i and ε_i are the concentration (in M) and molar extinction coefficient (in $\text{cm}^{-1}\text{M}^{-1}$) for the i^{th} component of the medium, respectively. Note that ε is dependent on wavelength λ , making μ_a wavelength dependent, too.

The **scattering coefficient** (μ_s) is the equivalent to the absorption coefficient for light scattering events, thus it describes the likelihood of a photon to be scattered within a unit length in

turbid medium such as biological tissue. A typical value for μ_s in tissue is 100 cm^{-1} . Also similar to mfp_a , a scattering mean free path mfp_s can be calculated as the inverse of μ_s , describing the average distance a photon can travel before being scattered. For biological tissue $\mu_s \gg \mu_a$ in the range of red to near-infrared light (650-850 nm), which are the wavelengths used in all following devices.

A **reduced scattering coefficient** is defined to accommodate the fact that biological tissue under Mie-scattering is highly forward scattering, meaning the direction of propagation is largely preserved despite multiple scattering events. The change in propagation direction is described by the anisotropy factor g , which is defined as

$$g \equiv \langle \cos \theta \rangle = 2\pi \int_0^\pi \cos \theta p(\theta) \sin \theta d\theta, \quad (2.8)$$

where θ is the angular change of direction in a simplified case of unpolarized light and isotropic scattering particles. $p(\theta)$ describes the phase function, an angle dependent probability of photon scattering from a defined input to a defined output direction. The value of g is set between -1 and 1, where -1 shows full backward scattering, 0 represents isotropic scattering from very small particles while 1 defines perfect forward scattering from large particles. In the case of bulk tissue, an average forward scattering of $g = 0.75$ to 0.98 can be found [168]. Because the measurement of g in tissue is challenging, a widely accepted value of $g = 0.9$ is assumed, which corresponds to an average scattering angle of 26° , leaving the most likely direction to be largely forward. Because it takes many scattering events for a photon to truly change direction, the reduced scat-

tering coefficient (μ'_s) was introduced:

$$\mu'_s = \mu_s(1 - g). \quad (2.9)$$

With $g = 0.9$ and $\mu_s = 100\text{cm}^{-1}$, it follows that $\mu'_s = 10\text{cm}^{-1}$. This parameter is of special interest in the field of diffuse optics, discussed in Chapter 2.2.1.

2.2 Diffuse Optics and Tissue Interaction

When biological tissue is illuminated, light will interact with structures inside of it. Possible interactions are illustrated in Figure 2.1, which shows events of emittance (a), surface reflection (b), scattering (c), diffuse reflectance (d) as light exits the tissue after multiple scattering events at a different location, absorption (e), and transmission (f). For the use of light according to applications in this thesis, the most important interactions are scattering, eventually leading to diffuse reflectance, and absorption.

2.2.1 Diffuse Light

As mentioned before, the dominant interaction of light in tissue is scattering, with scattering events being a thousand fold more likely than absorption, as determined by $\mu_s \gg \mu_a$. Scattering can be approximated as isotropic under consideration of the anisotropy factor, yielding μ'_s . The inverse ($1/\mu'_s$) is the distance after which isotropy, i.e. scattering in all directions with equal likelihood, can be assumed, meaning its original direction can not be determined. It is often referred to as the photon's "memory loss". Note that in reality, the photon has scattered approximately

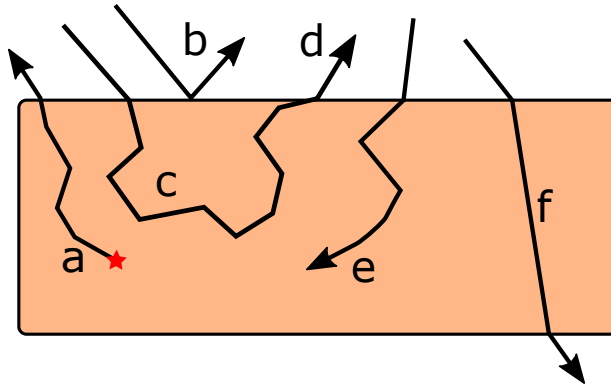


Figure 2.1: The square shows a tissue cross-section that is simplified as a homogeneous medium. a) is light emittance b) shows surface reflection, c) shows scattering inside the medium while d) shows diffuse reflectance, e) shows absorption of light in the medium, and f) is light transmittance. Every direction change inside the medium is a scattering event while the direction change when entering and leaving the medium is caused by refraction.

10 times, yet under the assumption of isotropy it is treated as one scattering event. This distance therefore, marks the boundary for diffuse optics, as opposed to ray optics in which the direction of propagation is well known and can be determined at any point in time or space.

To understand how one can derive spectroscopic measurements in this random environment, the propagation of light in diffuse medium needs to be determined. Only then a projection to medically relevant parameters is possible.

The Boltzmann transport equation, also known as the radiative transfer equation, is a heuristic model that looks at light as photons and considers the *diffusion* of photons into and out of a unit volume, the *collision* of photons with absorbers or scatterers, and the emittance of photons at *sources* inside the volume as described by

$$\frac{\partial u(r, \hat{\Omega}, t)}{\partial t} = \left(\frac{\partial u(r, \hat{\Omega}, t)}{\partial t} \right)_{Diff} + \left(\frac{\partial u(r, \hat{\Omega}, t)}{\partial t} \right)_{Coll} + \left(\frac{\partial u(r, \hat{\Omega}, t)}{\partial t} \right)_{Sources} . \quad (2.10)$$

Here, $u(r, \hat{\Omega}, t)$ is known as the angular energy density and is defined as $u(r, \hat{\Omega}, t) = L(r, \hat{\Omega}, t)/c_n$, with c_n as the speed of light in the medium and L , the radiance described in equation 2.5. Writing the Boltzmann equation out will lead to a still very complex system that is dependent on incident $\hat{\Omega}$ and scattering angle $\hat{\Omega}'$:

$$\begin{aligned} \frac{\partial u(r, \hat{\Omega}, t)}{\partial t} = & \left(-c_n \hat{\Omega} \cdot \nabla u(r, \hat{\Omega}, t) \right)_{Diff} \\ & + \left(-c_n (\mu_a + \mu_s) u(r, \hat{\Omega}, t) + c_n \mu_s \int_{4\pi} u(r, \hat{\Omega}', t) p(\hat{\Omega}', \hat{\Omega}) d\Omega' \right)_{Coll} \\ & + (q(r, \hat{\Omega}', t))_{Sources}, \end{aligned} \quad (2.11)$$

where $q(r, \hat{\Omega}', t)$ describes the energy emitted by a light source per unit time, per unit volume and per unit solid angle about time t , position r and direction $\hat{\Omega}$. This still rather complex equation can be further simplified by applying boundary conditions and assumptions about the nature of light propagation in biological tissue, to simplify the expression.

While the derivation is beyond the scope of this thesis, the procedure to simplify the Boltzmann equation starts by expanding the angular dependency of the energy density, scattering phase function and source terms into discrete sets on the basis of spherical harmonics to minimize the complexity of integro-differential equations [166]. From here an infinite set of equations arises that can be significantly shortened for sufficient approximations under the assumptions of $\mu_a \ll \mu_s$, and that the light source and distance (r) are sufficiently far apart ($r > 1/\mu_s$) [166]. At this point a simplified Boltzmann equation has been derived that is known as the P_1 approximation as it only uses spherical harmonics of the 0th and 1st order [169]. In case of biological tissue spectroscopy, the equation is further simplified by enforcing more restrictions. These are

strong isotropic scattering, which is given under the assumption that $\mu'_s \gg \mu_a$, **isotropic source** to reduce further angular dependencies for potential light emittance in the medium, and **slow optical signals** meaning that the time scale for transient changes in radiant energy density or light emittance is long compared to the time of absorption and scattering events [170, 171]. Given these assumptions we gain the *diffusion equation*, which allows the development of numerous diffuse optical devices used in medical applications.

$$\frac{\partial U(r,t)}{\partial t} = \nabla \cdot [D\nabla U(r,t)] - c_n\mu_a U(r,t) + S_0(r,t) \quad (2.12)$$

The change in radiant energy density $U(r,t) = \Phi(r,t)/c_n$ can also be expressed using the photon number density:

$$\frac{\partial \Phi(r,t)}{\partial t} = \nabla \cdot [D\nabla \Phi(r,t)] - c_n\mu_a \Phi(r,t) + c_n S_0(r,t). \quad (2.13)$$

Considering the three terms on the right, the change in number of photons in a given volume around a given position at a given time is equal to the photon diffusion in and out of the medium described by the diffusion coefficient D minus the photons absorbed, plus the photons emitted.

The diffusion coefficient D is defined as

$$D = \frac{c_n}{3(\mu'_s + \mu_a)}, \quad (2.14)$$

and it is clear that it is highly dependent on μ'_s .

The photon transport in diffuse versus non-scattering medium is demonstrated in Figure 2.2. The light travels in a circular pattern around the source, due to the isotropic assumption in biological

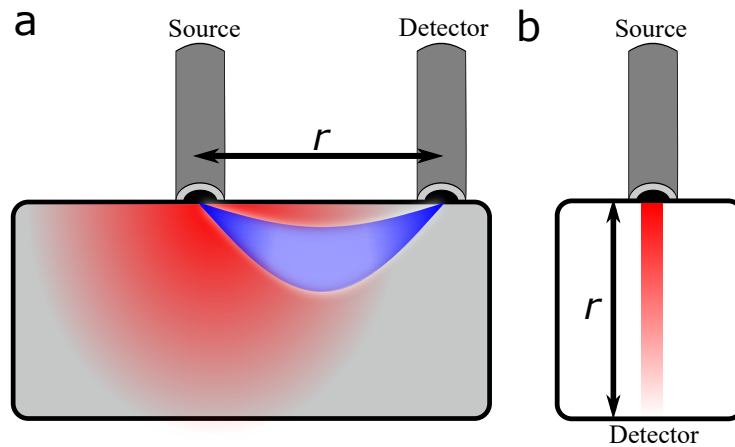


Figure 2.2: Light propagation of an incident light source on the surface of a medium is shown in red color. a) shows how light propagates in highly scattering medium such as optical tissue (red). The light detected in a second optical fiber at a distance r has propagated along the mean photon path (blue banana). b) shows the light propagation in a non-scattering medium for comparison.

tissue. Light propagation from the source to the detector can be described by a probability density function (Figure 2.2).

2.3 Near-infrared Spectroscopy

Near-infrared spectroscopy (NIRS) in general refers to the measurement of the interaction of electromagnetic waves with matter in the regime of near-infrared (NIR) light, from about 750 - 1400 nm (spectroscopy). The first use of a NIRS device was presumably done by Jöbsis et al. in 1977 [172]. Since then, the field has progressed significantly. The work in this thesis will concentrate on the medical application of NIRS for the measurement of absorption changes due to changes in hemoglobin concentration in biological tissue, which will give further information about tissue oxygenation and blood volume changes. The development of light modulation leading to the ability to not only measure changes but absolute concentrations of chromophores

inside biological tissue will further be discussed.

2.3.1 Light Absorption in Non-Scattering Medium

Scattering events are occurring at biological structures in the μm to mm scale. The main absorbers in biological tissue are water, melanin, lipids and hemoglobin. While water, melanin and lipids are fairly constant over time, hemoglobin concentrations can change with blood volume. Furthermore, oxygenated hemoglobin (HbO) and deoxygenated hemoglobin (Hb) concentrations can change independently, which influences the tissue oxygen saturation of hemoglobin, for example, caused by blood flow changes. The main focus of this work is therefore on hemoglobin related changes in optical signals.

In non scattering medium (see Figure 2.2b), the absorption coefficient of a medium inside a cuvette with known width r can be described by the Beer-Lambert's law, which states that

$$I = I_0 e^{-\mu_a r}, \quad (2.15)$$

where the intensity I measured on one side of the cuvette is dependent on the input light intensity (I_0) from the opposite side of the cuvette, and falls off exponentially over the distance r . Solving equation 2.15 for μ_a , it can be seen that

$$\mu_a = -\frac{1}{r} \log \frac{I}{I_0}, \quad (2.16)$$

and the concentration can be calculated using Equation 2.7 as $C = \mu_a / \epsilon$. The travel path for non-scattering medium is given by the source detector distance. For scattering media, the Beer

Lambert's law does not hold since the photon path is no longer describable by a straight line. A solution to the diffusion equation needs to be applied in order to calculate changes in μ_a .

2.3.2 Modified Beer-Lambert's Law

To calculate absorption coefficient changes in a highly scattering medium, one can use what is commonly called the "modified Beer-Lambert's law". Despite its name, it is not a derivation of Beer-Lambert's law, but instead is derived from the diffusion equation [173].

Under the assumption of continuous wave light, where the light source emittance is constant over time, the derivative over time on the left side of Equation 2.13 is obsolete. One can further assume that position $r = 0$ houses the light source and that $S_0(r) = P_{CW}\delta(r)$, where P_{CW} is the power of the continuous wave light and δ is the Dirac delta function, a mathematical description of a point source. This yields the following solution to the diffusion equation for continuous wave (CW) light

$$\Phi_{CW}(r) = P_{CW} \frac{3(\mu'_s + \mu_a) e^{-r\sqrt{3\mu_a(\mu'_s + \mu_a)}}}{4\pi r}, \quad (2.17)$$

which shows the CW fluence rate $\Phi_{CW}(r)$ with distance r from the point source. Note that this equation is only valid for $r > 1/\mu'_s$ as per diffusion approximation, making the infinite fluence rate at $r = 0$ due to the Dirac delta a nonissue. Equation 2.17 is dependent on knowledge of the exact light power P_{CW} induced into the medium and it needs knowledge of both μ_a and μ'_s . Given that currently only absorption coefficient changes ($\Delta\mu_a$) over time (t) are of interest, it can further be assumed that $\mu_a = \mu_{a0} + \Delta\mu_a(t)$, leading to $\Phi_{CW}(r,t) = \Phi_{CW0}(r) + \Delta\Phi_{CW}(r,t)$. Further simplifying the equation by assuming that $\mu'_s(t) = \mu'_{s0}$, with no change over time, and

considering $\mu'_s \gg \mu_s$ one can replace $(\mu'_s + \mu_a) \approx \mu'_s$. Under these additional conditions, the fluence rate change over time can be calculated as

$$\Delta\Phi_{CW}(r,t) \approx -P_{CW} \frac{[3\mu'_{s0}]^{3/2}}{8\pi\sqrt{\mu_{a0}}} e^{-r\sqrt{3\mu_{a0}\mu_{s0}}} \Delta\mu_a(t), \quad (2.18)$$

under the condition that $\Delta\mu_a(t) \ll \mu_{a0}$ and hence $\Delta\Phi_{CW}(r,t) \ll \Phi_{CW0}(r)$. This solution to the diffusion equation for small fluence rate changes over time can then be expanded to relative changes of fluence rate by taking the ratio between equation 2.18 and equation 2.17. With $\mu'_s + \mu_a \approx \mu'_{s0}$ it follows

$$\frac{\Delta\Phi_{CW}}{\Phi_{CW0}}(r,t) \approx -r \frac{\sqrt{3\mu'_{s0}}}{2\sqrt{\mu_{a0}}} \Delta\mu_a(t). \quad (2.19)$$

Solving equation 2.19 for $\Delta\mu_a(t)$ yields what is known as the modified Beer-Lambert's law

$$\Delta\mu_a(t) = -\frac{1}{r\text{DPF}} \frac{\Delta\Phi_{CW}(t)}{\Phi_{CW0}} \quad (2.20)$$

where the differential pathlength factor $\text{DPF} = \frac{\sqrt{3\mu'_{s0}}}{2\sqrt{\mu_{a0}}}$ [173]. For practical application in chapters 3 and following, $\Delta\Phi_{CW}(t) = \Phi_{CW}(t) - \Phi_{CW0}$, where $\Phi_{CW0} = \Phi_{CW}(t=0)$ is the measured intensity at time point 0 at a given distance, rather than the fluence rate of the source itself. Thus, it is also apparent that $\Delta\mu_a(t=0) = 0$.

The similarity of equations 2.16 and 2.20 is apparent when considering that $I = \Phi$ in the case of a surface area illumination and that $\log\left(\frac{\Delta I}{I_0}\right) \approx \frac{\Delta I}{I_0}$ for small changes in intensity. The additional factor of DPF accounts for the scattering part, as derived above, and symbolizes the modification to the Beer-Lambert's law. The approaches shown in Chapter 3.1 and 5 rely on hemoglobin

concentration changes derived using the modified Beer-Lambert's law.

2.3.3 Multi-Distance Approach

The modified Beer-Lambert's law can be used to calculate changes in absorption coefficient ($\Delta\mu_a$). To measure absolute values of μ_a and μ'_s , absorption and scattering events need to be distinguished. To achieve this, multiple variations of NIRS have been proposed, including time domain NIRS which exploits a pulsed laser and measures the photon counts arriving at the detector over time, yielding information about time of flight and thus scattering events inside the medium where as the light intensity corresponds to absorption [174, 175]. Similarly, a frequency domain (FD) method was proposed by Fantini et al. to disentangle scattering and absorption events by using sinusoidally oscillating light powers to gain information about absorption changes from the amplitudes (Φ_{AC}) and scattering from the phase delay (θ) of the oscillation compared to the input signal (see Figure 2.3a) [176]. This measurement is performed at a minimum of 2 source-detector separations, though for improved SNR a standard of 4 source-detector pairs has been established in the field, as demonstrated in Figure 2.3b. The name multi-distance approach refers to these source detector pairs and was chosen to distinguish it from other methods of FD-NIRS, such as a multiple-frequencies FD-NIRS, as used in diffuse optical spectroscopic imaging (DOSI) [177, 178].

Note that in Figure 2.3b the average photon path increases in depth as the source detector separation increases. This effect for semi-infinite medium, i.e. medium that has one optical boundary on which source and detectors are placed (say skin) and is otherwise "infinite" with respect to the effective photon mean free path ($\text{mfp}_{eff} = 1/(\mu_{eff})$), scales with the square root of the source

detector separation:

$$\langle z \rangle_r = \frac{1}{2} \sqrt{\frac{r}{\mu_{eff}}}, \quad (2.21)$$

with

$$\mu_{eff} = \sqrt{3\mu_a(\mu'_s + \mu_a)}. \quad (2.22)$$

Here $\langle z \rangle_r$ is the mean photon-visitation depth, with dependency on the source detector separation (r) [166]. This means a higher depth sensitivity can be reached by increasing the source detector separation at a cost of reduced photon counts due to the exponential light intensity decay over distance as has been seen in chapter 2.3.2 and will be discussed below.

The modulation frequency that is chosen for FD-NIRS needs to be fast enough to generate a measurable phase shift within typical source detector separations of about 3 cm. It also needs to be slow enough to not cross the full oscillation mark, at which point it is not possible anymore to distinguish between e.g. π and 3π . Given optical properties for tissue ($\mu'_s = 10 \text{ cm}^{-1}$, $\mu_a = 0.1 \text{ cm}^{-1}$, $n = 1.3$) and a target phase shift of $\theta \approx 1 \text{ rad} \approx 57^\circ$ for a 3 cm source detector separation yields a modulation frequency of $\omega \approx 130 \text{ MHz}$. The devices used for research described in this thesis are using an $\omega = 100 \text{ MHz}$ light modulation frequency. Starting with the general diffusion equation (Equation 2.13) a point source is placed at $r = 0$, which emits a sinusoidally modulated light at angular frequency ω . The source term of the diffusion equation can then be written as $S_0(r, \omega, t) = P_{FD}(\omega)\delta(r)e^{-i\omega t}$. As the time dependency of this signal is fully described by the oscillation term $e^{-i\omega t}$, and thus the time derivative becomes a multiplication with

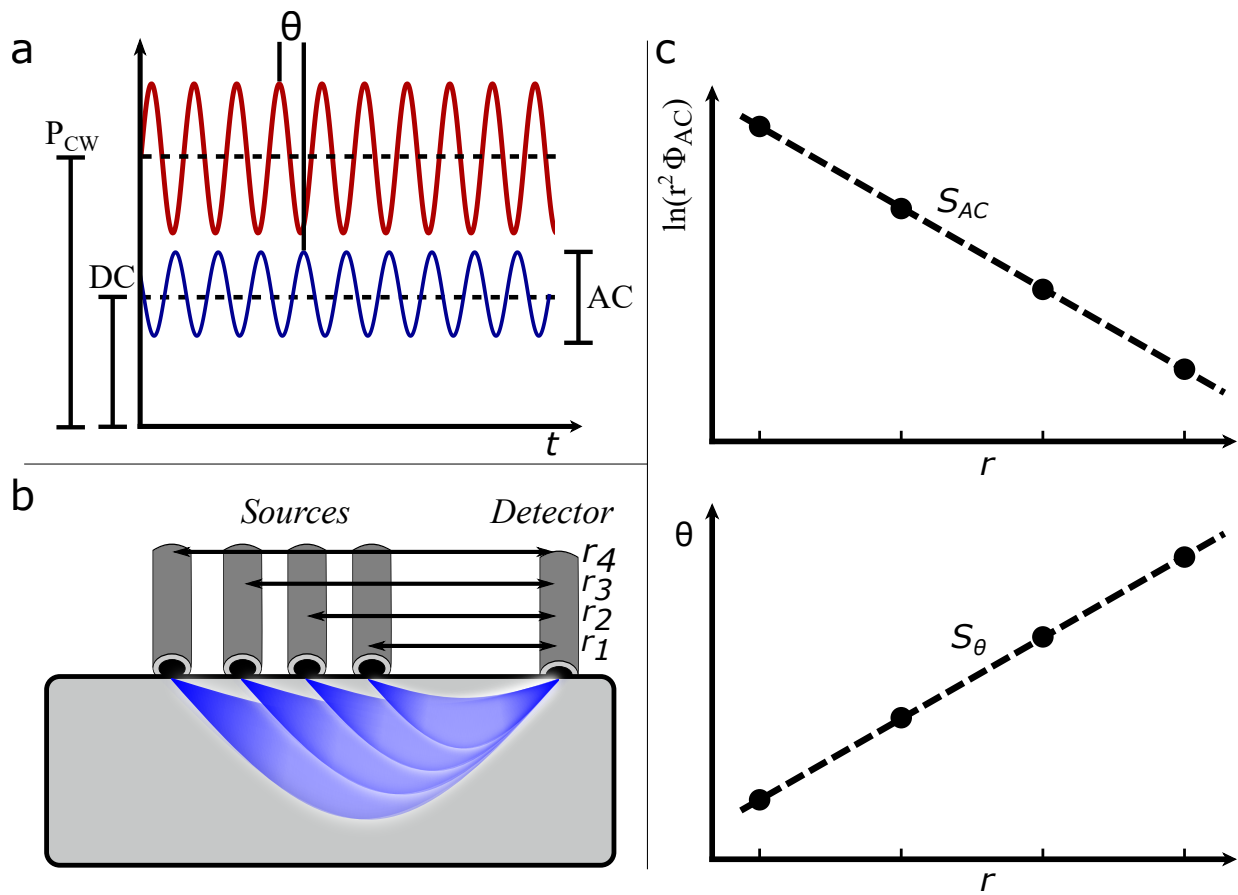


Figure 2.3: a) shows the power modulation of the incident light (red) and the measured light (blue). The properties of frequency domain light are determined by the offset (DC), the amplitude (AC) and the phase delay between input and output (θ). In b) a 4 source-detector-distances NIRS example is shown, with 4 sources and 1 detector. The average light path is shown in blue. The graphs in part c) show the linear decrease of $\ln(\Phi_{AC})$ over distance and the linear increase of θ .

$-i\omega$, the solution to the diffusion equation becomes

$$\Phi_{FD}(r, \omega) = P_{FD}(\omega) \frac{3(\mu'_s + \mu_a)}{4\pi} \frac{e^{-r\sqrt{3(\mu'_s + \mu_a)(\mu_a - \frac{i\omega}{c_n})}}}{r}. \quad (2.23)$$

The frequency domain fluence rate $\Phi_{FD}(r, \omega)$ is dependent on the amplitude P_{FD} [179]. Note that $\Phi_{FD}(r, 0) = \Phi_{CW}(r)$ from Equation 2.17, which simultaneously represents the DC component as the offset of the fluence rate modulation, as shown in Figure 2.3a.

From here, calculating the oscillation amplitude AC, and phase position θ is possible and yields

$$\Phi_{AC}(r, \omega) = |\Phi_{FD}(r, \omega)| = P_{FD}(\omega) \frac{3(\mu'_s + \mu_a)}{4\pi} \frac{e^{-r\sqrt{\frac{3\mu_a(\mu'_s + \mu_a)}{2}} \sqrt{1 + \left(\frac{\omega}{c_n\mu_a}\right)^2 + 1}}}{r}, \quad (2.24)$$

$$\theta(r, \omega) = \text{Arg}[\Phi_{FD}(r, \omega)] = r\sqrt{\frac{3\mu_a(\mu'_s + \mu_a)}{2}} \sqrt{\sqrt{1 + \left(\frac{\omega}{c_n\mu_a}\right)^2} - 1}, \quad (2.25)$$

with phase $\theta(r, \omega)$ given in radians.

While the relation between phase (θ) and modulation frequency (ω) under given conditions of absorption and scattering is non-linear, especially if $\omega/2\pi \approx 180 - 500\text{MHz}$, in the special range of ($\omega \ll c_n\mu_a$) linearity can be assumed [166]. With this condition in place, phase differences ($\theta(r, \omega)$) and the logarithm of the exponentially decaying amplitude scaled by the distance ($\ln[r\Phi_{AC}(r, \omega)]$) are linearly changing as a function of source-detector separation (r). When fitting a line to the amplitudes and phase information over distance, a slope change can be observed with changing optical properties. Specifically, an increase in μ_a will lead to a faster decay of the amplitude signal, and to a decrease of the phase delay, thus the positive slope becomes smaller.

Similarly for increases in μ'_s the amplitude will decay quicker, thus larger negative slope, and the phase angle slope will increase. The amplitude slope (S_{AC}) and phase angle slope (S_θ) can be calculated as partial derivatives over the source detector distance [180–182]:

$$S_{AC} = \frac{d}{dr} \ln[r\Phi_{AC}(r, \omega)] = -\sqrt{\frac{3\mu_a(\mu'_s + \mu_a)}{2}} \sqrt{\sqrt{1 + \left(\frac{\omega}{c_n\mu_a}\right)^2} + 1}, \quad (2.26)$$

$$S_\theta = \frac{d}{dr} \theta(r, \omega) = \sqrt{\frac{3\mu_a(\mu'_s + \mu_a)}{2}} \sqrt{\sqrt{1 + \left(\frac{\omega}{c_n\mu_a}\right)^2} - 1}. \quad (2.27)$$

When measuring with FD-NIRS at multiple distances, one can create the linear plots in Figure 2.3c for any given point in time. Note that as of now an infinite medium was assumed. When implying a more realistic model of semi-infinite medium, using a border to place source and detector components targeted into an optically semi-infinite medium, the linearity assumption of $\ln[r\Phi_{AC}(r, \omega)]$ no longer holds. It can be regained by an approximation that yields $\ln[r^2\Phi_{AC}(r, \omega)]$. Derivations of this approximation can be found elsewhere (e.g. Bigio and Fantini, Chapter 12.6, [166]). Equations 2.26 and 2.27 can now be used in conjunction to solve for the absolute values of μ_a and μ'_s . Here, μ_a and μ'_s are dependent on the slopes that one can measure, in addition to known constants of modulation frequency (here: $\omega = 110\text{MHz}$) and the speed of light in the medium (here: $c_n = 3 \times 10^{10}/1.3\text{cm/s}$)

$$\mu_a = \frac{\omega}{2c_n} \left(\frac{S_\theta}{S_{AC}} - \frac{s_{AC}}{S_\theta} \right), \quad (2.28)$$

$$\mu'_s = -\frac{2c_n}{3\omega} S_{AC} S_\theta - \mu_a. \quad (2.29)$$

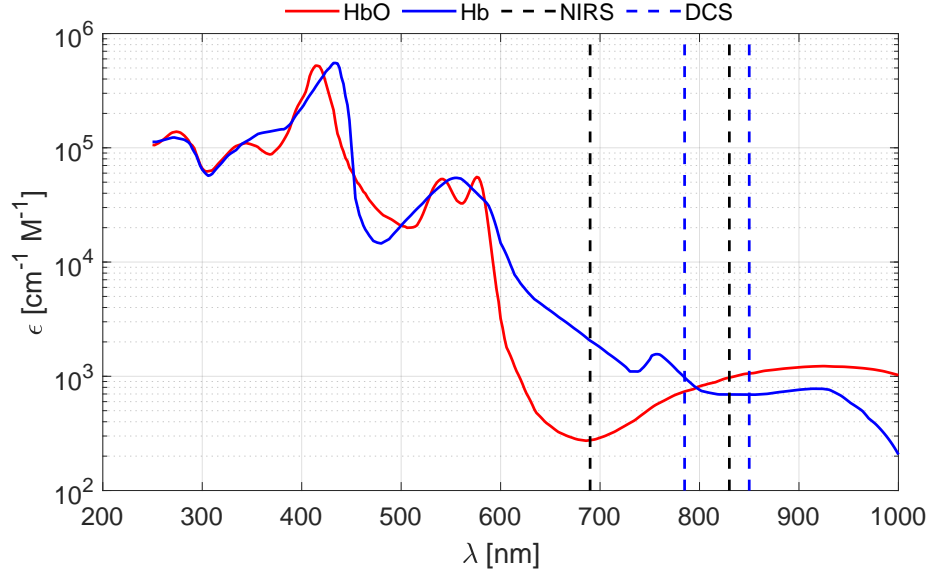


Figure 2.4: The spectrum shows the molar extinction coefficients for oxygenated hemoglobin (HbO, red) and deoxygenated hemoglobin (Hb, blue). The black dashed lines mark the wavelengths used in the NIRS system described below, the blue dashed line are wavelengths used in DCS. The data was collected by Scott Prahl from multiple sources and presented in [183]

2.3.4 Hemoglobin Concentration Calculation

Regardless of the calculation of $\Delta\mu_a(\lambda)$ or $\mu_a(\lambda)$, the corresponding hemoglobin concentration ΔHbO and ΔHb , or HbO and Hb , can be calculated using equation 2.7, given the molar extinction coefficients. Latter are listed in Figure 2.4 for oxygenated (red) and deoxygenated, or reduced, (blue) hemoglobin. Given that in the optical window between 600 and 900 nm absorption of lipids, water and melanin is significantly smaller than hemoglobin, and that they are largely static compared to the blood circulation, it is sufficient to only consider these two chromophores in the applications discussed in this thesis. From

$$\mu_a(\lambda) = C_{HbO}\epsilon_{HbO}(\lambda) + C_{Hb}\epsilon_{Hb}(\lambda), \quad (2.30)$$

one can see that two unknown concentrations (C_{HbO} and C_{Hb}), two literature based extinction coefficients ($\epsilon_{HbO}(\lambda)$ and $\epsilon_{Hb}(\lambda)$) and one measured value $\mu_a(\lambda)$ are given, making this an under defined system. To overcome this shortage, measuring at two wavelength, here $\lambda_1 = 690nm$ and $\lambda_2 = 830nm$, creates a solvable equation system. The wavelength (black dashed lines in Figure 2.4) lie on either side of the isosbestic point, i.e. the point of equal molar extinction coefficient at approx. 800nm, making the shorter wavelength weighted towards Hb and the longer wavelength weighted towards HbO . While the choice of wavelength is mathematically speaking irrelevant (with the exception of the isosbestic points), it has been shown in practice to improve signal quality to chose wavelength on either side.

Using these two wavelength, the following system follows:

$$\begin{aligned}\mu_a(\lambda_1) &= C_{HbO}\epsilon_{HbO}(\lambda_1) + C_{Hb}\epsilon_{Hb}(\lambda_1), \\ \mu_a(\lambda_2) &= C_{HbO}\epsilon_{HbO}(\lambda_2) + C_{Hb}\epsilon_{Hb}(\lambda_2),\end{aligned}\tag{2.31}$$

which, solved for chromophore concentration, yields the following system:

$$\begin{aligned}C_{HbO} &= \frac{\epsilon_{Hb}(\lambda_2)\mu_a(\lambda_1) - \epsilon_{Hb}(\lambda_1)\mu_a(\lambda_2)}{\epsilon_{HbO}(\lambda_1)\epsilon_{Hb}(\lambda_2) - \epsilon_{HbO}(\lambda_2)\epsilon_{Hb}(\lambda_1)}, \\ C_{Hb} &= \frac{\epsilon_{HbO}(\lambda_1)\mu_a(\lambda_2) - \epsilon_{HbO}(\lambda_2)\mu_a(\lambda_1)}{\epsilon_{HbO}(\lambda_1)\epsilon_{Hb}(\lambda_2) - \epsilon_{HbO}(\lambda_2)\epsilon_{Hb}(\lambda_1)}.\end{aligned}\tag{2.32}$$

Note that μ_a can be exchanged for $\Delta\mu_a$, which then calculates ΔHbO and ΔHb instead. Molar extinction coefficients are unaffected by this change.

2.4 Diffuse Correlation Spectroscopy

While NIRS can be used to measure hemoglobin concentrations and subsequently tissue saturation of oxygenated hemoglobin (StO_2) and CBV, it is also desirable to measure blood flow in many medical settings. A diffuse optical method was developed named Diffuse Correlation Spectroscopy (DCS) that can estimate the flow of red blood cells in human tissue [184–186]. The general idea is that the human tissue has a portion of static scattering structures and a portion of moving scattering objects. The latter ones are predominantly red blood cells. Blood flow can be estimated by measuring the movement of red blood cells in the tissue. DCS uses auto-correlation of light intensity speckles created inside the tissue due to constructive and destructive interference of a highly monochromatic laser light source. The speckle pattern inside the tissue changes faster with faster red blood cell movement, and thus loses auto-correlation at an earlier delay times. The method has been shown to correlate well with Doppler ultrasound and other blood flow measurement methods [185].

2.4.1 Electric Field Auto-Correlation

First, the electric field auto-correlation of light in turbid media has to be described, from which a diffusion equation expression can be derived that will allow the relation of measurements of light intensity to movement of light scattering particles.

The light electric field temporal auto-correlation at position r , time t , and for propagation along

$\hat{\Omega}$ can be expressed as

$$G_1^T(r, \hat{\Omega}, \tau) = \langle E(r, \hat{\Omega}, t) E^*(r, \hat{\Omega}, t + \tau) \rangle, \quad (2.33)$$

where $E(r, \hat{\Omega}, t)$ is the total light electric field, * denotes the complex conjugate and $\langle \rangle$ denotes the time or ensemble average. Here, τ is the delay time in the auto-correlation, which in the case of micro-vasculature blood flow typically has a range of μs to ms . Equation 2.33 obeys a correlation diffusion equation that is analogous to the Boltzmann transport equation (see Equation 2.10) [187, 188]. This naturally lends itself to apply similar simplifications and boundary conditions as in chapter 2.2.1, leading to the diffusion equation (2.12), such as the P_1 approximation and $\mu'_s \gg \mu_a$. One can calculate the angle independent electric field auto-correlation by

$$G_1(r, t) = \int_{4\pi} G_1^T(r, \hat{\Omega}, \tau) d\Omega, \quad (2.34)$$

which yields the *correlation diffusion equation* [184]

$$\nabla \cdot [D \nabla G_1(r, \tau)] - \left[c_n \mu_a + \frac{1}{3} c_n \mu'_s k_0^2 \langle \Delta r^2(\tau) \rangle \right] G_1(r, \tau) = -S_0(r). \quad (2.35)$$

Here, k_0 is the wave number $\frac{2\pi}{\lambda}$, $S_0(r)$ is an isotropic light source and $\langle \Delta r^2(\tau) \rangle$ is the average scatterer displacement. A commonly used displacement approximation is the Brownian diffusion [184]:

$$\langle \Delta r^2(\tau) \rangle = 6D_B \tau, \quad (2.36)$$

with D_B as the Brownian diffusion coefficient. Under the assumption of a semi-infinite medium and isotropic scattering, equation 2.35 yields

$$G_1(\rho, \tau) = \frac{3\mu'_s}{4\pi} \left[\frac{e^{Kr_1}}{r_1} - \frac{e^{Kr_2}}{r_2} \right], \quad (2.37)$$

where,

$$\begin{aligned} K &= \sqrt{3\mu_a\mu'_s + \mu_s'^2 k_0^2 \alpha \langle \Delta r^2(\tau) \rangle}, \\ r_1 &= \sqrt{\rho^2 + \frac{1}{\mu'_s}}, \\ r_2 &= \sqrt{\rho^2 + \left(\frac{1}{\mu'_s} + 2z_b \right)^2}, \\ z_b &= \sqrt{\frac{2(1 + R_{eff})}{3\mu'_s(1 - R_{eff})}}. \end{aligned} \quad (2.38)$$

R_{eff} is the effective reflection coefficient, which can be approximated as $R_{eff} \approx -1.44n^{-2} + 0.71n^{-1} + 0.668 + 0.00636n$ [189], where for this work $n = n_{in}/n_{out}$ is the refractive index ratio between inside (≈ 1.33 for tissue) and outside (1 for air) the medium. ρ is the source-detector distance and α is the ratio of moving scatters to static scatterers, which is therefore related to the hematocrit, i.e. the volume percentage of red blood cells in blood.

2.4.2 Intensity Auto-Correlation

To measure with DCS, speckle fluctuations of highly monochromatic light, characterized by long coherence lengths, will be observed. Under these conditions, light creates a speckle pattern inside the highly scattering tissue. This is due to constructive and destructive interference of the light with itself as it is scattered in different directions inside the tissue, creating spots, or speckles, of

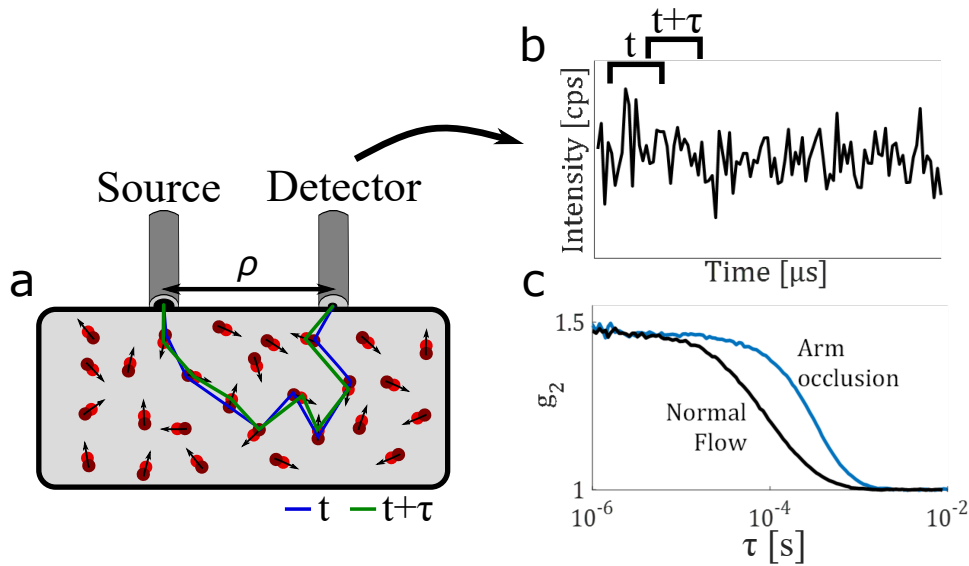


Figure 2.5: Long coherence length laser light (highly monochromatic) is send into tissue with moving scatterers, depicted by moving red circles in a). The shift in moving particles causes speckle pattern change, recorded as light intensity fluctuations in b). Using a moving correlation window, an intensity auto-correlation plot can be calculated as seen in c). Higher flow leads to stronger fluctuations in light intensity and a faster decorrelation (black), whereas low flow maintains a high correlation over a longer lag time τ , for example during arm occlusion (blue).

high and low light intensity. Observing changes in speckle patterns has previously been used to measure flow on surfaces of scattering medium, using a technique called *laser speckle contrast imaging* [190]. Here, the image of a speckle pattern is taken with a given exposure time of the camera. Non-moving scatterers will create a very sharp speckle pattern while regions of high flow of scatterers will appear blurry due to their movement and constantly changing speckle creation. Laser speckle contrast imaging can only measure superficial flow on skin or the exposed organs [191]. Similarly to the degree of blurriness of the image correlating to blood flow, one can observe flow driven speckle changes in DCS as a loss of intensity auto-correlations. Instead of using a camera to observe a large field of view superficially, source and detector fibers are placed on the surface of the medium. DCS is therefore as sensitive to deeper layers of tissue as previously described NIRS methods, in that it follows the probability density function of light

propagation described in Figure 2.2.

To observe a single speckle in deeper tissue using DCS, single-mode fibers are used whose fiber core diameter is small enough to not allow multiple simultaneous modes of light propagating at once. Thus, the detectors needed for DCS are single photon counting modules. The conceptual idea of measuring light intensity fluctuations over time to determine the movement of scattering particles by auto-correlation of said intensity is schematically demonstrated in Figure 2.5.

When photon intensities is measured at sampling rates of $> 1MHz$ and an auto-correlation of the input intensity for moving windows of milliseconds length (e.g. $\approx 50ms$) over delay times of $1\mu s > \tau > 10ms$ is calculated, normalized intensity auto-correlation curves, defined as $g_2(\tau)$, are gained (Figure 2.5c). Given that the normalized intensity auto-correlation

$$g_2(\tau) = \frac{\langle I(t)I(t+\tau) \rangle}{\langle I(t) \rangle^2}, \quad (2.39)$$

is related to the normalized electric field auto-correlation

$$g_1(\tau) = \frac{\langle E^*(t)E(\tau+t) \rangle}{\langle |E(t)|^2 \rangle}, \quad (2.40)$$

by $I(t) = |E(t)|^2$, one can be converted into the other. The Siegert relation [192]

$$g_2(\tau) = 1 + \beta |g_1(\tau)|^2 \quad (2.41)$$

is thus used to extract $g_1(\tau)$ from the measurable $g_2(\tau)$. Here β is a constant determined by the collection optics. By the use of single-mode fibers, a value of $\beta \approx 0.5$ is expected. It can be ap-

proximated by extrapolating $g_1(0)$ from the measurement. Note that $g_1(\tau) = G_1(\rho, \tau)/G_1(\rho, 0)$, where $G_1(\rho, 0)$ is assuming no scatterer displacement, which reduces the complex K term to $K = \sqrt{3\mu_a\mu'_s}$.

Under assumptions of μ_a , μ'_s , n , and a known ρ , a mathematical model described in equations 2.37 and 2.38 can be fitted to the measurement results. The fitting parameter that is alternated in a least mean-square-error fit, is the mean-displacement $\alpha\langle\Delta r^2(\tau)\rangle$. Note that the α -term is still present, meaning that the number of moving scatterers and the degree of displacement are entangled. The outcome of the fitting procedure is therefore a scaled diffusion coefficient αD_b , with units of s/cm^2 . While αD_b is not an absolute measure of blood flow or blood flow velocity, it has been shown to be highly correlated and to scale with absolute blood flow measured by various modalities for brain blood flow measurements, including transcranial Doppler Ultrasound [193] and ASL-MRI [194–196].

Instruments used for research presented in this thesis are based on lasers using either 785 nm or 850nm, as indicated in Figure 2.4. Note that DCS only needs one wavelength while NIRS requires two. NIRS and DCS are often operated in conjunction with each other, which is why the 850 nm wavelength is preferred. This is because an optical short pass filter can be used to block DCS light from entering the NIRS sensors, given that DCS operates at light powers of $> 30\text{ mW}$, while NIRS light sources emit less than 5 mW.

Chapter 3

Non-Invasive Measurement of Intracranial Pressure

The need for non-invasive ICP monitors is discussed in Chapter 1.1.5, and methods for ICP measurements are shown in Chapter 1.1.6. Here I will propose two methods to measure ICP with non-invasive instruments based on near-infrared light. An estimation of relative changes, or fluctuations in ICP is performed using changes in HbO over time, measured with NIRS. Estimations of absolute ICP values, or ICP offsets, are done based on CBF measurements with DCS. An overview of the two approaches is given in Figure 3.1. The performance for one example measurement for the combination of both approaches is briefly described in Chapter 3.3.

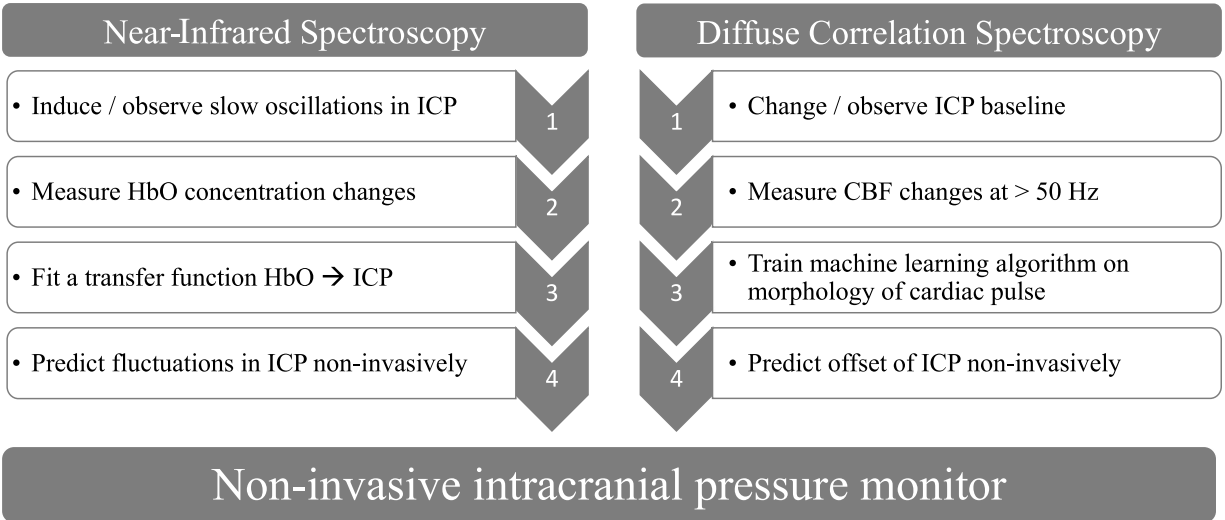


Figure 3.1: Schematic overview of the research approach for the development of a non-invasive intracranial pressure sensor on the basis of diffuse optics.

3.1 Estimation of Intracranial Pressure Fluctuations

Near-infrared spectroscopy (NIRS) (see Chapter 2.3) has been tested clinically [71, 197], but extrapolation of NIRS-based signals into ICP measurements were limited by the lack of a general data analysis strategy. To this end, we introduce an experimental model where ICP baseline changes and oscillations were induced incrementally through fluid infusion in non-human primates (NHP), a situation comparable to hydrocephalus. We demonstrate that NIRS and ICP are related in this setting, and we build a transfer function approach to translate HbO changes measured non-invasively with NIRS into ICP changes. Finally, we extrapolate to a clinical picture incorporating ICP, CPP, and CA as a fuller indication of vascular changes which may be associated with diagnostic and prognostic indicators [198–203].

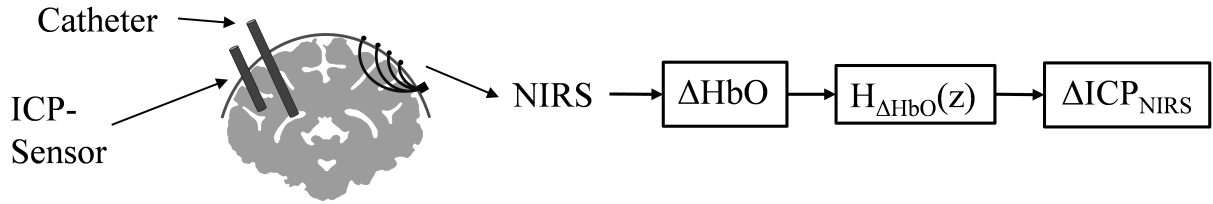


Figure 3.2: Experimental setup, showing the placement of the ICP sensor in the brain matter, the ventricular catheter and the NIRS probe. Hemodynamic responses from NIRS, here changes in oxygenated hemoglobin (ΔHbO), were used to estimate a transfer function to calculate estimates of non-invasive ICP_{NIRS} changes.

3.1.1 Materials and Methods

Changes in ICP were induced via changes in fluid volume in non-human primates (NHP), mimicking a form of hydrocephalus. ICP was altered actively by fluid injection *via* an intraventricular catheter and monitored with a traditional intraparenchymal ICP sensor, while hemoglobin concentration changes were measured non-invasively at the scalp with NIRS. The proposed approach is illustrated in Figure 3.2. The NIRS-based hemodynamic response was used to fit a transfer function that translates changes in oxygenated hemoglobin concentration into changes in ICP. We will refer to the estimated ICP as ICP_{NIRS} , to invasively measured intraparenchymal ICP as ICP_{ip} , and the conceptual idea of pressure as ICP.

3.1.1.1 Animal Model and Intraparenchymal Pressure Probe Placement

Seven healthy male rhesus macaques (*Macaca mulatta*) with an average age of 8.3 ± 1.7 years and an average weight of 10.5 ± 2.5 kg were used in these experiments. All procedures were approved by the Institutional Animal Care and Use Committee of the University of Pittsburgh and complied with guidelines set forth in the National Institute of Health's *Guide for the Care and Use of Laboratory Animals*. The facilities at the University of Pittsburgh are accredited

by the Association for Assessment and Accreditation of Laboratory Animal Care International (AAALAC) and in compliance with the Standards for Humane Care and Use of Laboratory Animals of the Office of Laboratory Animal Welfare (OLAW D16-00118). Furthermore, this manuscript is in compliance with the Animal Research: Reporting In Vivo Experiments (ARRIVE) guidelines. All NHPs were initially sedated using 20 mg/kg of Ketamine, 1 mg/kg Diazepam, and 0.04 mg/kg Atropine in the home cage. In the surgery room, animals were intubated and maintained under anesthesia using 1-3% Isoflurane. After placing the A-line into the carotid artery for Arterial Blood Pressure (ABP) measurements, animals were ventilated and given a paralytic, vecuronium bromide (0.1 mg/kg/hr). Data streams of ICP_{ip} and ABP were recorded at 100 Hz using an MPR1 Datalogger from Raumedic. In order to monitor ICP_{ip} with the traditional intraparenchymal probe and to manipulate pressure *via* intraventricular fluid infusion, the skull was exposed and two small craniotomies were made to place the ICP_{ip} sensor (Precision Pressure Catheter, Raumedic Helmbrechts, Germany) into the brain frontal lobe parenchyma and a catheter in the lateral ventricle for fluid injection (Lumbar Catheter, Medtronic, Minneapolis MN). The holes were then sealed with bone wax to reduce the possibility of cerebrospinal fluid leakage.

The intraventricular catheter was connected to a saline reservoir. Changing the height of the reservoir relative to the animal's head induced a pressure change through gravitational force. Alternatively, in three animals ICP was changed by connecting the ventricular catheter to a syringe pump which applied mechanical force. While the gravitational system maintained a more stable elevated ICP baseline, the syringe pump allowed for fluid volume control and faster changes. An overview of the induced ICP changes and each system used to change ICP is given in Figure

3.3. The baseline of ICP was changed from normal pressure (about 3-10 mmHg) in increments of 3 mmHg until reaching 15 mmHg, at which point pressure was increased in increments of 10 mmHg to a total height of 40 mmHg, which is considered severely elevated. At each baseline value, ICP oscillations were induced by rotating the reservoir or oscillating the piston in the syringe pump. The oscillations were set to five different frequencies distributed between 0.009 Hz and 0.059 Hz. These frequencies were chosen to fall before and after previously published autoregulatory cutoff frequencies [150, 151]. The order of ICP oscillation frequency was randomized once and then held the same in all experiments (see Figure 3.3). Due to the shorter duration of faster frequencies, the highest frequency was induced for eight periods, while all others were induced for four periods. This ensured enough signal length for later processing steps, including the elimination of noise and extraneous signals such as respiration that were unrelated to our primary goals. Each experiment lasted for a period of 10 to 15 hours.

3.1.1.2 Near Infrared Spectroscopy for Extracranial ICP Measurements

Cerebral hemoglobin concentration changes were measured with a multi-distance, frequency domain NIRS system, the OxiplexTS (ISS Inc., Champaign, IL, USA). Two wavelengths were used to illuminate the tissue, 690 nm and 830 nm. Source detector distances were set to 0.75 cm, 1.33 cm, 1.66 cm and 2 cm. The optical fibers were placed directly on the exposed skull to avoid contamination of the signal by blood circulation in the muscle and skin tissue. In all animals, the probes were placed over the visual cortex just anterior to the occipital pole, maximizing the distance from the point of fluid injection. Data were acquired at 5 Hz, sufficient to capture slow physiological waves and heart and respiration rates.

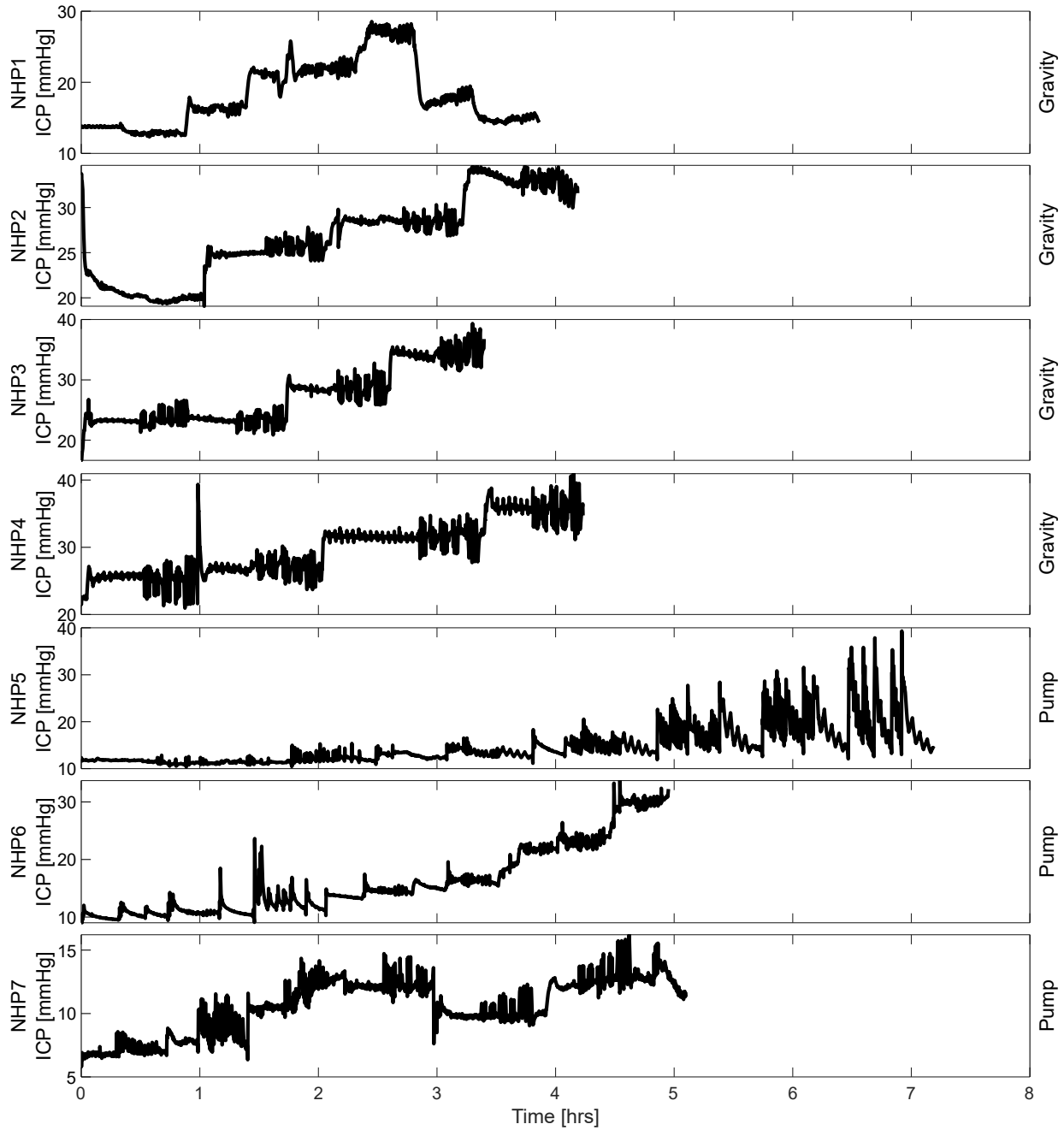


Figure 3.3: Induced ICP_{ip} changes are shown over time for the seven NHP. For the first four animals a gravitational system was used to influence ICP, for the last three a syringe pump forced the fluid through the ventricular catheter to increase the ICP. NHP 5 shows a lack of stable baseline increases, which is why for NHP 6 and 7 a second catheter was placed to allow for stable ICP_{ip} baseline while ICP_{ip} was oscillated using the syringe.

For calculating hemodynamic changes over time, the modified Beer-Lambert law (see Chapter 2.3.2) was used based on the second longest source-detector separation (1.66 cm). The modified Beer-Lambert law translates light attenuation from two wavelengths into hemoglobin concentration changes [173]. Temporal changes in oxygenated (ΔHbO), deoxygenated (ΔHb), and total ($\Delta\text{HbT} = \Delta\text{HbO} + \Delta\text{Hb}$) hemoglobin concentration were used for the calculations described below.

3.1.1.3 Signal Processing

The 100 Hz ICP_{ip} data were down-sampled by first applying a low-pass filter to prevent aliasing and then selecting every 20th data point, resulting in a 5 Hz data-sampling rate, matching the optical data. Based on simultaneously placed markers during the recording, the pressure and hemodynamic data were aligned and truncated to be equal length. Using a narrow band-pass filter around the induced frequencies, a single frequency signal was approximated and extracted. Given the nature of the narrow band-pass, potential baseline drifts and artifacts were removed in this process and no further preparations of the signals were needed. The single frequency segment was then treated as an independent measurement (see Figure 3.4). To account for small variations in the frequency content from the intended frequency values shown in Table 3.1, the actual induced frequencies were extracted from the ICP_{ip} data through auto-correlation. Narrow band pass filtering around the induced frequencies was derived from the Parks-McClellan algorithm[204] for optimal finite response (FIR) filter design ('firpm', MATLAB, The Math-Works Inc., Natick, MA, USA). The high filter order of $N \geq 2000$ was estimated by the Parks-

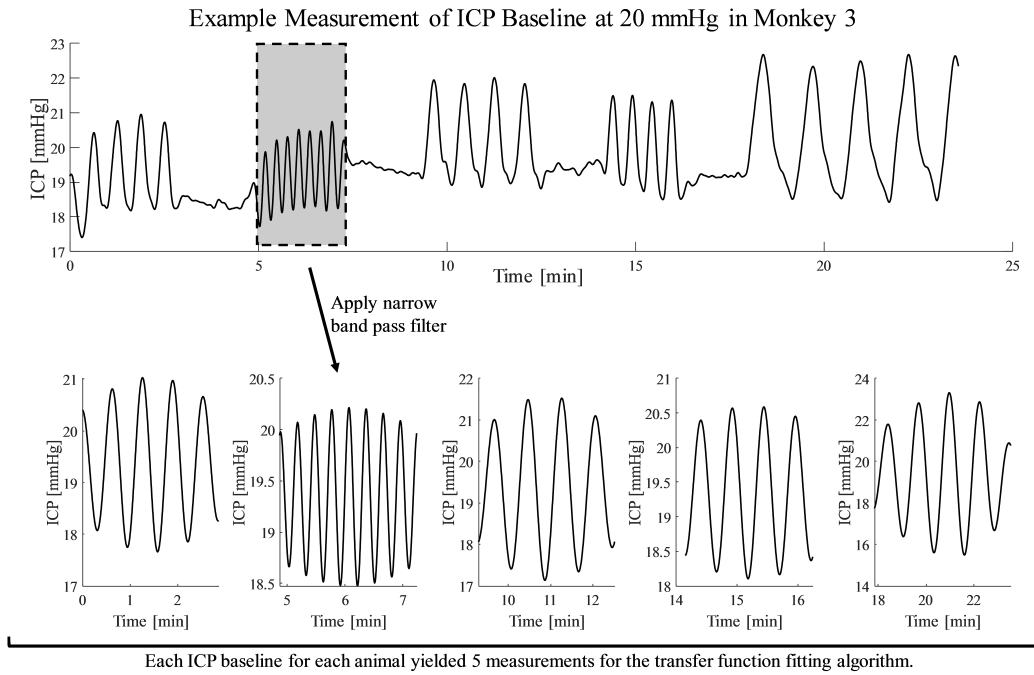


Figure 3.4: Example ICP_{ip} data from one animal. The raw data (top graph) was filtered around the induced frequencies. The period at which each frequency was induced was then treated as an independent measurement available for data fitting.

Table 3.1: Defined order and number of full rounds of each induced frequency.

Order	Frequency [Hz]	# of Oscillations
1	0.025	4
1	0.059	8
1	0.017	4
1	0.033	4
1	0.009	4

McCellan algorithm ('firpmord', MATLAB, The MathWorks Inc., Natick, MA, USA). High order filters were used to remove all signals except the induced frequency content from ICP_{ip} oscillation.

Using the Hilbert transform, the magnitude and phase information of the filtered signal were calculated. A measurement was discarded as unstable if the standard deviation of the phase difference between ΔHbO and ΔHb exceeded 30° , corresponding to unstable physiological responses to ICP oscillations. Furthermore, a measurement was discarded if the magnitude of ΔHbO at the induced frequencies did not exceed the noise level. Noise was defined as the magnitude of the same frequency at a time where no ICP oscillations were induced.

3.1.1.4 Transfer Function Analysis

Based on the extracted frequency content described above, a leave-one-out cross-validation was performed to estimate a generalized transfer function while avoiding over-fitting [205]. Each of the five different frequencies induced during one baseline level of ICP was considered a separate input to the transfer function estimation. This method increased the amount of data sets available for cross-validation. The total amount of 38 measurements times 5 frequencies produced 190 data sets. After applying the signal quality criteria, 33 of these measurements were excluded, leaving 157 remaining data sets available for cross-validation.

Through L-curve analysis, the balance between precision and generalization was set at four poles and two zeros for the discrete-time, frequency domain transfer function. Under these conditions the "fz" function (MATLAB, The MathWorks Inc., Natick, MA, USA) was used for data fitting.

This algorithm optimizes the numerator and denominator of the transfer function based on a non-linear least-squares algorithm [206]. The numerator and denominator of the fitted transfer function of the leave-one-out cross-validation were averaged. This averaged transfer function was then applied to low-pass filtered hemoglobin concentration measurements. Specifically, the estimated transfer function was then applied to low pass filtered data, cutting off at 0.1 Hz, with a lower filter order of $N = 3$. All filters were applied using MATLABs "filtfilt" function (MATLAB, The MathWorks Inc., Natick, MA, USA), which guaranties a zero-phase delay by applying the filter in both forward and backward direction. The final validation was therefore based on partially unknown data with a much wider frequency range than the narrow band filtered data used for finding the transfer function.

3.1.2 Results

We measured cerebral hemodynamic changes non-invasively with NIRS in seven anesthetized non-human primates in which we were able to manipulate and measure ICP directly. In order to ensure good contact of the probe with the animal, data fidelity was checked by observing expected natural hemodynamic changes in the NIRS data (i.e., respiration and heartbeat oscillations), and later confirmed in the form of a fast Fourier transform (FFT). We observed heart rate and respiration frequencies in the FFTs of all animals used. A spectrogram of a representative measurement illustrating the frequency content over time can be found in Figure 3.5. Baseline step increases in ICP were recorded for each trial by the conventional intraparenchymal pressure probe, as well as ABP, CPP, ΔHbO , and ΔHb . Figure 3.6 shows ICP oscillations had a notable effect on the hemodynamics, but did not induce oscillations in ABP. The data in this graph has

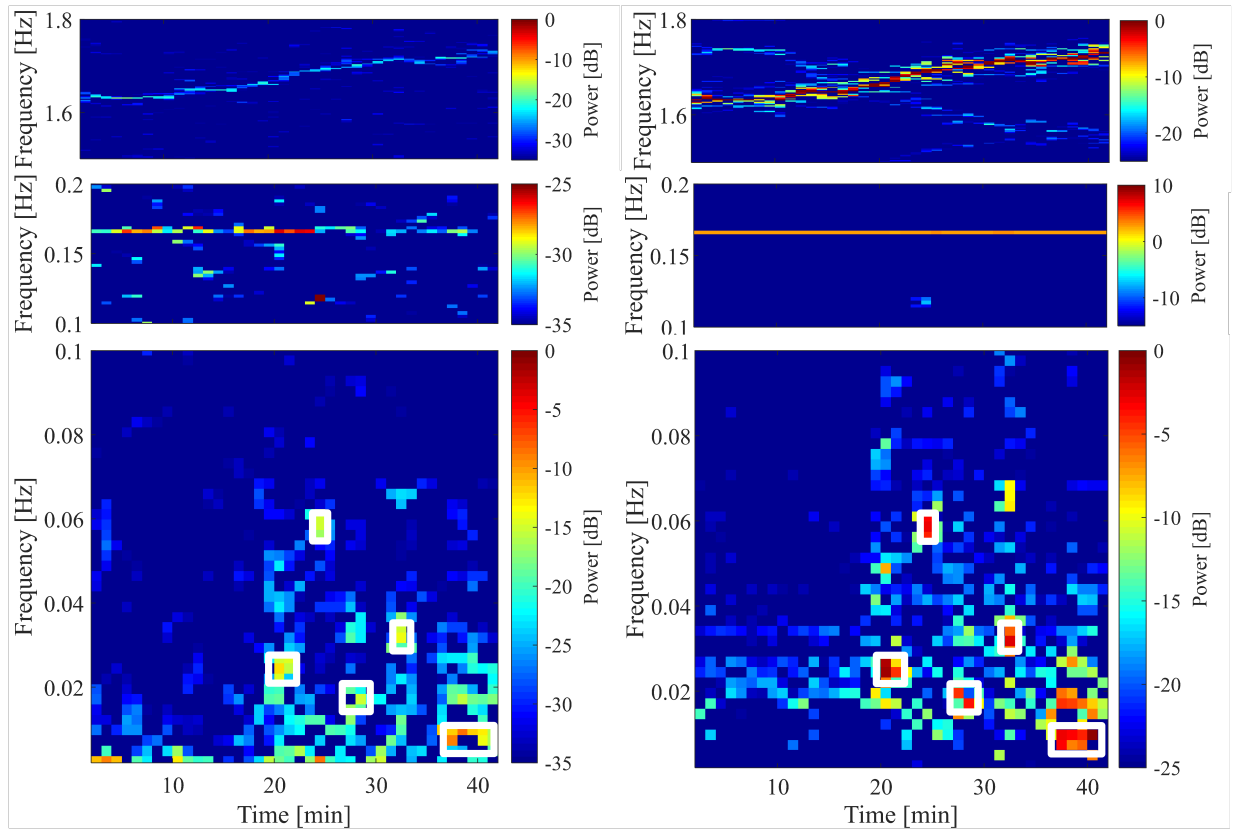


Figure 3.5: The top two graphs illustrate the spectral power color-coded as a function of frequency (y-axis) and time (x-axis). The left plots show ΔHbO while the right plots show ICP_{ip} . The drift in heart rate can be observed in the top graphs while the middle graphs show respiration rate and the lower graphs are zoomed in to frequencies below 0.1 Hz. Here, the expected spectral power increases in certain time frames for pre-defined frequencies (according to induced ICP oscillations) are highlighted by white boxes. The oscillations induced in ICP_{ip} can also be found in ΔHbO .

been low-pass filtered to eliminate respiration and heart-rate influences on the signal. We first evaluated whether the magnitudes of HbO alone as measured by extracranial NIRS were consistent with the changes in ICP observed *via* the invasive parenchymal probe. Using the narrow band pass filtered data, the magnitudes of the induced oscillations were extracted by means of the Hilbert transform. Figure 3.7 shows the relationship between HbO magnitudes and ICP_{ip} magnitudes, where each dot corresponds to one of the 157 single frequency data sets. The red curve represents a linear fit, while the dashed black line indicates a function with the slope of 1. The magnitudes of ICP_{ip} obtained from the conventional intraparenchymal probe did not translate directly into HbO (Figure 3.7). In addition, the phase difference between HbO and ICP_{ip} was slightly larger than 180° , indicating the need for a more complex transfer function translating ΔHbO into ICP_{NIRS} . Signal to noise ratio (SNR) was defined as magnitudes of oscillation divided by the magnitudes of periods in which these oscillations were not induced into ICP. It thus yields a metric to understand which signal was influenced by ICP oscillations. High SNR was observed for ICP_{ip} , CPP, and hemodynamic measurements of ΔHbO , ΔHb and ΔHbT , as illustrated in Figure 3.8. We next measured the SNR at two different ICP baselines (Figure 3.8). Using an unpaired Student's t-test, no significant differences were found between SNR at 10 mmHg and 40 mmHg for ABP ($p = 0.21$). Thus, responses remained at or below the level of the noise, leaving the SNR below 1. All other signals showed a significant increase in SNR ($p < 0.05$) when treating all frequencies of one signal as a single group. Frequency dependent trends in the magnitude were observed at low ICP baseline values but reduced at highly elevated ICP, suggesting a loss of frequency dependent magnitude changes.

In order to account for frequency dependent and ICP baseline dependent changes in HbO, we fit

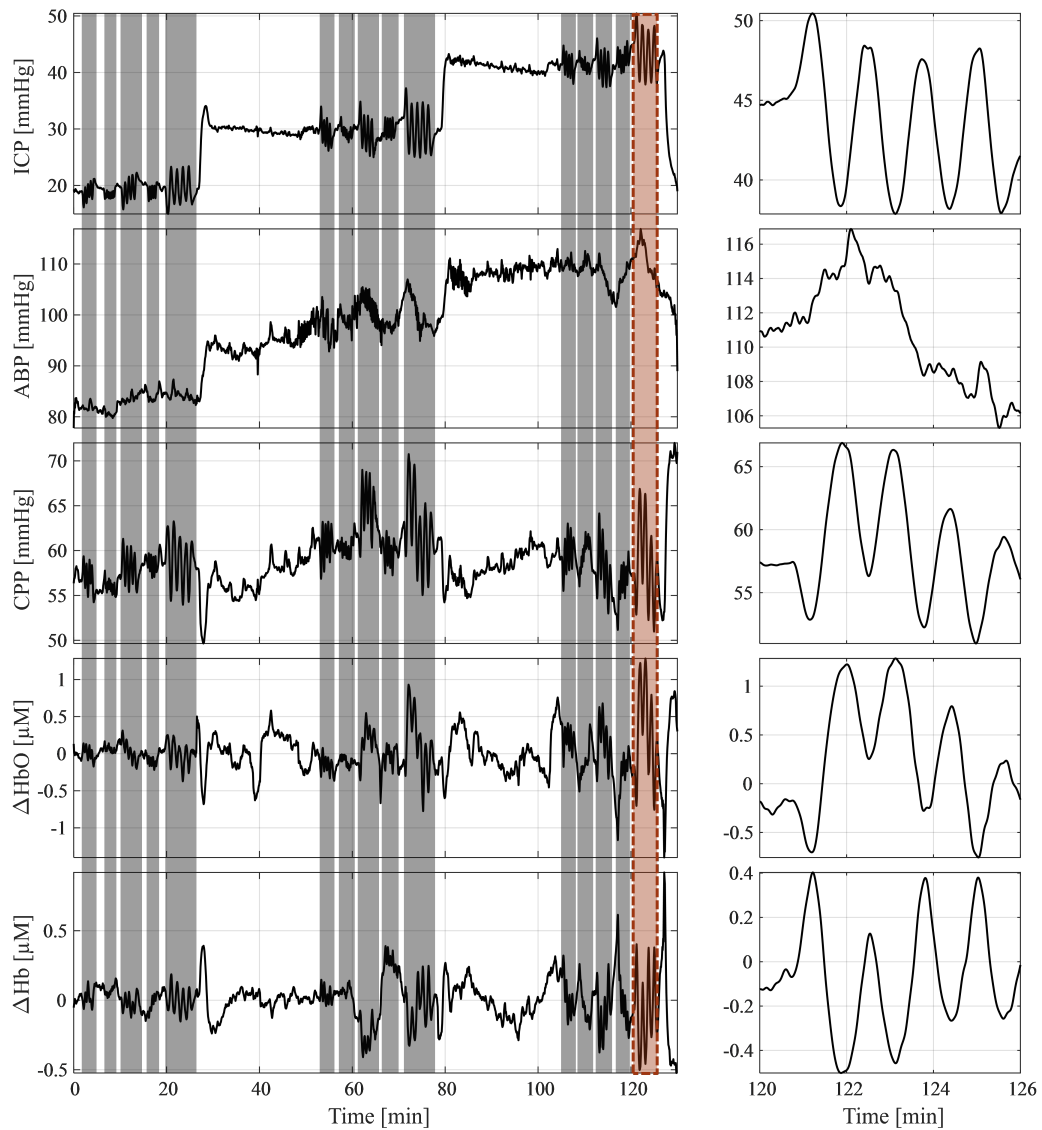


Figure 3.6: This representative measurement shows parts of the protocol. The top graph illustrates the baseline changes in ICP_{ip} with sinusoidal induced oscillations highlighted in grey. A close up of the induced oscillation indicated by the red background is shown on the right. Oscillations in ICP did not translate into ABP oscillations, shown in the second graph from the top. CPP, ΔHbO , and ΔHb showed oscillations corresponding to the ICP_{ip} change induced.

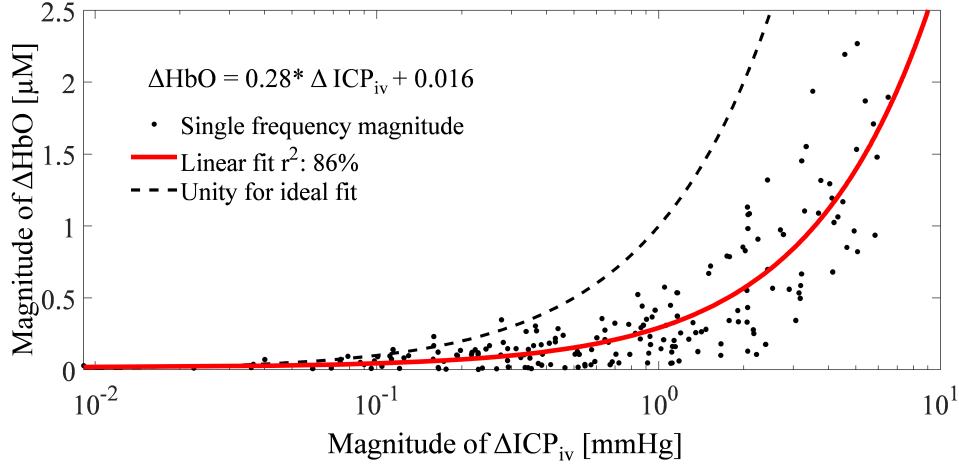


Figure 3.7: Linear relationship between oscillation magnitudes in ΔHbO and invasively measured $\Delta\text{ICP}_{\text{ip}}$. The linear fit is shown as a function in the top left. Note that the x-axis is shown in logarithmic scale to improve visibility of low magnitude data points. A unity line is shown for reference to indicate an ideal fit.

a transfer function to the hemodynamic data. The transfer function found, $H(z)$, is given by

$$H(z) = \frac{-0.22z + 0.22}{z^4 - 1.9z^3 + 0.22z^2 + 1.33z - 0.65}. \quad (3.1)$$

During the fitting, one of the zeros in the numerator was fitted to 0, such that the resulting transfer function is based on 1 zero and 4 poles. The outcome is visualized in the bode plot in Figure 3.9. The error bars represent the standard deviation over all cross-correlation subsets and show an increase in gain over frequency. Similarly, the phase difference changes over frequency, confirming a frequency dependence for the translation of HbO to ICP_{ip} . After applying the transfer function to low-pass filtered ΔHbO data of low filter order, the estimated, non-invasive $\Delta\text{ICP}_{\text{NIRS}}$ is plotted in Figure 3.10A. Since the transfer function was applied to low-pass filtered data rather than narrow band pass filtered data, the test signal has a higher frequency content than the data used to fit the transfer function. The top graph in Figure 3.10A shows time traces of

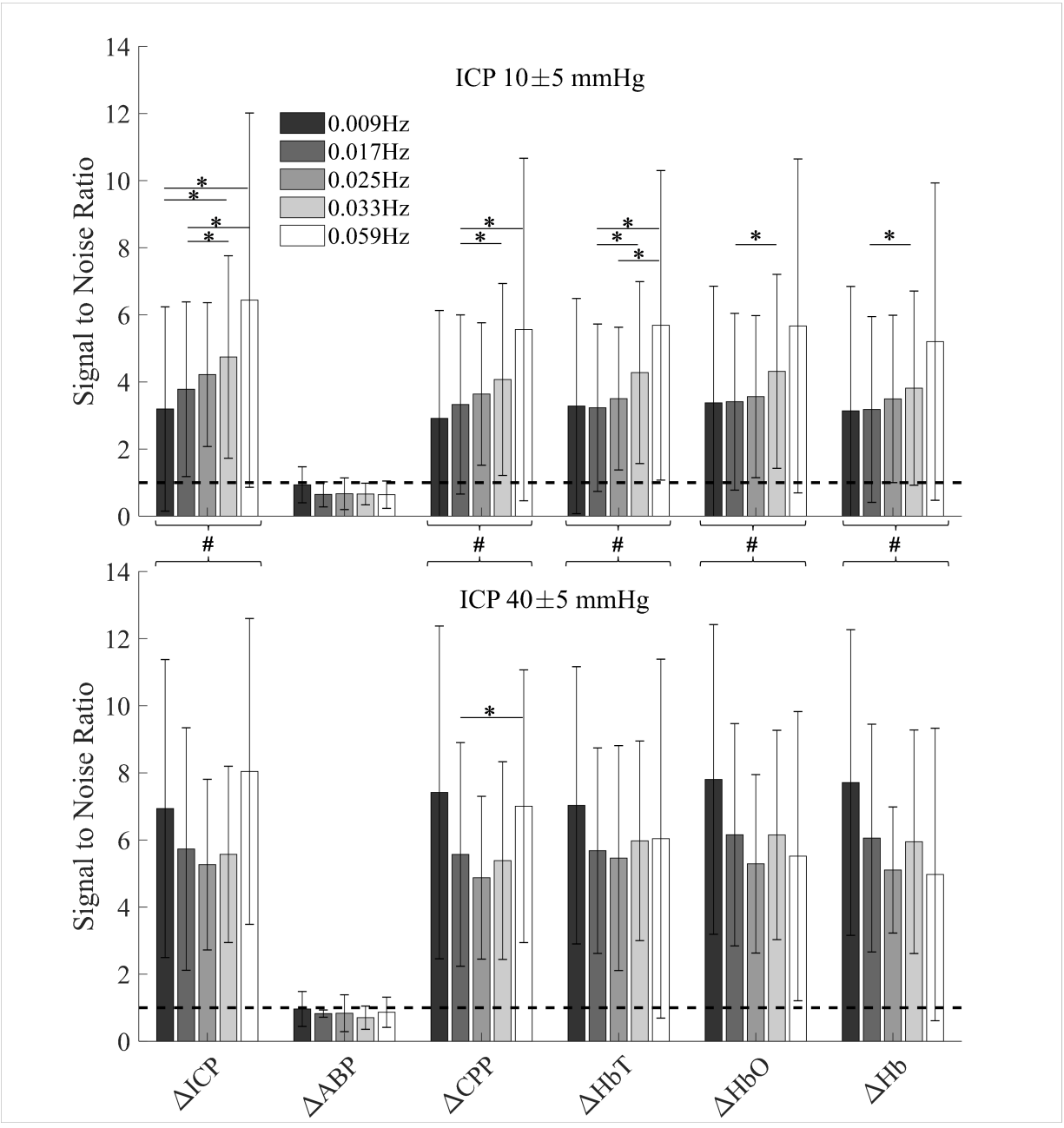


Figure 3.8: The signal to noise ratio (SNR) was calculated as the ratio of frequency specific amplitudes. The amplitude during ICP oscillation is considered the signal, while amplitude of the same frequency without induced ICP oscillation is considered noise. The dashed line shows the noise level at SNR = 1. Error bars show the standard deviation at every given frequency. Top: Healthy baseline ICP. Bottom: Highly elevated baseline ICP. A single asterisk indicates significantly different ($p < 0.05$) average SNR calculated by a paired t-test across frequencies within one signal type. The pound sign indicates significantly higher SNR in high ICP baseline ($p < 0.05$) as indicated by two-sample t-test when treating all frequencies of a signal as one group.

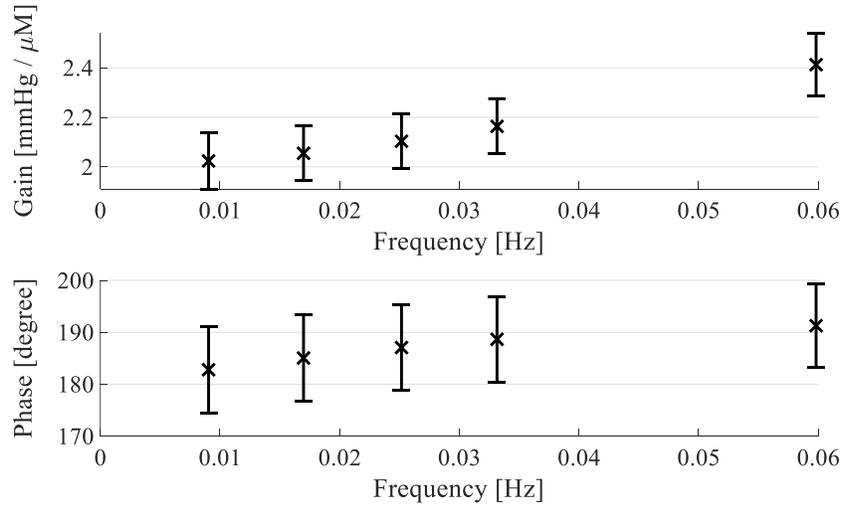


Figure 3.9: Bode plot of the found transfer function. The error bars show the standard deviation over all subsets of the cross-validation algorithm used to fit the transfer functions. The mean of all coefficients of all transfer functions is calculated and its gain (top) and phase delay (bottom) from ΔHbO to $\Delta\text{ICP}_{\text{ip}}$ is shown above.

ICP_{ip} (red line) and our calculated NIRS based ICP_{NIRS} (grey line). The time traces qualitatively match well in terms of amplitude as well as phase delay ($r^2=0.86$). The lower graph of Figure 3.10A represents a similar measurement at the same ICP baseline of 40 mmHg in a different animal. The transfer function result is underestimated but the dynamic trends nonetheless show high correlation ($r^2 = 0.57$). The over- and under-estimations are also evident in a magnitude comparison in Figure 3.10C. When comparing the magnitude differences to Figure 3.7, a clear improvement can be observed, as the linear fit (red line) now lies closer to the unity line (dashed line). The linear fit still lies below the unity line, indicating a tendency overall to underestimate the ICP_{ip} magnitudes.

Aside from the magnitude similarity, the minimization of phase lags between ICP_{NIRS} and invasively measured ICP (ICP_{ip}) is indicative of a good transfer function. Figure 3.10B shows the average phase delay between ΔHbO and $\Delta\text{ICP}_{\text{ip}}$ in red. Phase differences evolve around

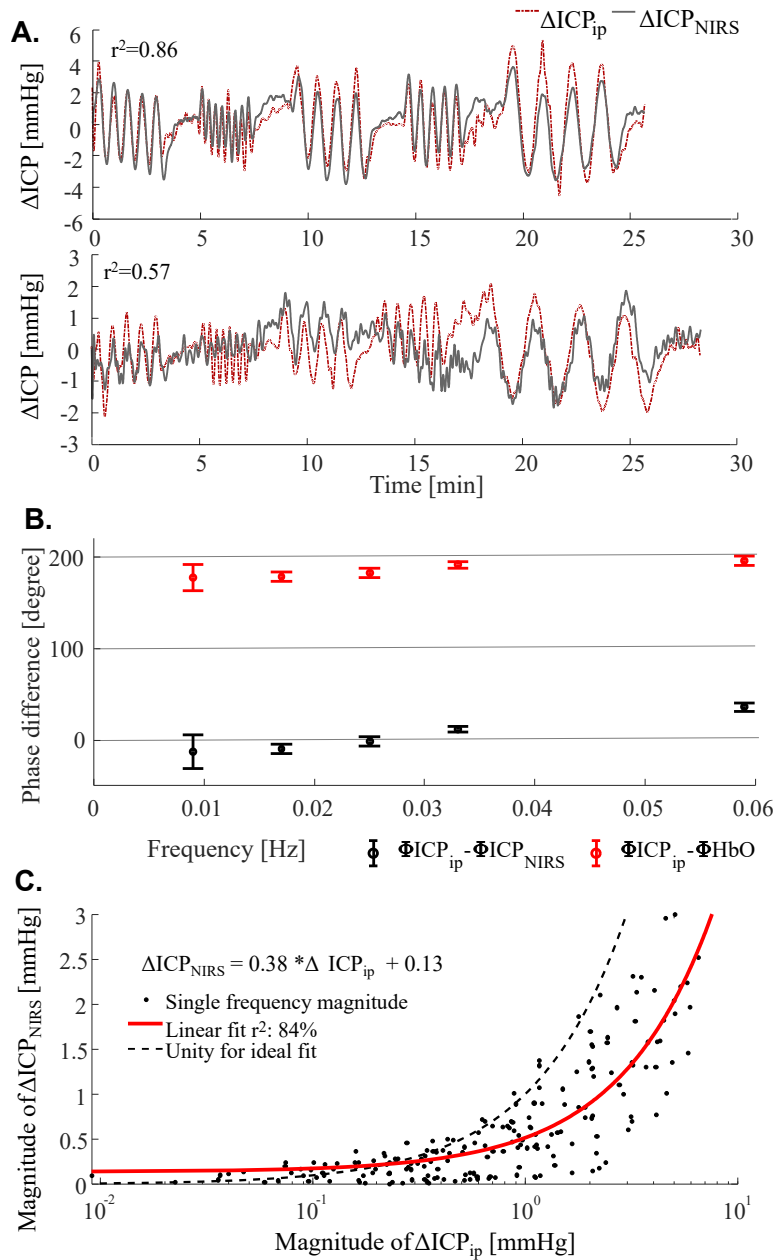


Figure 3.10: A) Comparison of invasive, parenchymal probe (dotted red line) and non-invasive NIRS (solid grey line) ICP measurements. Top: Representative example of animal 4 at a baseline of 40 mmHg. Bottom: Underestimation in animal 5 at a baseline of 40 mmHg. Pearson correlation is shown in the top left of both graphs. B) Phase difference between invasively measured ICP and estimated NIRS-based $\Delta\text{ICP}_{\text{NIRS}}$ is shown as black error bars. The error bar indicates the standard deviation and the cross indicates the mean phase difference over all 157 single-frequency data sets. Similarly, the red line indicates the phase difference between invasive ICP_{ip} and measured ΔHbO . C) Comparison of magnitudes after transfer function analysis. The red line indicates a linear fit to the magnitudes. The right-sided, downward shift compared to the ideal unity line indicates a tendency for underestimation of the oscillation magnitudes.

180°. Applying the transfer function then allows for a phase delay evolving around 0° between ΔICP_{NIRS} and ΔICP_{ip} shown in black.

3.1.3 Discussion

We developed an approach to estimate changes in ICP non-invasively using hemodynamic changes as measured with NIRS. Using a non-human primate model to induce ICP changes by means of fluid insertion, we showed that the magnitude and time lag of ICP_{NIRS} changes can be reconstructed based on a transfer function approach and thus accurately estimate ICP_{ip} changes detected by a conventional invasive probe.

During induced ICP oscillation, we observed that ΔHb and ΔHbO are out of phase (close to 180°) with each other, which is consistent with blood flow and blood volume changes [180]. The ICP changes induced in this study are expected to elicit a global effect across the brain. The change in ICP leads to a subsequent change in CPP under the assumption that ABP is uncorrelated. Confirmation of the assumed lack of ABP correlation is expressed in Figure 3.8, in which the SNR of the induced frequencies is close to 1 for ABP. If CPP decreases as a result of an ICP increase, it is thus expected that brain oxygenation and ΔHbO decrease. Taken together, our data therefore suggests that blood flow plays a role in ICP induced changes. Our work is consistent with a previous study demonstrating the capacity of NIRS to capture fluid injections into the brain related to ICP [207], yet we expended on this observation extensively in performing the frequency dependent analysis that resulted in the transfer function demonstrated here.

One of the novel aspects to this study is that we induced changes in ICP rather than ABP. The upper image in Figure 3.8 shows average SNR of presumably auto-regulated measurements, while

the lower image shows a highly elevated ICP baseline, at which auto-regulation can be assumed to be impaired. Autoregulation is typically quantified under the assumption that ABP changes are the cause of ICP changes. Very sparse information can be found about changes in ICP without ABP changes that influence the autoregulatory capability of the brain or cerebral blood flow directly. Our initial analysis showed hemoglobin concentration changes in the absence of significant reaction in ABP for oscillations in ICP with periods of up to 2 minutes. Our blood pressure measurements were obtained from the carotid artery, a systemic location external to the brain, due to the inability to access cerebral, local ABP. Autoregulation derived from carotid blood pressure alone might therefore lead to false conclusions about autoregulation impairment since hemoglobin concentrations significantly oscillate with ICP. This limitation underscores the need for the extrapolation to CPP, which will be possible by measuring ΔICP_{NIRS} using NIRS and the algorithm described here in conjunction with arterial blood pressure measurements.

While oscillations in ICP do not lead to ABP oscillations, we observed that long-term baseline changes in ICP do lead to transient increases in ABP baseline. This is seen as a systemic regulatory effect wherein the body alters ABP to ensure sufficient perfusion to the brain. Theoretically, the increase in ABP should stabilize CPP, which in turn ensures a steady cerebral blood flow. Whether this effect is due to the much higher amplitude of the ICP baseline compared to oscillation amplitudes, or to the extended period of ICP elevation, or to the long-term anesthesia remains unknown. We hypothesize that a long duration of ICP elevation triggers an ABP increase while short duration oscillations induced in ICP do not trigger an ABP response, as observed in the time traces and SNR plots above (Figure 3.6, Figure 3.8, Figure 3.10A).

The following assumptions need to be valid for using the transfer function to estimate ICP: a)

A reaction in cerebral hemodynamics to ICP changes must occur, b) other influences on the signal, such as blood pressure elevation or hemorrhage, are excluded, and c) a linear relationship between the pressure changes and the hemodynamic changes exists. The three conditions are addressed as follows:

1. We have shown that ΔHbO and ΔHb react to induced ICP changes. The magnitudes were dependent on the ICP baseline, making low-pressure cases less reliable for ICP_{NIRS} estimation. Nonetheless, we found a reaction to pressure changes even at the very low baseline level.
2. During the experiment, no leakage of cerebrospinal fluid (CSF) or blood was observed. Furthermore, the blood pressure increase as a reaction to ICP changes was observed only during long-term baseline changes and not during short periods of induced sinusoidal changes. However, the effects of anesthesia through isoflurane are uncertain. Future work with an anesthetic known to have fewer potential effects on cerebral autoregulation and hemodynamics will help to clarify this concern.
3. Given the small magnitude of changes in ICP_{ip} and ΔHbO , we assume local linearity. The linearity of cerebral autoregulation and the hemodynamic response are discussed in the literature, and examples can be found for non-linear methods to quantify autoregulation impairment [157, 208], with an overview of non-linear models given by Payne et al.[4]. However, linear models are more common and the high correlation between ΔHbO and ICP_{ip} shown in Figure 3.7 encourages this assumption.

According to Lassen's curve [73] the lower limit of autoregulation can be reached and exceeded if ICP increases, resulting in a decrease of CPP. This implies that the highest ICP baselines we

induced may fall outside the autoregulated range. The reason for autoregulatory impairment can be twofold. On one hand, high ICP can exceed the vasodilation limit of arterioles. On the other hand, fast inflow of saline through the catheter could exceed the fluid uptake rate of the brain. In either case, autoregulation would influence the capabilities of using simple, linear methods like transfer functions to estimate ICP from hemoglobin concentrations. Despite the autoregulatory behavior, we see large oscillations in ΔHbO . Application of the transfer function shows suitable, yet noisier oscillations compared to the invasive measurements. Additional methods to determine the cerebral autoregulation impairment of individual subjects might further improve ICP_{NIRS} estimation. Active autoregulation could be the cause for the trend toward underestimation of magnitudes seen in Figure 3.10C. Furthermore, the transfer function approach can be extended to include ABP and cerebral blood flow measurements. As maintaining blood flow is the goal of cerebral autoregulation, it has great potential to improve the prediction quality. Blood flow measurements could be added by Diffuse Correlation Spectroscopy (DCS) or transcranial Doppler ultrasound. DCS is also a non-invasive method which measures microvascular blood flow and is based on near-infrared light [184].

We demonstrated the feasibility of estimating time traces of ICP changes based on ΔHbO . However, we were only able to report relative changes. In order to quantify the ICP baseline, additional information is needed. With estimation of the ICP offset, the transfer function approach could be used to generate trends over time. Further quantitative ICP estimation of baseline values may be possible based on more sophisticated machine learning tools.

3.1.4 Conclusion

Non-invasive methods to estimate ICP are needed to improve treatment of TBI, hydrocephalus, stroke, and other diseases. Here, we introduced a method that allows for non-invasive, real time measurements of ICP. We have demonstrated that induced fluid pressure oscillations in CSF influence cerebral hemodynamics, which we have measured with NIRS. Fitting a transfer function to the measured changes yielded a mathematical tool to track ICP changes by changes in HbO over long periods of time. We have presented that a reliable fit is possible for both magnitude and phase alignment compared with an invasive reference measurement. While our transfer function approach makes substantial progress toward accurate non-invasive measurements of ICP through NIRS, further refinements of the experimental setup and the data analysis will be necessary to improve its applicability across physiological and experimental conditions. Important next steps include the estimation of ICP baseline through non-invasive measurements and the translation to human from nonhuman primates. Once this approach is more refined, the use of NIRS has high potential for clinical translation as a long-term bed-side instrument to observe trends in ICP as well as a short-term instrument to observe ICP reactions and recovery. Due to its non-invasive nature, NIRS-based ICP_{NIRS} monitoring may be equally useful for low-risk patients that do not qualify for invasive measurements as well as in research settings on healthy subjects.

3.2 Quantification of Intracranial Pressure Baseline

Previously, hemodynamic changes measured non-invasively with diffuse optical devices have been correlated to ICP or CPP [207] and first attempts to predict ICP from these measurements

of hemoglobin concentrations and CBF have been presented (see Chapter 3.1). Using diffuse optical devices such as near-infrared spectroscopy (NIRS) [209, 210] and diffuse correlation spectroscopy (DCS) [184] has the benefit of simplicity of use, given that only one probe needs to be placed on the head that can measure for hours without causing discomfort or risk to the patient. Furthermore, these devices can be portable and potentially low cost. Another significant advantage of diffuse optical methods, such as DCS, which measures changes in cerebral blood flow, is the sensitivity to the microvasculature, allowing for localized measurements as compared to global measurements using TCD.

Here we expand the idea of using hemodynamic changes to measure ICP and demonstrate that absolute values of ICP extraction are possible. We take advantage of changes in the cardiac pulse waveform with ICP as well as hemodynamics. Specifically, we utilize ICP pulse shape changes when the ICP baseline increases [211, 212]. A similar idea has recently been proposed by Fischer and colleagues, who demonstrated a proof-of-concept of estimating ICP in infants and adults based on pulsatile CBF measurements and a recurrent neural network using a hold-out validation [72]. The pulse typically shows three distinct peaks, namely the percussion peak translated from the systolic pulse in the pulsatile arterial blood pressure (ABP), the tidal peak created as a rebound of the percussion peak (a result of intracranial compliance), and the diastolic peak from the closure of the aortic valve (see Figure 3.11c). As ICP rises, the intracranial compliance changes and so does the ICP waveform, with the tidal wave increasing in height relative to the percussion wave. Here we use DCS in a non-human primate model in which ICP was experimentally manipulated to measure the cardiac pulsation of cerebral blood flow, which also shows the three descriptive peaks. Using a set of physically relevant features and advanced

machine learning algorithms, we correlated the morphological changes in the CBF waveform to underlying ICP baselines. This approach permitted a highly accurate estimate of ICP from non-invasive cerebral blood flow sensing [200, 201, 203, 213].

3.2.1 Materials and Methods

To train a machine-learning algorithm to identify level of ICP from cardiac pulse waveforms, cerebral blood flow changes were recorded with DCS in combination with an electrocardiogram (EKG) in five non-human primates (NHP) under different ICP values.

3.2.1.1 Diffuse Correlation Spectroscopy

Diffuse Correlation Spectroscopy (DCS) was used to measure cerebral blood flow. The working principle of DCS has been described previously (see Chapter 2.4). A single long-coherence length laser at $\lambda = 850$ nm wavelength (DL852-050-SO, CrystaLaser, Reno, NV, USA) was used for illumination through a 200 μm -diameter multimode fiber. The source-detector distance was 2 cm and photon counts were recorded at 2 MHz through four few-mode fibers (5.8 μm core diameter) leading into a four-channel photon counting module (SPCM-AQ4C, Excelitas Technologies, Vaudreuil-Dorion, Quebec, Canada). Using software correlation, the photon intensity was auto-correlated and all four channels were averaged. The intensity auto-correlation was then converted to electric-field auto-correlation and fitted to the solution of the diffusion equation [186]. Using this technique, we achieved a sampling rate of 50 Hz, which was fast enough to resolve the cardiac pulsation. CBF was extracted as an expression of the Brownian motion diffusion coefficient αD_B (in cm^2/s) and here described as a percentage change from the baseline, as

Δ CBF. A synchronization pulse was sent to the auxiliary port of the DCS at any time the 3-lead EKG registered a QRS complex in the signal. The EKG used was an in-house amplifier circuit that allowed the detection of a cardiac pulse when the electrical signal of the EKG exceeded a threshold manually set for each subject at the beginning of the experiment. This threshold was set to be exceeded during the R-peak in the QRS complex of the EKG. The thresholding approach of the EKG signal allowed for precise recording of the onset times of a cardiac pulse.

3.2.1.2 Experimental Design

All procedures were approved by the Institutional Animal Care and Use Committee of the University of Pittsburgh and complied with guidelines set forth in the National Institute of Health's Guide for the Care and Use of Laboratory Animals (2011). The measurements were conducted on five NHPs (*Macaca mulatta*, N = 5, f/m: 0/5, 8.2 ± 1.5 years, 10.2 ± 2 kg). All animals were initially sedated using 20 mg/kg of Ketamine independently or in combination with 1 mg/kg Diazepam and 0.04 mg/kg Atropine. After placing an arterial line in the external carotid artery, the animals were ventilated and maintained under anesthesia using a combination of 10-25 μ g/kg/hr Fentanyl administered intravenously and a minimal amount of Isoflurane gas (< 1%). At the same time 0.1 mg/kg/hr of Vecuronium Bromide paralytic was given. Each animal was held with its head facing forward in a stereotaxic apparatus and its stomach on the table. The source and detector fibers of the DCS system were placed directly on the exposed skull of the animals to reduce the influence of skin and muscle layers of the tissue. The fibers were placed laterally on the right hemisphere near anterior-posterior zero in stereotaxic coordinates (Figure 3.11a). For ICP monitoring and pressure manipulation, two small craniotomies were made. One permit-

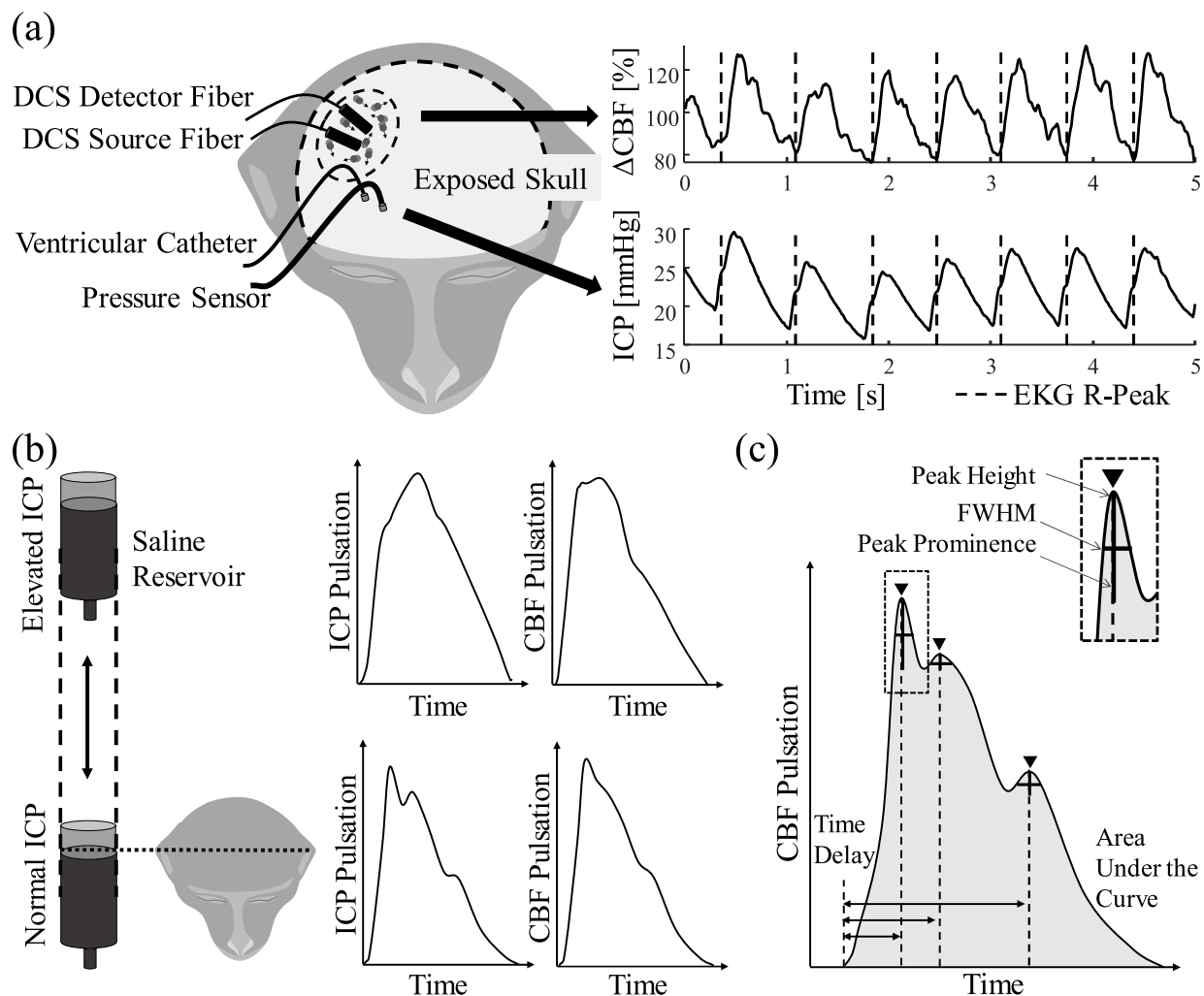


Figure 3.11: Experimental setup and data analysis. (a) shows the experimental setup with the placement of optical fibers and pressure sensor as well as the catheter on the exposed skull of the monkey. The traces at the right show an example of changes in cerebral blood flow (ΔCBF) and ICP. The dashed line marks the maximum of the QRS complex in the EKG recording. (b) shows how the saline reservoir connected to the lateral ventricle influences ICP. The left two pulses show ICP pulsation shape changes, the right two curves show similar changes in blood flow pulsation. (c) shows which morphologically relevant features were extracted from the cartoon version of an ideal ΔCBF pulse.

ted access to the lateral ventricle for a catheter (Lumbar catheter, Medtronic, Minneapolis MN) and the other led into the brain parenchyma for placement of the ICP sensor (Precision Pressure Catheter, Raumedic Helmbrechts, Germany). ABP was measured from the A-line and ICP from the invasive sensor at 100 Hz by a MPR1 Datalogger (Raumedic Helmbrechts, Germany). Alignment markers were sent from a central voltage source to the pressure MPR1 Datalogger and the DCS. The ventricular catheter was connected to an open saline reservoir that was lifted relative to the animal's head height to induce fluid pressure changes (Figure 3.11b). By maintaining a constant height, the pressure of the saline column translated to the cerebral ventricle and ICP was altered. Due to CSF absorption in the brain, the catheter was held open to allow for constant saline flow, which permitted maintenance of an ICP baseline level. The first measurement for every subject was performed at the opening ICP. The ICP was then leveled to 9 mmHg for a second measurement, if the initial ICP was at or below this level. From there, the ICP was gradually raised to approximately 12 mmHg, 15 mmHg, 20 mmHg, and 30 mmHg. In three of the five subjects, the ICP was returned to a level of 9 mmHg between elevated levels (12-30 mmHg), to distinguish ICP-induced influences on the hemodynamic signal from those associated with the passage of time during the experiment. Every ICP level was held for approximately 90 minutes while ICP and Δ CBF were recorded throughout this time period.

3.2.1.3 Signal Processing

General signal processing was performed using Matlab R2019a (The MathWorks Inc., Natick, MA, USA). All recorded signals were aligned with digital markers sent to the DCS and MPR1 Datalogger. EKG markers were used to measure the pulse onsets. Over the course of several

hours, laser instabilities were observed as seen in fluctuating y-axis intersection of the intensity auto-correlation curve, known as β . The presence of a laser instability was determined by any β value, averaged over 10 seconds, that showed a deviation greater than 0.01 from the median. If an instability was detected in a measurement, we removed all points in time where β deviated more than half a standard deviation from the median. Unrelated to β , some DCS pulses did not follow the canonical cardiac waveform shape, likely due to motion artifacts. These motion artifacts can be caused by human intervention for periodically filling the saline reservoir, watering the eyes of the NHP that were held open for visual stimulation of the brain in a parallel experiment, or maintenance of the anesthesia and paralytic solution syringe pumps. To exclude such pulses, we used a z-score rejection. The z-scored Δ CBF over all pulses within a measurement (a period of approximately similar ICP for 90 minutes) was calculated at each time point. Individual pulses that showed a z-score > 3 from the mean of the individual ICP baseline for individual subjects were rejected. After rejection of data, 120 consecutive pulses were averaged to improve the signal-to-noise ratio (SNR). In our NHPs, 120 cardiac pulses corresponded to approximately 60 seconds of data, given a typical heart rate of 120 beats per minute. The invasively measured ICP was averaged over the time of these pulses to function as the ground truth for training of the machine learning approach. The average window was then shifted by 10% of the window length, or 12 pulses, and the procedure was repeated for the entire sequence of ICP data at each ICP level. This approach balanced between the need to average data to reduce measurement noise and preserve a large amount of training data for the machine learning algorithm. The averaged pulses were then normalized to establish a consistent range across animals. The normalization was performed in both the x- and y-direction, i.e. the blood flow change across a pulse was set to

be between 0 (diastolic) and 1 (systolic), and the length of a pulse was set to be 151 data points wide from diastolic to diastolic point in time by means of spline interpolation. This normalization also removed the effect of heart rate changes that can be independent of ICP changes. To improve the SNR further, an adaptive filter was applied to the averaged pulses. Here we used a Kalman filter adaptation, which was applied consecutively to all averaged pulses. Such filtering allowed for the generation of an ideal pulse over time as an average of all previous pulses. Each pulse was compared to the ideal pulse, the difference was calculated, and the pulse was then corrected based on the error. Empirically determined constants defining the trust in the ideal pulse and the measurement determined the strength of correction, weighted by the calculated error. The ideal conception was then updated by adding the new measurement to the ideal conception calculation. As the waveform changed with increasing ICP, so did the Kalman filter. The adaptive filter permitted reduction of the noise while maintaining the cardiac pulse morphology and the ICP based changes thereof. Given the sparsity of recorded pulses above 30 mmHg of ICP, the prediction was only performed for ICP values between 0 and 30 mmHg. The above procedures resulted in a total of 14,121 averaged pulses across all five animals.

3.2.1.4 Feature Extraction

After normalization and filtering, morphological features were extracted. In Figure 3.11b the morphological differences for both ICP and Δ CBF for low (bottom) and high (top) ICP are shown. To describe the subtle differences in the waveforms, the features shown in Figure 3.11c were extracted using the peak finding algorithms provided by the matlab function “findpeaks”. To describe the individual waves within a cardiac pulse, peak height (pk), prominence (p) and

Table 3.2: Morphological features extracted from cardiac pulsation in Δ CBF

Individual peak analysis		Peak to peak differences	Full pulse analysis
$P1_{pk}$	$P3_{pk}$	$d(P1 - P2)_{pk}$	Area under the curve (AUC)
$P1_{pos}$	$P3_{pos}$	$d(P2 - P3)_{pk}$	Mean arterial pressure (MAP)
$P1_w$	$P3_w$	$d(P1 - P2)_{pos}$	
$P1_p$	$P3_p$	$d(P2 - P3)_{pos}$	
$P2_{pk}$		$d(P1 - P2)_w$	
$P2_{pos}$		$d(P2 - P3)_w$	
$P2_w$		$d(P1 - P2)_p$	
$P2_p$		$d(P2 - P3)_p$	

full width at half maximum (w) were extracted. In addition, the time point of the peak relative to the prior diastolic minimum (pos), as well as the area under the curve were calculated. Further information was gained by calculating the differences between waves. A complete list of all features is shown in Table 3.2. P1, P2 and P3 refer to the percussion, tidal and dicrotic peaks of the pulse wave, respectively. The peak to peak differences were denoted as $d(P1 - P2)$ and $d(P2 - P3)$ and were calculated for all four single peak features. In some cases, a feature was not detectable, e.g. when the percussion and tidal peaks ($P1$ and $P2$) merged to a single peak ($P1$) at high ICP. In that case the dicrotic peak (normally $P3$) became the second detected peak ($P2$) and no $P3$ could be found. In such cases, all undetected features were set to 0, but still used in the machine learning algorithm as the lack of a peak could be a strong indicator of elevated ICP. An additional feature added to the algorithm was the averaged mean arterial pressure (MAP) over the time span of the 120 averaged pulses. This was done to avoid misinterpretation of elevated MAP for elevated ICP. Combining the 22 features created a feature set that could be used to describe the individual averaged pulse. A feature set was calculated for every averaged cardiac pulse, creating a matrix including physiologically relatable information to use for supervised machine learning.

3.2.1.5 Machine Learning

To allow for training and testing of the machine learning approach, the data were first separated into training and testing data sets. The testing set, consisting of randomly sampled 20% of all available feature sets, was held out from the training process (performed on 80% of the data) and used in the final cross-validation. The training set was then used to build a regression forest using the python toolbox scikit-learn [214]. The functionality and working principle of regression forests and random decision forests in general has been explained in detail elsewhere [215, 216]. The regression forest chosen here was a bagged ensemble of 1000 individual decision tree regressors. Each decision in the decision tree was binary and described by a threshold across a single feature chosen to yield the highest information gain. Bagging describes that each individual decision tree in the ensemble was trained on a small subset of the available training data set. This reduces the risk of overfitting to the training set. Therefore, we chose to only include a randomly sampled fraction of one third of the training set in each tree. The number was chosen by empirical evaluation. No restrictions were given on the features available to every node or tree, such that all features could be used at any time. The maximum depth of each tree was set to 15. An increased tree depth can yield better results but risks overfitting. In a decision tree regressor, the tree depth is exponentially proportional to the resolution at which ICP can be estimated – a depth of 1 can distinguish 2 ICP levels, while a depth of 3 can distinguish 8. The parameters of ensemble size and tree depth as well as bagging quantity were chosen empirically to achieve a high precision and minimize overfitting. After training the regression forest with the training data set and the corresponding invasively measured ICP as the ground truth, the testing data set was used. A prediction of non-invasive ICP based on the feature sets of each individual pulse

was generated and the correlation to the invasively measured ICP was determined.

3.2.2 Results

We successfully induced ICP baseline changes in 5 NHPs and recorded pulsatile Δ CBF throughout the experiment for multiple hours to generate a data set large enough for machine learning application.

3.2.2.1 Data Acquisition

For every NHP, data were collected in sets of approximately 90 minutes per ICP baseline, with the total amount of data collected for animals varying between 9.1 and 16.6 hours. At the beginning of every set, the ICP was adjusted. The individual measurement sets were combined in post processing. Changes in ICP translated into both changes in ABP and Δ CBF. This was especially apparent when lowering the ICP from an elevated state back down to 9 mmHg (Figure 3.11a). By measuring ABP, ICP, and Δ CBF at high sampling rates, we were able to observe individual cardiac pulses and their characteristic peaks and valleys (Figure 3.12b).

3.2.2.2 Waveform Extraction

The morphological details in the Δ CBF pulsatile signal needed were apparent by comparing the pulses of low and elevated ICP baselines. Comparing pulses at ICP baseline below 10 mmHg, which is considered normal pressure, with pulses during ICP baselines above 20 mmHg, which is pathologically high, showed subtle but distinct differences (Figure 3.13). Overall, a higher ICP led to a broadening and rightward shift of the cardiac pulse compared to the previous diastolic

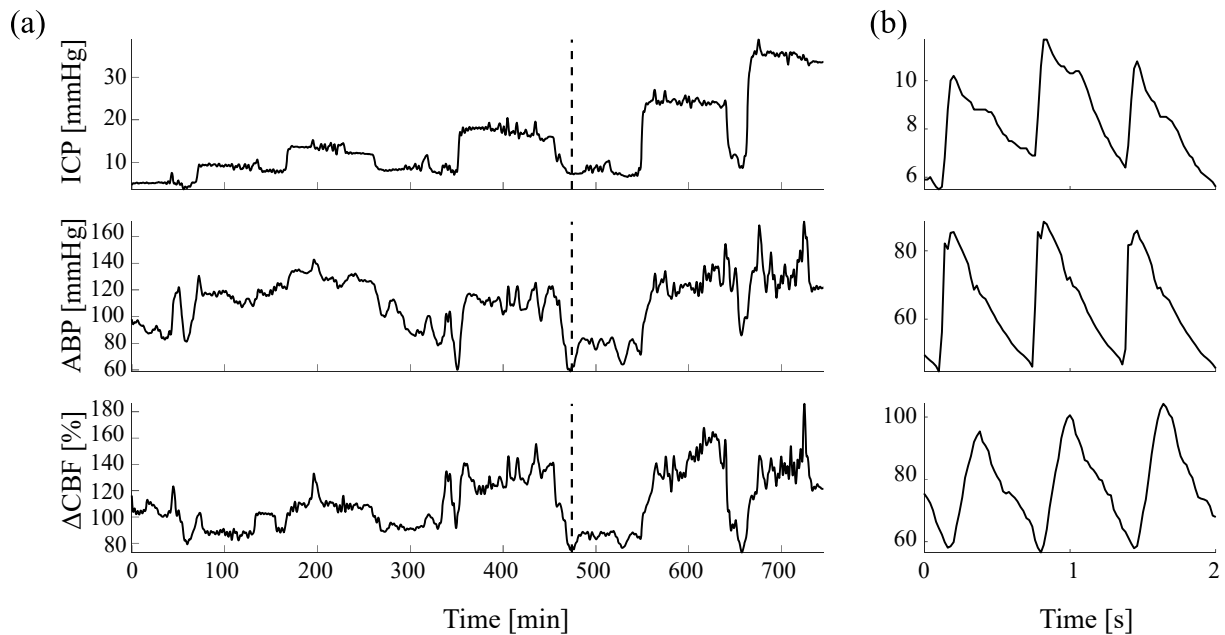


Figure 3.12: Example recording of data in one subject. (a) shows a full measurement from one subject, low-pass filtered (cut off frequency at 0.008 Hz) to emphasize the baseline. Dashed line indicates where figure (b) is located. In (b), a close-up of data at the dashed line is shown to see individual pulses. The pulses were filtered by a moving average of 0.1 seconds.

minimum. The strength of this effect differed between subjects (rows in Figure 3.13, with NHPs 2 and 4 exhibiting the least apparent changes but nonetheless subtle morphological shifts. ICP and ABP waveforms were in good agreement with the non-invasively measured Δ CBF waveform. ICP, measured through a parenchymal pressure transducer, and ABP, measured in the carotid artery through an A-line, must be measured invasively, leaving Δ CBF as the only non-invasive measurement we performed that was able to show these subtle changes.

3.2.2.3 Regression Forest Learner

We were only able to collect a small amount of data in one animal beyond 30 mmHg (Figure 3.14a). Therefore, the training and testing of the regression forest was only performed for data below 30 mmHg. The held-out testing data was closely matched ($r^2 = 0.91$) between the inva-

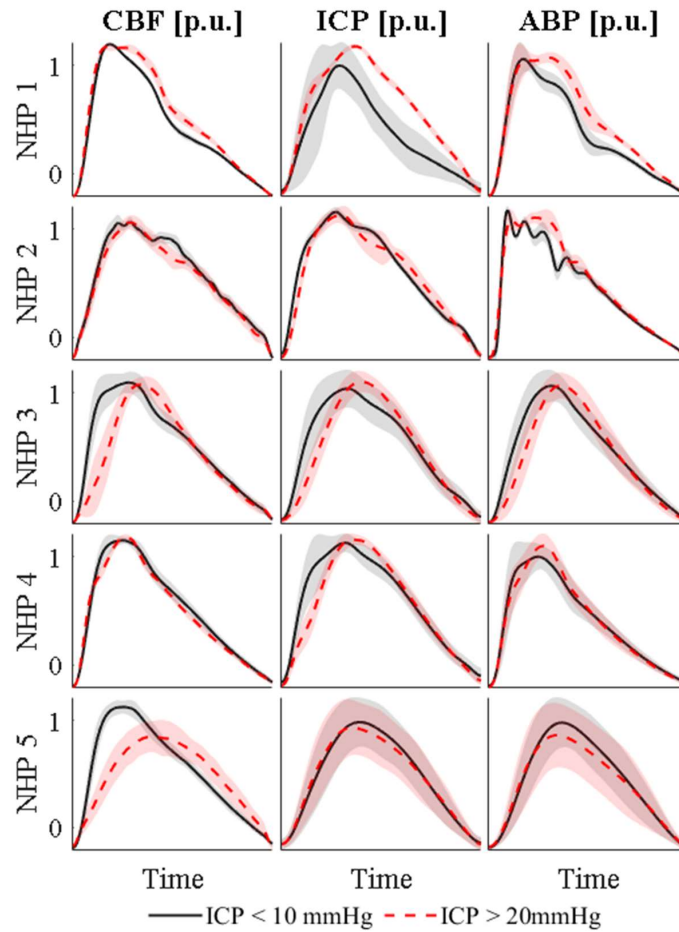


Figure 3.13: Averaged cardiac pulses of all five NHP for Δ CBF, ICP and ABP. The solid black line in each graph shows all pulses below 10mmHg for the specific NHP. The red dashed line shows pulse averages of ICP baselines above 20mmHg. The shaded area shows the standard deviation over all averaged pulses at each time point. The pulses were normalized in height by division of maximum, thus showing a per unit (p.u.) magnitude, and spline interpolated in time to be of the same length.

sively measured (ICP_{inv}) and estimated (ICP_{est}) pressure, as seen in Figure 3.14c. The shaded area shows the confidence interval of the prediction calculated using the Jackknife algorithm described by Wager et al. [217]. The dashed lines show an area of ± 2 mmHg around the ideal match shown as the solid line. A mean squared error of 3.3 mmHg was calculated for this test. A good match between estimated and invasively measured ICP can be seen, especially around 10 mmHg, which is also the area with the most available data (shown in 3.14a). Further evidence for a good fit is given by the Bland-Altman plot that shows how 95% of all data points are within 3.7 mmHg of the invasive reference measurement (Figure 3.14d). We found that the area under the curve (AUC) of the cardiac pulse and the MAP baseline value (not pulsatile shape) were the most important features in our data (Figure 3.14b). This suggests that a measurement of MAP, for instance by blood pressure cuffs or photoplethysmography, is essential for a precise prediction of ICP. In fact, when removing MAP as a feature to the regression forest, to generate a single device approach only using information from DCS, the r^2 value dropped to 0.82 (data not shown). The area under the curve was the second most important feature for predicting ICP, which is confirmed by the wave broadening (Figure 3.13). The time delay to the dicrotic wave, the third peak in the cardiac pulse, was the third strongest indicator of ICP. This feature is interesting as it might not be present in some averaged waveforms. Therefore, the lack of a dicrotic wave can offer valuable information to the fitting algorithm. To simulate a continuous prediction, we ran all available waveforms for a single subject through the predictor and plotted estimates against invasive measurements. Figure 3.14e shows this example measurement, of which randomly selected 80% of the pulses were also used in the training set and only 20% held out from training representing new data points. The graphical representation over time shows good agree-

ment between the estimated (gray colored graph) and the invasive measurement (black colored graph) and the mean square error (MSE) between the two was calculated to be 3.2 mmHg and is thus comparable to the test performed with only held out data (Figure 3.14c).

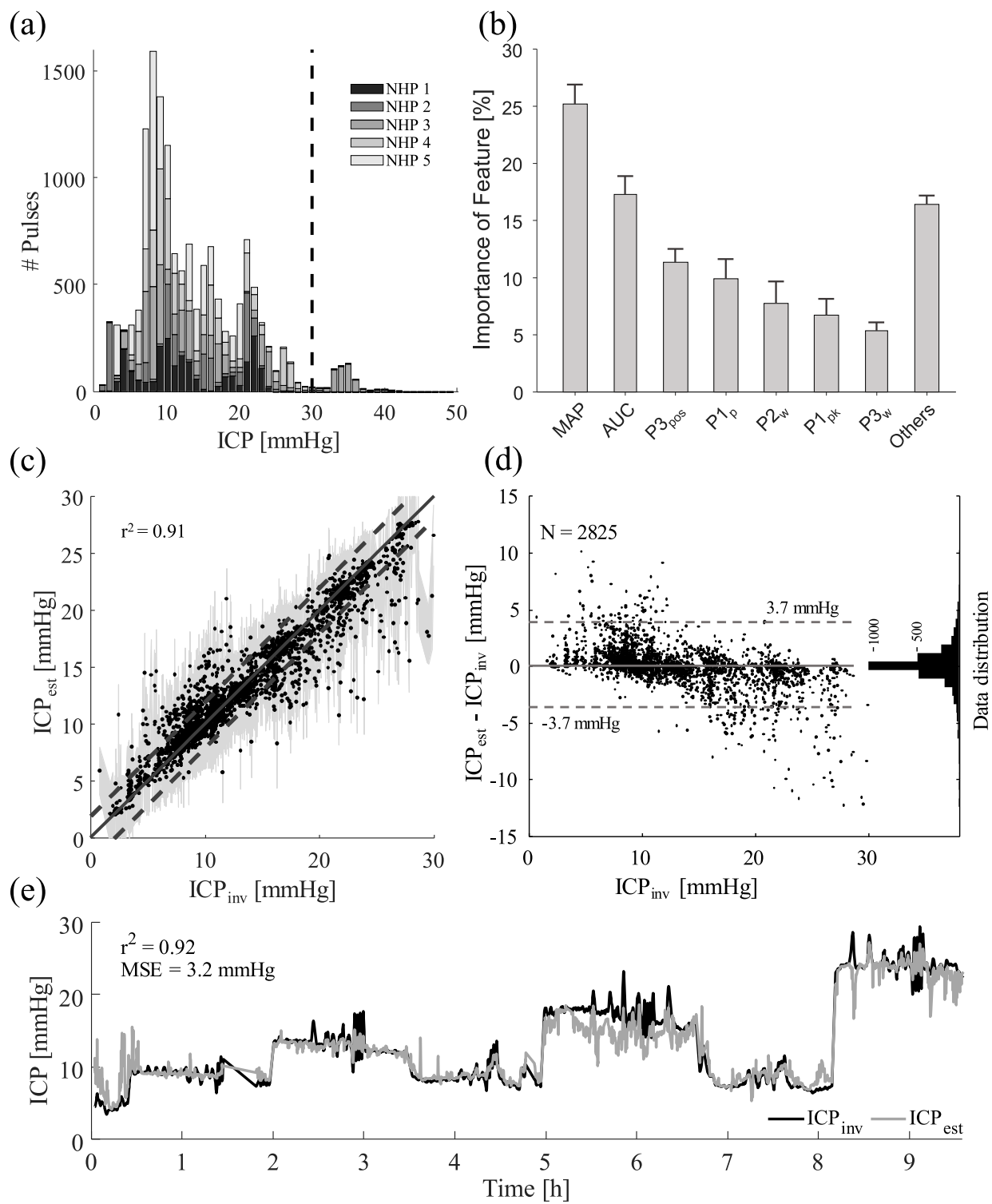


Figure 3.14 (*previous page*): Results of the regression forest machine learning approach. (a) shows the distribution of the available data. The dashed line marks the maximum ICP level that was fitted for at 30 mmHg. (b) shows the distribution of features used in the regression forest as a percentage of all chosen features in all decision criteria generated. The standard deviation across individual trees is shown as error bars. Nomenclature is according to Table 3.2. (c) shows the performance of the regression forest by plotting estimated ICP (ICP_{est}) over invasively measured ground truth (ICP_{inv}). The solid line shows the ideal fit, while the dashed lines mark an area of 2 mmHg around the ideal fit. The shaded area shows the confidence interval. (d) graphs the difference between ICP_{est} and ICP_{inv} over ICP_{inv} in a Bland-Altman plot. The dashed lines span a region of 95% of the distribution, corresponding to a standard deviation of 1.96. The histogram on the right of this graph shows the distribution of data points in number of samples. (e) shows a continuous estimate of ICP for NHP 3. The gray line shows the estimated ICP, and the black line the invasively measured ICP. An $r^2 = 0.92$ and a mean squared error $MSE = 3.2$ mmHg were achieved.

3.2.3 Discussion

In this work, we demonstrate that changes in baseline ICP influence the shape of the cardiac pulsation observed in the ICP and ΔCBF waveforms. This effect allowed us to estimate ICP using a machine learning approach with ΔCBF data obtained from DCS. In our testing in five macaque monkeys in which we induced ICP changes with a catheter placed in the lateral ventricle, we achieved a very high similarity between estimates of ICP and the invasive measurements ($r^2 = 0.91$, cross-validated), with an estimation error of $MSE = 3.3$ mmHg and a 95% similarity to the invasive data within a 3.7 mmHg range. The results therefore indicate the possibility of reliable estimation of ICP in absolute numbers solely based on non-invasive measurements of MAP and ΔCBF . The addition of EKG, another non-invasive measurement, allowed for precise waveform alignment and averaging and is highly recommended in this setup, but not essential if a hypothetical clinical application would not permit its use. The invasively measured ICP was used as a validation reference, but it was not free of measurement error, due to placement location in the brain tissue and inherent device limitations, such that differences between the two

can partially be explained by the limitations of the reference measurement itself. The benefit of a feature-based machine learning approach like the regression forest lies in the information we receive about the importance for every physiological feature, i.e. how often a feature allowed for the most significant split of ICP values. This information can be used to improve the algorithm in the future or reject features to enhance performance for real-time applications. We found that MAP and area under the curve of the Δ CBF waveform were the most important features, while features that can potentially be removed without reducing the prediction performance were the derivative features showing differences in peak height, prominence, full width at half maximum and position between adjacent peaks. Some groups have tried to predict CPP rather than ICP [51, 218]. Under the assumption that $CPP = MAP - ICP$, we would be able to calculate ICP from the estimated CPP through a non-invasive measurement of MAP. We tried fitting to CPP directly by replacing the ground truth of invasively measured ICP with invasively measured CPP and found that CPP prediction yielded $r^2 = 0.98$. While this can be considered a good fit, deriving ICP from here, by subtracting the measured MAP value from the estimated CPP value, showed worse performance, typically overestimating the true ICP with a wider spread of ICP values and yielding $r^2 = 0.76$ (data not shown). This is likely due to the assumptions used to calculate the reference CPP values. Describing CPP as the difference between MAP and ICP is an approximation often used in the clinic, and yet it neglects the effect of vessel wall tension and assumes that venous sinus pressure is always equal to ICP. Furthermore, the MAP feature was used in over 90% of all decisions, which intuitively makes sense given that normal MAP values are approximately one magnitude larger than normal ICP values but overrules the sensitivity to ICP influences on CPP. We therefore chose the direct ICP estimation over the CPP estimation.

Despite the good performance of ICP estimation with our approach, a set of limitations apply:

Generalization and Inter-Subject Variability

1. The ability of the brain to autoregulate blood flow under differing pressure conditions can vary among individuals and is one of many ways the five animals in this study differ from each other.
2. Despite our best efforts at maintaining inter-experimental similarity, some subject variation can be explained by slight variations in the probe placement for DCS as well as the ICP sensor and the ventricular catheter.
3. While our approach outperforms current non-invasive alternatives, estimates of ICP in this study were performed on held out data of the same NHP used for training. Further testing on additional NHPs (not used to train the algorithm) and testing on human subjects is needed to make a direct comparison and draw firm conclusions about the potential of clinical use.

Experimental Setup

1. In our study, changes in ICP were induced with an open saline reservoir connected via a catheter to the lateral ventricle. These changes induced a hydrocephalus-like state in which ICP was altered, but it is unclear how this type of manipulation of ICP will relate to situations involving brain swelling or hemorrhage. Future work will be necessary to test the generality of our ICP prediction in other disease states to make application in traumatic brain injury and stroke possible.

2. The distribution of blood vessels and therefore blood flow as well as intracranial pressure was assumed to be equal throughout the brain. This might limit the application in certain clinical settings like local edema or hemorrhage. However, finding and comparing differences in healthy vs. impaired brain regions can be a strength of this system as well, allowing for localized ICP measurements.
3. Under the assumption that morphological waveform changes are a result of brain impedance changes due to elevated pressure, one must consider that the impedance to flow can be changed by other mechanisms as well, including cerebral autoregulation which influences the vasomotor tone. Influences of autoregulation are not considered artifacts in this study but rather a potential contributor to the signal.
4. Autoregulatory impairment and vasomotor tone can be influenced by anesthesia, which is a limitation of the study design. The isoflurane gas anesthetic, which is suspected to negatively influence autoregulation [138], was kept at a minimum through the inclusion of fentanyl. Nonetheless, the use of anesthesia may influence the generalizability of our results to measurements of ICP in awake individuals or those under different anesthesia regimes.

Signal Processing

1. To train a regression forest, a large data set of features must be generated. This procedure can, depending on the complexity of features and amount of training data, accumulate to many hours of processing time. Once a regression forest is trained however, the application can be done in real-time, given that regression forests perform simple comparisons at each

node in each tree, which require minimal computational power.

2. The accuracy of the regression forest prediction is dependent on the training data set size.

Figure 3.14c shows an increasingly larger confidence interval with increasing ICP, which is an effect of fewer training data points at larger ICP values (as seen in the distribution in Figure 3.14a).

Our work compares favorably to other non-invasive ICP monitors using TCD. Cardim and colleagues reported confidence intervals between 4.2 to 59.6 mmHg when comparing a large number of TCD-based approaches, with an overall confidence interval around 12 mmHg [219]. In the review by Rosenberg et al. a large portion of the discussed ICP monitoring devices used CT or Ultrasound to measure the diameter of the optical nerve sheath [6]. They only make a binary decision between elevated and normal ICP, with a cut-off pressure at 20 mmHg. Reported sensitivity for TCD ranges from 74% to 95%, with a specificity of 74-100% for 7 independent studies identifying ICP > 20 mmHg. CT approaches show similar results as they rely on the same physiological response to elevated ICP. Using our approach, a sensitivity of 88% was achieved, with a specificity of 97%, placing the DCS-based ICP estimation at the top half of the reported classification results, while having the additional advantage of allowing continuous predictions as opposed to binary decisions. This implies that our approach can potentially be used to identify cases of elevated ICP prior to EVD placement, currently estimated by enlarged ventricles in magnetic resonance imaging (MRI) or computer tomography (CT) in TBI patients.

3.2.4 Conclusion

We have demonstrated the potential of DCS to be used as a non-invasive monitor of ICP by interpreting the waveform shape of cardiac pulsation of ΔCBF . The performance of our machine learning approach relied on incorporating non-invasive measurements like EKG, for better pulse averaging, and MAP, for excluding events of elevated MAP. The regression forest reached an $r^2 = 0.92$ (cross-validated) with a mean squared error of 3.3 mmHg. In the future, a transition to human application in clinical settings is needed to test the performance of a DCS-based ICP monitor against clinically relevant invasive monitors in disease states that result in altered ICP for reasons different from the fluid pressure elevation method used here. In addition, increasing the number of subjects will be essential in future work to account for inter-subject variability and improve the generalization of the approach. Nonetheless, our method opens the door for ICP monitors in patients with less severe injuries or diseases as well as healthy patients for research purposes.

3.3 Combination of Intracranial Pressure Fluctuation and Baseline Prediction

The approaches for ICP estimation described in chapters 3.1 and 3.2 show good performance for the estimation of ICP fluctuations and offsets, respectively. The Transfer function approach based on measurements of ΔHbO have a temporal resolution of 5 Hz given the sampling rate of the NIRS device, with a potential to be increased in the future. The major drawback of this approach is the missing offset estimation. Sometimes, knowing that a change in ICP occurred is sufficient,

for example in bedside monitoring in the hospital after shunt surgery. Often enough, the initial diagnosis needs to measure the actual ICP offset. To overcome this shortcoming a machine learning based estimation of ICP was developed, using the pulsatile shape of ΔCBF measured with DCS. A good performance in predicting ICP offsets is shown, but the major drawback of this technique is the temporal resolution and sensitivity to small changes in ICP. Thus, the final product for ICP estimation with both high temporal resolution and sensitivity as well as offset estimation will be the combination of both approaches. A proof of concept (Figure 3.15) shows the potential of this combination. All ICP data for one NHP was combined into one data set. ΔCBF was calculated using the transfer function approach derived from ΔHbO . The quantitative ICP offsets were calculated by averaging cardiac pulsations in ΔCBF , extracting morphological features, and passing the features through the regression forest. The center time point of the averaging period was used to align the estimated baseline ICP_{est} and the estimated $\Delta\text{ICP}_{\text{NIRS}}$. The ICP_{est} signal, being sparse compared to the 5 Hz $\Delta\text{ICP}_{\text{NIRS}}$ signal, was interpolated by repetition of the previous value. The two signals were then added to yield a combined estimate. It is worth mentioning that both devices are non-invasive, bedside compatible instruments operating with near-infrared light. They can be combined into a single, small probe (see Chapter 5) and continuously monitor for many hours. The clinical impact of this device can be high, but research for pressure dynamics and cerebral autoregulation can benefit as well through the availability of healthy volunteer studies. Future work will show the feasibility of the combined instrument in human studies. A first look at clinical translation is presented in Chapter 5.

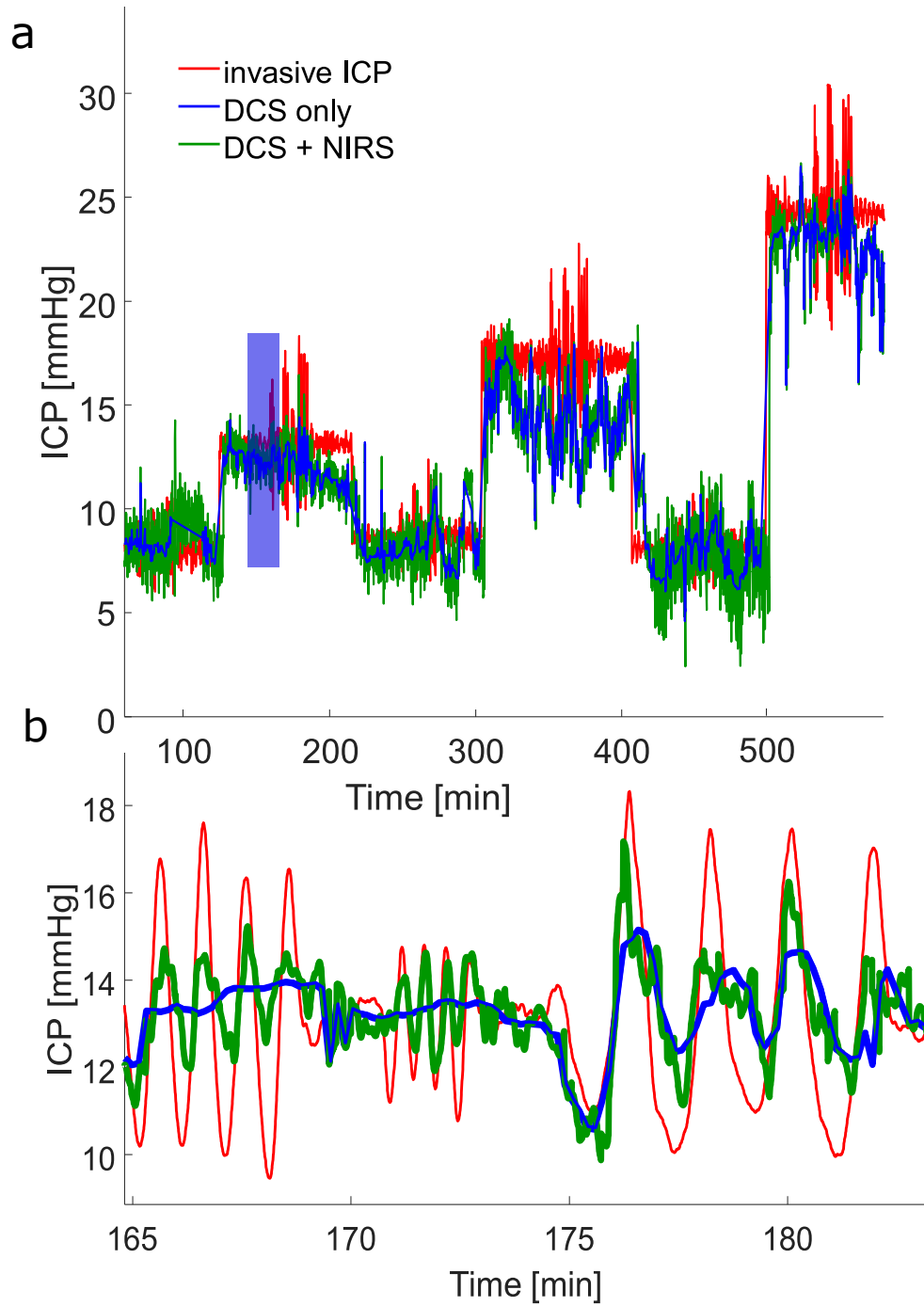


Figure 3.15: Proof of concept for a non-invasive ICP monitor for one example animal. a) shows ICP measurements for a full experiment with multiple ICP offsets and ICP fluctuations at every offset. Invasive ICP (red) is the ground truth and properly followed by offset estimation using Δ CBF pulse data measured with DCS and converted by the trained regression forest into ICP offset estimations (blue). NIRS based ICP fluctuations estimations regain temporal resolution (green). b) shows a magnified section marked with a blue box in a).

Chapter 4

Quantification of Cerebral Autoregulation

Impairment

The measurement of ICP in a non-invasive fashion, as described in the previous chapter, has the potential for a substantial clinical impact. It is not only because of the access to ICP alone, but because it allows for reliable measurements of cerebral autoregulation (CA) as well. The general concept, common measurement methods, and common classification of CA measurement methods have been introduced in Chapter 1.2. Despite many decades of research and a large variety of measurement methods, a consensus on the effectiveness and use of CA measurements to guide clinical treatment has not yet been reached. We believe that common challenges in CA assessment are the comparison to Lassen's curve as a point of reference and the unavailability of ICP measurements in healthy volunteers due to the highly invasive acquisition. These challenges necessitate clinical studies to rely on data from patients with severe injuries and diseases that might affect the autoregulatory system in unpredictable ways and make comparisons across

institutions with varying guidelines for treatment challenging. We set out to overcome these challenges of current CA studies and to create a basis for CA assessments by showing the effects of ABP and ICP perturbations in healthy non-human primates (NHP) with controlled CA impairment by means of isoflurane anesthesia. Inhaled and intravenous anesthetic effects on cerebral physiology can differ strongly, which can be translated to their effect on vasodilation and cardiac output modulations in a dose related manner, as well as cerebral metabolic rates [135], as discussed in Chapter 1.2.2.5. Isoflurane and fentanyl anesthetics are ideal candidates to compare effects of CA and the effects of regulatory vasodilation on CBF maintenance. With this work, we will show how anesthetics can be used to manipulate CA in non-human primates and how this generates a healthy subject basis for CA studies. We will show the agreement of measurement methods of Lassen's curve [73] (Chapter 1.2.3.1), Fraser's phase delays [150] (Chapter 1.2.3.2), and Czosnyka's pressure reactivity index [159] (Chapter 1.2.3.3), under conditions of ABP and ICP oscillations, and we will show the importance of CPP measurements as compared to ABP measurements alone.

4.1 Materials and Methods

We compared measurements of autoregulation in a NHP model during intact and impaired autoregulation, induced both by elevated ICP and change of anesthesia between isoflurane and fentanyl. Isoflurane is used to impair CA due to its vasodilation and blood pressure reduction effects (see Chapter 1.2.2.5), while fentanyl is not known to have significant effects on the vaso-motor tone and maintains CA.

4.1.1 Diffuse Correlation Spectroscopy

In order to measure CBF we used a custom-built diffuse correlation spectroscopy (DCS) system. Details about the specifics and DCS operation can be found in Chapter 2.4. Optical fibers were placed on the exposed skull, one fiber delivering long-coherence length laser light (785 nm or 850 nm wavelength). The returning light was captured by 4 bundled single-mode or few-mode detector fibers 2 cm away from the source light. Software correlation was used to measure temporal changes in speckle patterns in the perfused brain tissue. The fit to the theoretical solution to the diffusion equation yielded the diffusion coefficient term αD_B , which we here refer to as CBF and the relative change is named $\Delta\text{CBF} = \text{CBF} - \text{CBF}_0$.

4.1.2 Experimental Setup

All procedures were approved by the Institutional Animal Care and Use Committee of the University of Pittsburgh and complied with guidelines set forth in the National Institute of Health's Guide for the Care and Use of Laboratory Animals (2011). The facilities at the University of Pittsburgh are accredited by the Association for Assessment and Accreditation of Laboratory Animal Care International (AAALAC) and in compliance with the Standards for Humane Care and Use of Laboratory Animals of the Office of Laboratory Animal Welfare (OLAW D16-00118). Furthermore, this manuscript is in compliance with the Animal Research: Reporting In Vivo Experiments (ARRIVE) guidelines. Measurements were taken on a group of 12 NHPs (Macaca mulatta, f/m: 0/12, 8.1 ± 1.7 years, 9.9 ± 2.5 kg). The cohort of animals used in this study is partially overlapping with NHP used for research in Chapter 3. Therefore, protocols of animal preparation and anesthesia were identical. For this study, 7 animal were anesthetized with

1-3% of isoflurane, while 5 animals received a combination of intravenously administered 10-25 $\mu\text{g}/\text{kg}/\text{hr}$ of fentanyl and a minimal amount of isoflurane gas ($< 1\%$). Anesthesia levels were adjusted throughout the experiment to ensure sufficient anesthetic depth as indicated by either a rise in ABP for isoflurane anesthesia, or a spike in heart rate after a toe-pinch test in fentanyl anesthetized NHPs. All monitoring devices, including intraparenchymal ICP, invasive ABP, and NIRS, as well as the intraventricular catheter were placed and recorded identical to the setup described in Chapters 3.1 and 3.2 (Figure 4.1a).

4.1.3 Experimental Design

Similar to experiments in Chapter 3, ICP was oscillated at frequencies of 0.025 Hz, 0.059 Hz, 0.017 Hz, 0.033 Hz, and 0.009 Hz using the saline reservoir connected to the ventricular catheter. These frequencies were chosen to be around the autoregulatory cut-off frequency [150, 151]. Similarly to above experiments, the ICP baseline was changes from normal pressure (approximately 3-9 mmHg) to highly elevated pressure (40 mmHg). In addition to ICP, PEEP was oscillated using a programmable ventilator (EMV+, 731 Series, ZOLL Medical Corporation, MA, USA) in 6 non-human primates ($N_{\text{Fentanyl}} = 5$, $N_{\text{Isoflurane}} = 1$) as shown in Figure 4.1c. The PEEP value was set to 6 cmH₂O (8.1 mmHg) and oscillated at the same frequencies as ICP with a magnitude of 4 cmH₂O (5.4 mmHg). ABP oscillations were performed on every ICP baseline after the ICP oscillations in the same order of frequencies.

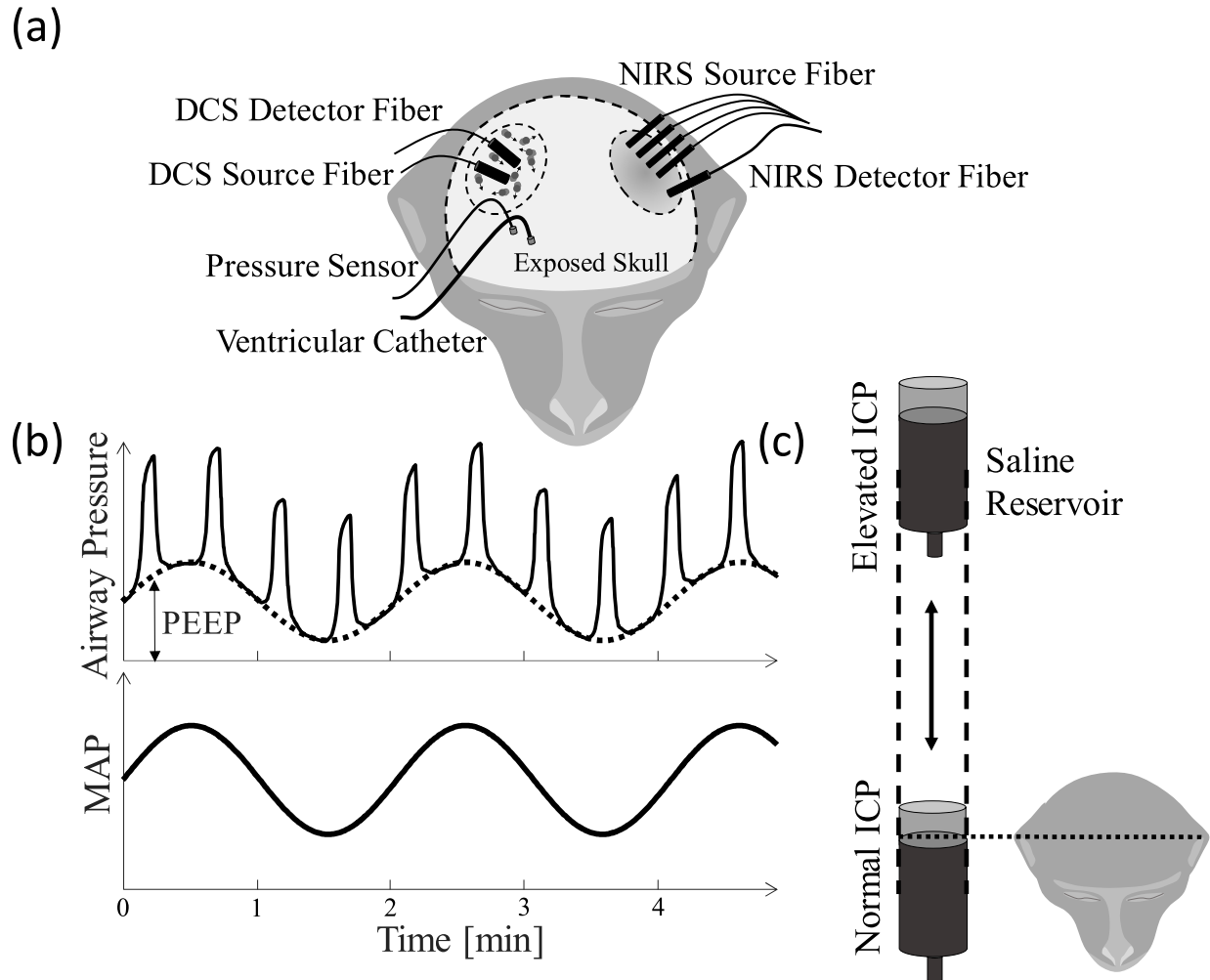


Figure 4.1: Experimental Setup. (a) shows the location of DCS, catheter and ICP sensor relative to the NHP's head. These positions were maintained across all NHPs. (b) The saline reservoir connected to the ventricle catheter was raised and lowered relative to the NHP's head to allow for ICP manipulation. (c) Change in positive end-expiratory pressure (PEEP), the pressure remaining in the lungs after exhalation, through active programming of the ventilator influences systemic mean ABP (MAP).

4.1.4 Signal Processing

To examine the effects of anesthesia and CPP on CA, we assessed it in terms of static CA using Lassen's curve, dynamic CA using phase differences between ICP and ABP, and pseudo-dynamic CA using PRx. For all CA calculations the signals of ABP, ICP and CBF were first aligned based on markers set during the experiment. Mean ABP was calculated using the clinical standard of 2/3 diastolic ABP plus 1/3 systolic ABP. CPP was then calculated as mean ABP - ICP. All signals were down sampled to 5 Hz.

4.1.4.1 Static Autoregulation

Lassen's curve was calculated to see the full range of CPP values and the influence on the regulation of CBF. All data were averaged in bins of 10 seconds to remove effects of respiration and cardiac pulsation. The CBF data was cleaned from artifacts by z-score rejection ($z > 0.5$) on an individual NHP basis, *only* if signs of artifacts were detected. The artifacts in question come from laser instabilities that were not foreseen and were later removed by identification of the β value, which is defined as the intensity auto-correlation at a zero-delay time, subtracted by 1. A measurement was said to have artifacts if at any time point in β value was smaller than the median (approx. 0.1) by 0.01. In stable measurements, the β value is not expected to change significantly from its median given the low-pass filter applied thorough the averaging described above. When laser stability was lost, β started fluctuating significantly and the time point was identified as unstable by its z-score. Afterwards, all CBF data points were cleaned further by rejecting any averaged 10 second window of CBF outside a z-score range of 2, rejecting further artifacts from room light, motion, and remainder of laser instability. Data rejection was done on

a per animal basis. CBF data was then averaged according to the underlying CPP in 180 bins of 1 mmHg width to calculate an average CBF as a function of CPP. For Lassen's curve, CBF curves were mean subtracted and mean divided for each NHP before group averaging of isoflurane and fentanyl anesthesia.

4.1.4.2 Dynamic Autoregulation

Induced oscillations in ABP and ICP were used to calculate the phase difference between ABP and ICP, to allow a frequency domain measurement of dynamic autoregulation. To extract the phase information, narrow bandpass filters were generated using the Parks-McClellan finite impulse response filter generation algorithm in Matlab R2019a ("firpmord" and "firpm", The MathWorks Inc., Natick, MA, USA). This filter generates a pass band of 0.03 Hz to either side of the induced frequencies such that the extracted signal is almost a perfect single frequency sinusoid. The Hilbert transform was applied to this signal, generating an envelope of the sinusoid and containing information of both magnitude and phase of the induced oscillations. Phase information was calculated independently for both ICP and ABP. Subtracting ICP phase from ABP phase yielded phase delay, which has previously been reported by Fraser et al. to be indicative of autoregulation. We performed this calculation independent of the origin of oscillation (fluid induction vs. PEEP) and averaged the phase delays according to their anesthesia protocol.

4.1.4.3 Pseudo-Dynamic Autoregulation

The PRx value was calculated based on the Pearson correlation coefficient of moving averaged ICP and ABP time traces. Signals were down sampled to 0.1 Hz by averaging 10 second periods

of data. The Pearson correlation between down sampled ICP and ABP was calculated over 5-minute-long periods. The same windows were used to calculate an average CPP. PRx values were sorted in 150 groups of CPP values between 0 and 180 mmHg. Before averaging the PRx values, the Fisher's Z transformation was applied to account for cosine shaped Pearson correlations. The normal distributed Z values were then averaged, and the inverse transformation applied. This algorithm was applied to the two groups of different anesthesia protocols separately.

4.2 Results

From a total of 12 NHPs, we recorded CBF, ABP and ICP during varying pressure conditions in ICP and ABP. We collected a total of 45.6 hours of data in 7 isoflurane-anesthetized NHPs and a total of 60.5 hours in 5 fentanyl-anesthetized (with < 1% isoflurane) NHPs. During these measurements we successfully elevated ICP by fluid induction in the ventricles and were able to observe the reaction in ABP and CBF (Figure 4.2).

4.2.1 Static Autoregulation

Static autoregulation was assessed by Lassen's curve (Figure 4.3). Fentanyl-anesthetized NHPs show a plateau of Δ CBF between 60 mmHg and 100 mmHg, indicating intact CA. Sloped areas below and above the plateau, called lower (LLA) and upper (ULA) limit of autoregulation, showing CA impairment. On the other hand, isoflurane showed data dominantly below LLA, indicated by the slope and constantly low CPP in these NHPs. The histograms of CPP values show a wider spread in fentanyl than in isoflurane anesthesia, with overall higher values. The

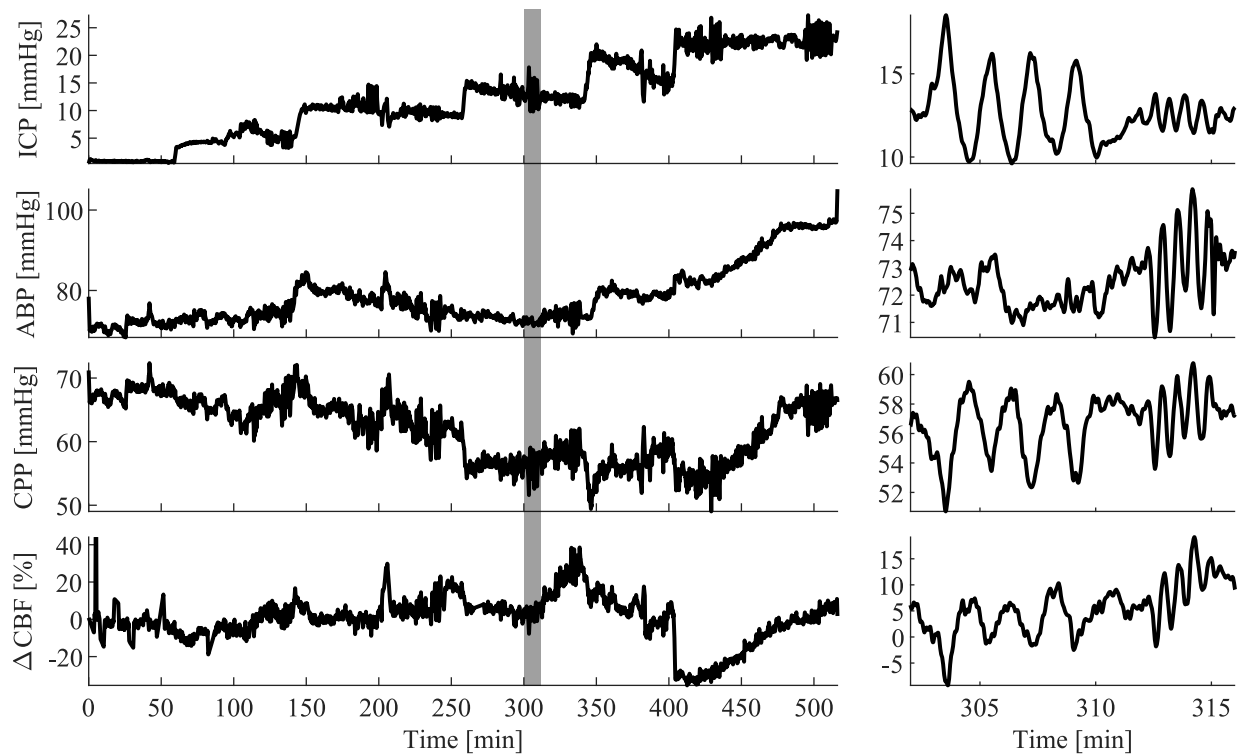


Figure 4.2: A representative measurement of one NHP under fentanyl anesthesia. The left side shows the entire time trace of measurements from this NHP. Clear steps in ICP show on the top graph. ABP follows the ICP baseline trend in the second graph from the top, keeping CPP in the third graph largely stable. Δ CBF changes in the bottom graph show immediate reactions to baseline changes and recovery. The right-hand side shows a zoomed in frame around the minutes 300 to 317 (grey box on the left). Here it can be seen that ICP oscillations (until 310 minutes) as well as ABP oscillations (after 310 minutes) were translated into CPP and Δ CBF.

average CPP value and standard deviation for isoflurane were 48.4 ± 14.7 mmHg as compared to fentanyl with 85 ± 22.5 mmHg. We observed that CPP and ABP distributions were significantly different from each other while ICP values were similar (Figure 4.3). Given that the data were not normal distributed, we performed a Mann-Whitney U-test that evaluated if the two groups came from continuous distributions with different medians ('ranksum', Matlab R2019a, The MathWorks Inc., Natick, MA, USA). While the CPP distributions were significantly different from each other ($p < 0.05$), the histograms of ABP show a larger overlap region ($p < 0.05$). ICP for the same data were found to not be significantly different ($p > 0.05$, see middle Figure 4.3). Isoflurane levels were distinctly different between the isoflurane and fentanyl groups, as they show no overlap (see bottom Figure 4.3). The isoflurane levels reported here are the volume percentages of inhaled air supplied to the ventilator and were documented every 15 minutes. Thus, the histogram is shown as the number of measurements rather than data points, where every measurement corresponds to a baseline level of ICP and incorporates 45 – 90 minutes of data.

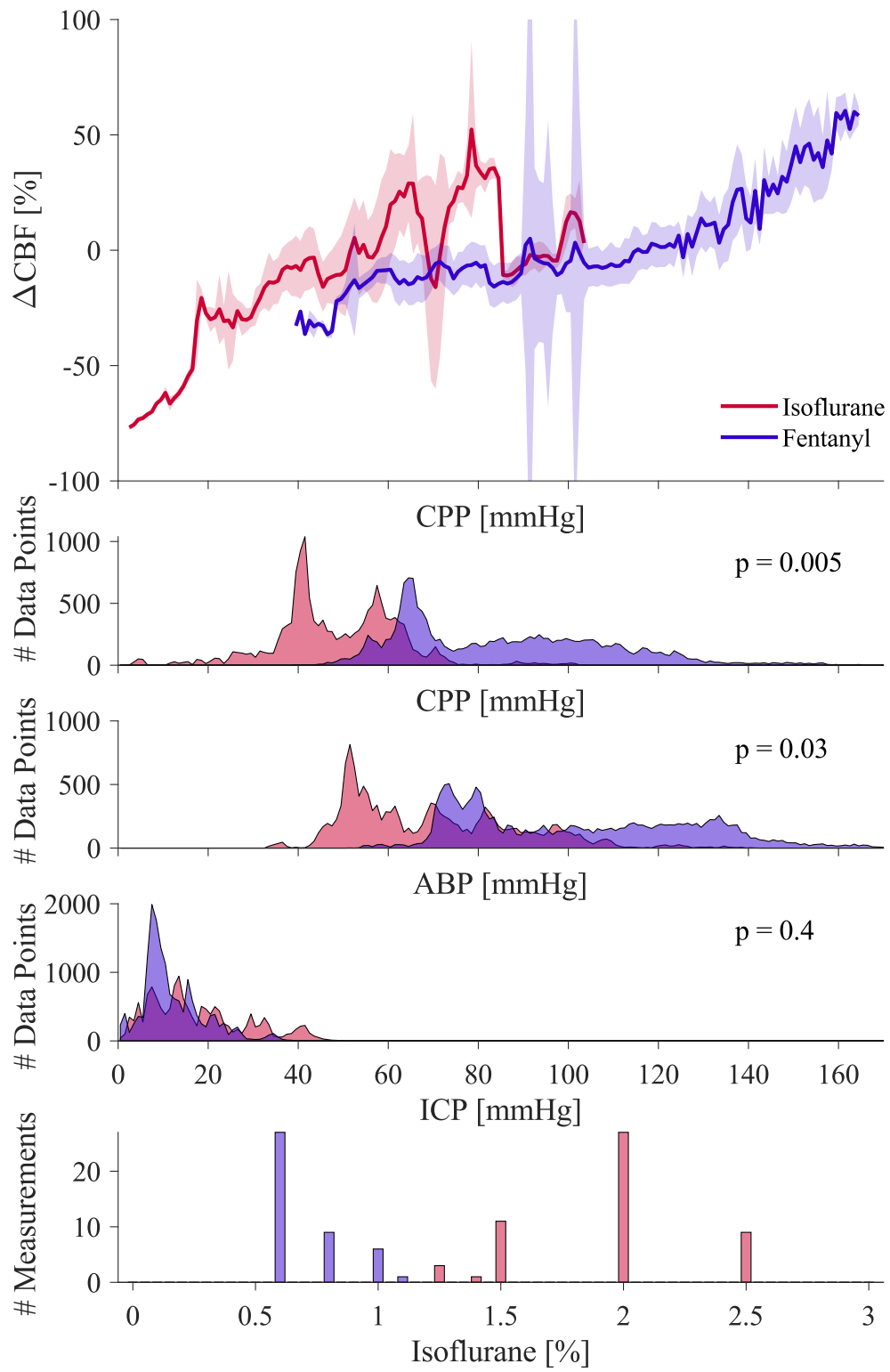


Figure 4.3 (*previous page*): Lassen's curve shows the relationship of ΔCBF over CPP (top). Here the red line indicates isoflurane anesthesia and the blue line represents the group with mainly fentanyl anesthesia. Shaded areas show the standard deviation across all NHPs in this group. The 3 middle graphs show histograms of averaged data point available to create the top graph for (from the top) CPP, ABP, and ICP. A statistical significance test between fentanyl and isoflurane groups was performed (Mann-Whitney U-test) that test the hypothesis that both groups are from distributions with equal medians. Test results are denoted with p-values, where $p < 0.05$ is considered statistically significant. The bottom graph shows the distribution of isoflurane percentage for the anesthetic groups with the number of measurements (of approx. one hour length each).

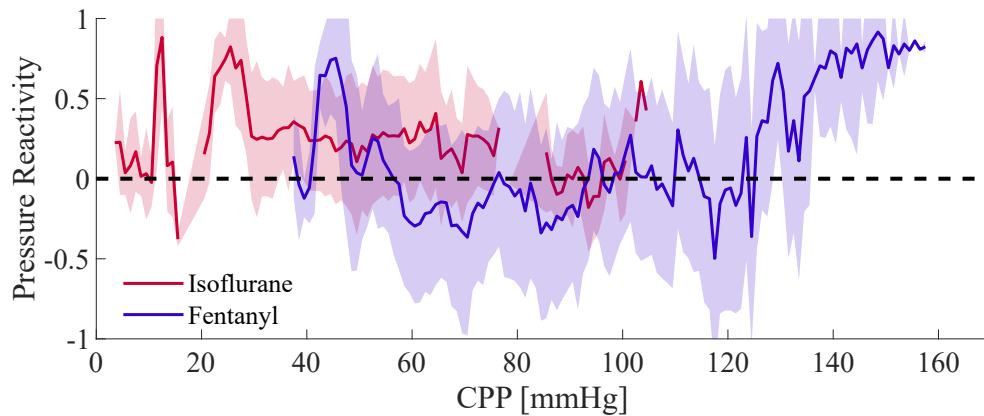


Figure 4.4: Pressure Reactivity (PRx) values are plotted as averages according to underlying CPP values. The red line indicates the averaged response of isoflurane anesthetized NHPs, while blue is the average of fentanyl. Shaded areas show the standard deviation. The dashed line marks a correlation of 0.

4.2.2 Pseudo-Dynamic Autoregulation

Anesthesia dependent differences in the values of PRx were found (see Figure 4.4). The isoflurane-anesthetized NHPs had a PRx averaging well above the zero-line at a broad range of CPPs, indicating CA impairment. Fentanyl-anesthetized NHPs had a largely negative trend within the Lassen's curve plateau of 60 mmHg to 100 mmHg, indicating intact CA.

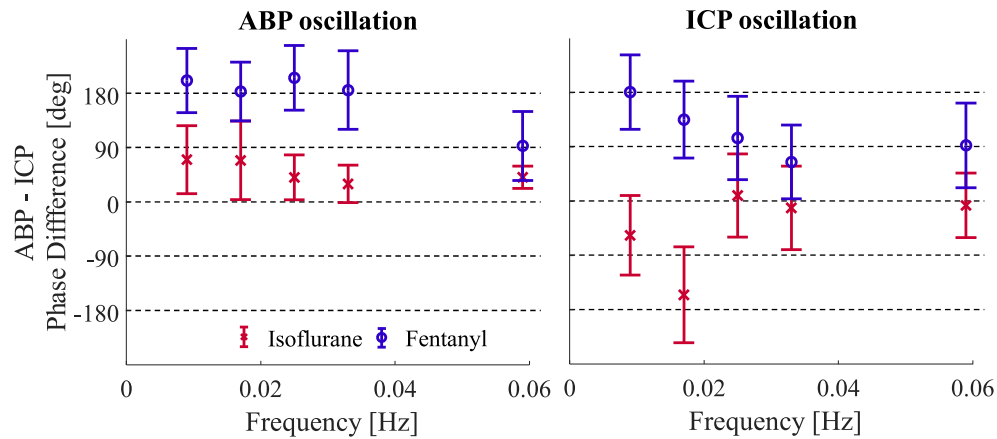


Figure 4.5: The delay lag between ABP and ICP during oscillations in ABP (left) and ICP (right) are shown. Red markers with a central X symbol show isoflurane anesthesia group averages with error bars spanning the standard deviation. Blue markers with a central O symbol show the fentanyl group.

4.2.3 Dynamic Autoregulation

The phase delay between ABP and ICP was calculated during oscillation of ICP (based on fluid induction) and ABP (based on PEEP). ABP oscillations show that fentanyl anesthetized NHPs have a phase lag of approx. 180° (see left side of Figure 4.5), which has also been reported by Fraser et al. [150]. After the cutoff frequency of CA around 0.033Hz [150, 151], the phase difference reduced to 90° . Isoflurane maintained a phase difference below 90° , indicating autoregulatory dysfunction. In addition to ABP, we also oscillated ICP. A decrease in phase difference from the very first frequency of 0.009Hz in the fentanyl group shows a different behavior compared to ABP oscillations. Isoflurane oscillations are mostly below but close to 0° , showing that CA might be compromised.

4.3 Discussion

Our results show that measurements of static, dynamic, and pseudo-dynamic autoregulation under anesthesia induced autoregulation impairment are in general agreement, that CPP is a better comparison value of CA than ABP or ICP alone, and that ABP and ICP oscillations result in different yet comparable frequency responses of pressure reactivity. These findings are further discussed below.

To measure the impairment of CA, the autoregulatory system first needs to be perturbed. Height change in a saline reservoir connected to the lateral ventricle and manipulation of PEEP can be used to activate autoregulatory reactions. We showed that oscillations in ΔCBF occur as a reaction to ICP and ABP oscillations (see Figure 4.2). A change in ΔCBF is acceptable if an appropriate compensation is seen in a timely manner. However, for high ICP elevations that lead to very low CPP, the LLA of the Lassen's curve (Figure 4.3) can be exceeded and CA becomes impaired, meaning that ΔCBF is no longer recovering from CPP changes and the NHP is at a higher risk for oxygen starvation of the brain.

Dividing the field into static, pseudo-dynamic and dynamic CA allowed us to capture a range of CA measurement algorithms proposed in previous years. To control for a presumable ground truth of CA impairment in the NHPs, we have used two different protocols of anesthesia, namely higher percentage of isoflurane gas anesthetics ($> 1.5\%$) for CA impairment and very low isoflurane ($< 1\%$) in combination with predominantly fentanyl anesthesia, administered intravenously, for intact CA.

The ranges of CPP (Figure 4.3) between the two groups are significantly different ($p < 0.05$) and show little overlap. This is likely an effect of the anesthetic itself as isoflurane has been shown to

suppress ABP at higher dosage [136]. The wider range of CPP in the fentanyl group allowed for a full reconstruction of Lassen's curve. The reconstructed Lassen's curve follows the literature based canonical shape and clearly shows the plateau of intact autoregulation where ΔCBF was not changing. The isoflurane group with the reduced CPP had most of the data beyond the LLA, showing a dependency of ΔCBF and CPP and autoregulatory impairment. This observation was confirmed by the PRx value (Figure 4.4), in which low correlation values indicate intact CA. Our results indicate that autoregulation is intact when using fentanyl, with PRx values below 0, while isoflurane impairs autoregulation with values of PRx above 0, often showing PRx $>$ 0.3. This further indicates that the isoflurane group had impaired autoregulation. Furthermore, the phase difference between ABP and ICP during pressure oscillations shows that dynamic autoregulation is impaired in isoflurane measurements for both ICP and ABP oscillations, as indicated by a smaller phase lag, and intact in fentanyl anesthesia, given the almost 180° phase difference. Given that all three CA approaches indicate the same trends, and that they are in accordance with the original publications and the anesthesia comparison in patients undergoing elective surgery given by Tiecks et al. [141], we are confident that CA manipulation was successful.

The results, however, differ from the original publications significantly in that they were performed on healthy NHPs, not hospitalized patients. More importantly, the driving force for CPP changes in this study is a change in ICP, not ABP. These two changes combined give weight to the hypothesis that it is not only ABP that drives CA activity, but more likely CPP. In this case, ICP plays an important role in the regulation of brain perfusion and has strong implications on treatment of patients at risk of elevated ICP, as it happens in traumatic brain injury or hydrocephalus. This hypothesis is further strengthened by the similar reactions to oscillations

at different frequencies in ICP and the frequency dependent response in case of intact CA during fentanyl anesthesia. Yet another indicating factor is the distribution of ICP and ABP values across the two anesthetic groups. While the CPP and ABP histograms show a significant difference, ICP histograms for the same data set show very similar distributions (as determined by Mann-Whitney U test in Figure 4.3). Furthermore, the overlap region of CPP values is smaller than the overlap in ABP. This shows that it is not the individual ABP or ICP value but their combination ($CPP = \text{mean ABP} - \text{ICP}$) that should be considered when measuring CA impairment.

Limitations to this approach apply:

- We presented the data as a group average across animals, which permitted us to pool the data to have the highest power to measure CA. In the future, investigation into individualizable CA measurements is necessary.
- We used stereotaxic coordinate to place our measurement probe and cannula in an equivalent location across all NHPs. However, slight variations are possible. This especially applies to the placement of the pressure probe into the parenchyma as its location was determined through measurement of distances on the skull, and the DCS probe to measure ΔCBF , which was placed relative to the pressure probe and needed to be fitted to the skull's shape.
- The rate of anesthetic administered for both fentanyl and isoflurane varied across NHPs, due to differences in weight and metabolism, and sometimes had to be adjusted during the experiment. Therefore, the degree of CA impairment between NHPs within a group might vary slightly.
- ABP was measured in the carotid artery and assumed to be systemic in this work. The

ABP inside the skull might vary from this assumption. Similarly, ICP was assumed to be global across the cranium. This assumption is not necessarily valid in clinical applications as pressure distributions can potentially vary with lesions, fractions, or tumors.

- While the results above were recorded on healthy NHPs, and similarity to human anatomy and physiology is high, direct comparison to healthy human subject might still show differences in auto-regulatory abilities. Without reliable non-invasive assessment of ICP, this limitation cannot be easily overcome.

4.4 Conclusion

The information presented here shows that isoflurane strongly impairs CA, in both dynamic and static measurement approaches, while fentanyl anesthesia allows for adequate pressure and cerebrovascular flow regulation. The impairment applies to both ICP and ABP perturbations of the vascular system, suggesting that it is the CPP value that sets CA in motion. This is further supported by observations that ABP and ICP distributions can be similar while CPP distributions between fentanyl- and isoflurane- anesthetized NHPs are significantly different. This implies that clinicians might have to regulate CPP in patients with hydrocephalus, stroke and traumatic brain injury, instead of relying on ABP or ICP alone.

Chapter 5

Clinical Translation

The results in Chapters 3 and 4, acquired in non-human primate studies, show the potential of non-invasive ICP and CA sensing using diffuse optical methods. The methods developed in NHPs were translated into the clinic as a next step. For this, a clinical collaboration with the Children's Hospital of UPMC of Pittsburgh was created. Patients in the pediatric intensive care unit were recruited, with an age range of 1 through 17 years. Inclusion criteria were informed consent of their parents or legal guardians, and the availability of ICP measurements through an EVD or a parenchymal pressure sensor. This study was approved by the University of Pittsburgh Institutional Review Board (IRB#: PRO16030693) and the Carnegie Mellon University Institutional Review Board (IRB#: STUDY2018_00000121). To translate the mathematical models developed in NHPs, NIRS and DCS data from pediatric patients during resting and routine EVD shunting was recorded. The transfer function developed for NHPs was applied to the patient data as a proof of concept for non-invasive ICP estimation in humans. In the following chapter I will explain the preparations necessary to translate the feasibility studies in previous chapters into the

clinic, show preliminary results, and give a direction for future work.

5.1 Clinical Setup

A dedicated set of NIRS and DCS devices was arranged on a mobile cart to increase ease of use and mobility in the hospital (see Figure 5.1c), while being able to quickly deploy the instrument and remove it from the patient room in case of emergencies. A large green power switch on the front of the cart allowed medical staff and operators to quickly shut off the power to all lasers and detectors, while data acquisition would continue through battery power until safely stopped by the operator. Recorded data could then be saved onto hard drives from the laptop's battery power alone. For additional safety, appropriate laser hazard signs were made visible and eye protective glasses, filtering red and near-infrared light, were handed out to the patient. Throughout the measurement, regular check-ups on the laser safety, probe position and signal quality were performed approx. every 15 minutes by visual inspection from outside the room.

The probe that was placed on the patient's head was custom designed to incorporate NIRS and DCS fibers as co-localized as possible (Figure 5.1a). The design utilized prisms to reflect light in a 90° angle onto the skin, and the diffuse reflected light back into the detector fibers. This created a smooth surface of the top of the probe, that was used to attach the probe to the patient's forehead using medical adhesive wrap. The angled light guidance increased coupling efficiency to the skin, compared to a straight fiber setup in the non-human primate studies (Chapters 3, 4). It further reduced the ambient light leaking into the fiber tips and reduced the strain on the fibers itself, making it significantly more comfortable to wear for extended periods of time. NIRS and

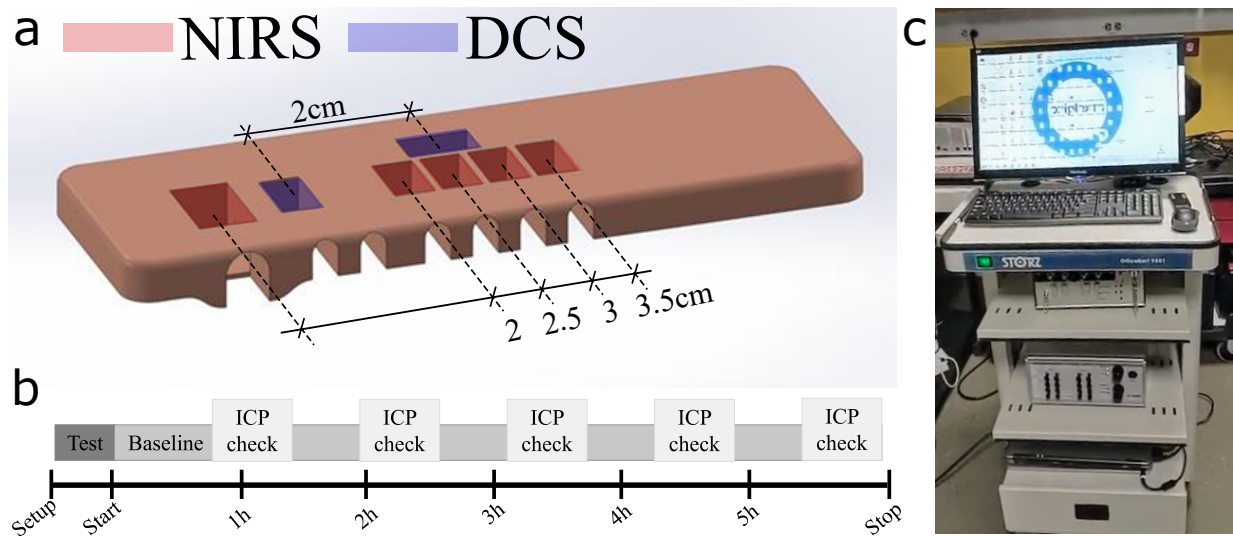


Figure 5.1: The devices used in the clinical setup are shown. a) shows the setup of a custom made probe design that incorporates NIRS and DCS. Light is reflected through a prism onto the skin at a 90° angle. b) shows a schedule for a typical measurement of pediatric care with occasional ICP checks in which ICP is measured through the EVD. In c) a picture of the cart is shown that allows easy and flexible transport of the device to the patient. From top to bottom it shows the user input device table, the DCS shelf, the NIRS shelf, the computer unit shelf, and the drawer for supplies like disinfectant and probe fixtures.

DCS data were aligned by a voltage signal sent to auxiliary channels in both devices simultaneously from a manually activated voltage source. Measurements of ICP, ABP, EKG and other clinically relevant vital signs were recorded by the hospital information system and extracted manually after the measurements for the patient had been concluded.

5.2 Measurement Protocol

After informed consent was received, the device was brought into the patient's room and placed most often behind the bed to allow for maximum accessibility of the patient by medical staff. This also allowed the optical fibers to run to the top of the bed and away from the patient. The

probe was cleaned with disinfecting alcohol wipes and dried before it was placed on the forehead of the patient, approx. 1 cm above the eyebrow and away from the inter-hemispheric fissure, with variations based on the patient's condition. The measurement then followed a general scheme (Figure 5.1b), in which vital signs, Δ CBF as well as HbO and Hb were recorded. Regularly, medical staff perform a measurement of ICP ("ICP check") by closing the EVD and stop the CSF drainage that reduces ICP, measure the fluid pressure inside the ventricular catheter through a pressure transducer installed in the catheter (see Figure 1.4). CSF is predominantly water and as such in-compressible, therefore the fluid pressure in the catheter is equal to the pressure inside the head. The ICP measurement at typically 120Hz sampling rate would last for 1-5 minutes, at which point the system was set back to CSF drainage. After 1 hour of consecutive measurement, the recordings was stopped and restarted to give time for medical routines and patient care. Consecutive hours of recording were possible given that most patients were in the bed or the small perimeter of their rooms due to the EVD and ICP sensor placements.

Measurements of ICP using a parenchymal pressure transducer probe is a second possibility and allows for constant ICP monitoring as opposed to the small true ICP measurement during shunt closure in the EVD. While this measurement method has so far been an exception, patients with both EVD and parenchymal pressure probe are comparably often available in the pediatric intensive care and would yield more reliable data.

At the beginning of every new measurement, a set of markers were sent to DCS and NIRS for alignment to each other and the hospital information system, from which a time was taken and written into the measurement protocol for alignment to an additional time marker.

The study protocol allowed us to measure for multiple consecutive measurements for a total

duration of 7 days. As of today, measurements on 5 patients have been conducted, with an age ranging between 17 month and approximately 12 years, where 2 patients had hydrocephalus, and 3 TBI. A total of approx. 14 hours of data was collected. Due to the early stage of this study, and ongoing improvement iterations on the setup and protocols, only preliminary results can be shown.

For a proof of concept, the estimation of ICP fluctuation based on a fitted non-parametric transfer function to an example data set is presented. Note that this transfer function has been fitted on the basis of non-human primate data and perfect compatibility cannot be guaranteed. For application of the ICP offset estimation and CA, more data collection is required.

5.3 Signal Processing

Before further data transport outside the hospital, data was deidentified by removing all links to the patients name, room number and other personal information. The hospital data was received as an extensible markup language (XML) file, that categorized data in 2 minute bins. A python script was developed to translate the XML structure into a more convenient, matlab compatible ".mat" file. Special care was given to the variety of devices that are dynamically installed and removed from the recording in the clinical daily practice. Therefore, the code was written to dynamically create variables and ensure perfect time alignment.

Based on the time and alignment markers, as well as measurement duration, sections of clinical data were extracted to match the time frames of optical recordings. For EVD based ICP measurements, ICP readings were only possible when the shunt was closed. Hemoglobin concentration

changes were calculated based on the modified Beer-Lambert law (Chapter 2.3.2). Signals of ΔICP , ΔHb , and ΔHbO were calculated by mean subtraction, down sampled to 5 Hz, and low-pass filtered using a 0.1 Hz cut-off frequency as described in 3.1.1.4. The transfer-function derived for non-human primates (Equation 3.1) was applied to ΔHbO .

5.4 Preliminary Results

A general observation for measurements on awake patients is the amount of movement artifacts that renders a large portion of the data unusable. Furthermore, it was observed that patients would occasionally lift and move the probe. This often causes the detectors, faced with high light levels from room light, to perform a security shut-off in the NIRS system.

From the data sets of good and stable hemodynamic signals, visual inspection of correlations between ΔHbO and ΔHb are generally negative, which hints towards good hemodynamic data quality, as compared to positive correlations that might indicate movement artifacts (Figure 5.2). Due to short term measurements of ICP in patients with EVDs, only little data is available in which continuous ICP signals are available. The example in Figure 5.2 shows an ICP measurement in patient 4. This data set was chosen due to the long duration of consecutive shunt closure in the EVD, allowing for a five-minute ICP measurement. As seen previously in NHPs, opposing trends can be observed between ΔICP and ΔHbO . Therefore, the transfer function yields a good approximation, with an explained variance $r^2 = 62\%$ between the invasively measured ICP ($\Delta\text{ICP}_{\text{iv}}$) and the estimated ICP ($\Delta\text{ICP}_{\text{NIRS}}$).

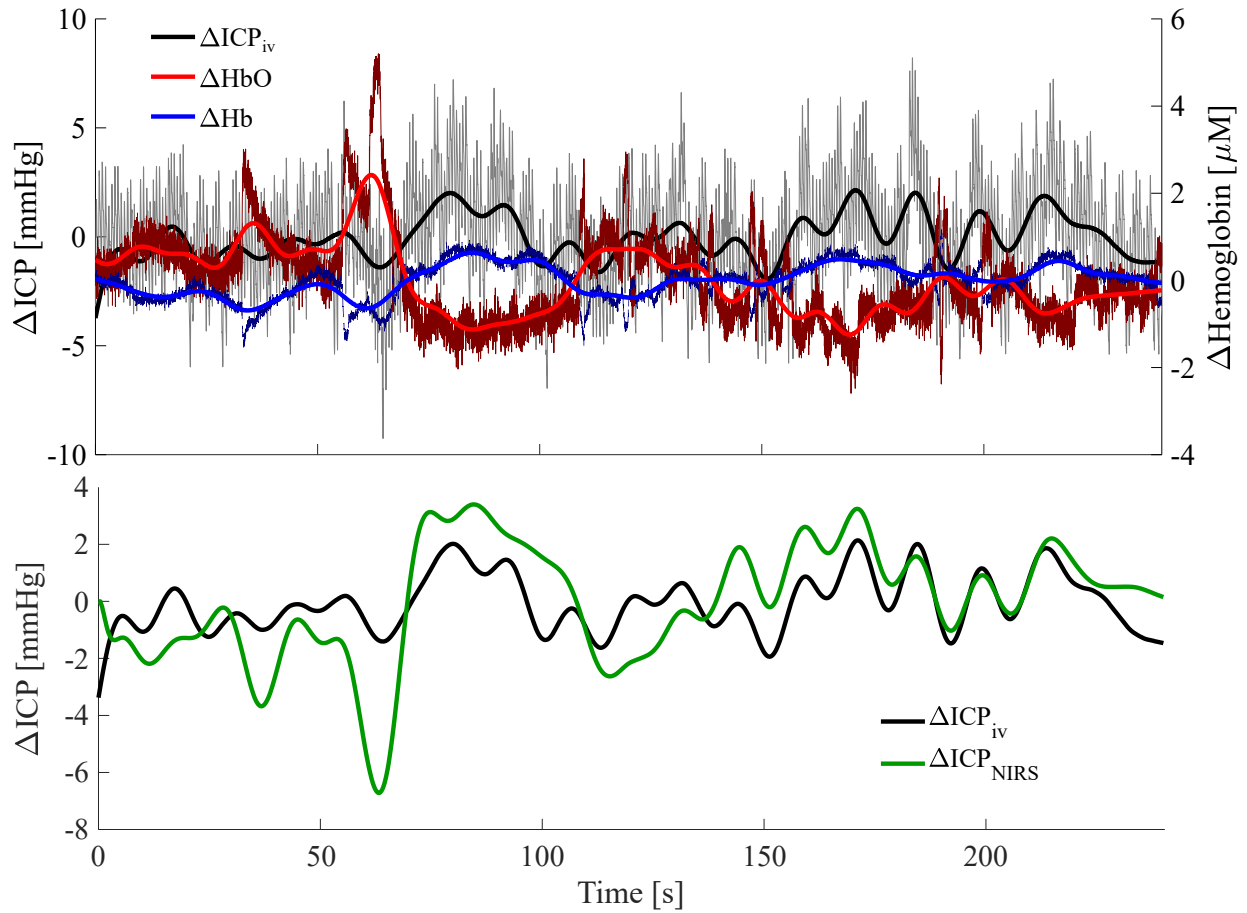


Figure 5.2: A 4 minute example measurement from one patient is shown in the top figure for ΔICP_{iv} (black), ΔHbO (red), ΔHb (blue). The bold line shows the low-pass filtered trends of the high-frequency signal shown in thin lines. The bottom figure shows the same ΔICP_{iv} (black), compared to ΔICP_{NIRS} (green), estimated based on the transfer function derived for non-human primates in Chapter 3.1.

5.5 Discussion

Preliminary results show a proof of concept for the measurement of ICP fluctuations in pediatric TBI and hydrocephalus patients. The similarity to measurements in NHPs is given even though ICP was not actively manipulated as it was in NHPs, which further indicates a strong link between ICP and HbO changes. Therefore, the data shown in the example (Figure 5.2) is surely a good example and yet not all sections in which ICP was measured can show similarly high correlations. Despite the encouraging results, a human based transfer function should be re-fitted, to account for different dynamic influences and further improve performance of the estimation. Potential differences that influence the transfer function fit are vessel wall tension, impedance to flow inside the skull and skull structure, the significance of voluntary breathing compared to the use of ventilators, and the influence of anesthesia.

The measurement of absolute values, or the offset of ICP, requires the measurement CBF and precise averaging of pulses as described in Chapter 3.2.1.3. Therefore, more data with improved SNR and better alignment precision to the hospital information system is needed. How well the NHP based machine-learning approach will perform is unknown, yet it is most likely, that a new regression forest has to be trained to gain results comparable to the ones shown in Chapter 3.2.2. For the future, data acquisition needs to continue and special attention has to be directed towards motion artifact reduction. Furthermore, a solid basis for data alignment needs to be determined. Ideally, a voltage signal can be sent to the bedside monitor or be received from it and recorded in the optical acquisition boards. This will grant access to the clinical EKG measurements. The EKG signal, with its very sharp QRS complex, is the ideal candidate to determine onset times for pulse wave averaging needed to improve SNR and determine ICP offsets.

Chapter 6

Summary

In this work, I have described the mathematical tools and models necessary to use NIRS and DCS for non-invasive ICP estimation. After giving a detailed introduction into the pressure dynamics (Chapter 1.1) and mechanisms of CA (Chapter 1.2), with a special focus on emphasizing the challenges in today's diagnostic approaches and their influence on therapeutic decisions, I laid out the basics for measurements of Δ CBF, HbO and Hb, using non-ionizing, near-infrared light (Chapter 2.3, 2.4).

In Chapter 3.1, I have reported on the mathematical approach to measure fluctuations in ICP by fitting a non-parametric transfer function to translate oscillations in Δ HbO into Δ ICP. In that, I have developed the modelling approach, worked on a design for in-vivo testing and collected data from NHPs under varying conditions of ICP elevation. Good agreement between invasively measured and estimated fluctuations in ICP was shown, with correlations of up to $r^2 = 0.86$ for continuous measurements and an overall correlation of oscillation magnitude heights of $r^2 = 0.84$ and a phase delay close to 0.

To measure offsets in ICP, or in other words absolute values, I reported on the use of shape changes of the cardiac pulsation in ΔCBF , measured with DCS, to be linked to ICP changes in Chapter 3.2. Here, I have collected evidence for the theory of shape changes in cardiac pulsation of ICP and how similar effects of impedance changes in the brain also influence ΔCBF . I developed the computational model using a regression forest training, extracted characteristic features describing the shape of the cardiac pulsation, and tested the approach in-vivo in NHP. For 20% of held out data from the regression forest training, an overall correlation of invasively measured and non-invasive estimation of $r^2 = 0.91$ was achieved, with 95% of all data within an error range of 3.7 mmHg and a comparable ability to distinguish normal from elevated ICP at a 20 mmHg threshold to other proposed non-invasive measurement techniques.

The developed non-invasive ICP measurement techniques can not only be employed to measure ICP for its own sake but also to measure the brain's ability to regulate pressure and blood flow in the brain. In fact, elevated ICP and CA impairment are often seen in the same types of diseases like TBI or ischemic stroke. Unfortunately, there is no universally agreed on measurement technique for CA. I therefore attempted to identify a model of known CA impairment for future work on non-invasive CA measurement techniques. In Chapter 4, I described how changing anesthesia between groups of NHP, in which changes in ICP and ABP were introduced, allowed for shedding some light onto the importance of ICP in CA assessment. This further allowed the comparison of different CA measurement techniques introduced in Chapter 1.2. It was found that static and dynamic autoregulation assessments in NHP under fentanyl anesthesia were intact, while they were impaired in isoflurane gas anesthesia.

Finally, I elaborated on the early stage of clinical translation for this work in the pediatric intensive care unit in the Children's Hospital of UPMC of Pittsburgh in Chapter 5, in which I show first success in translating ΔHbO fluctuations into ΔICP changes with a good correlation of $r^2 = 0.62$. Further data collection and adjustments of the models developed in Chapters 3 and 4 are necessary to conclude a final test of feasibility and evaluate the clinical impact.

Collectively, these studies demonstrate that (1) diffuse optical devices are sensitive to ICP changes, (2) these changes can be translated into physical ICP values by means of signal processing and machine learning, (3) measurements of cerebral autoregulation should be driven by CPP, not ABP alone, (4) volatile gas anesthesia like isoflurane impairs the ability to regulate blood flow and that both static and dynamic methods agree over this impairment.

The major contribution of this thesis is the introduction of non-invasive, bedside compatible measurement of ICP with the potential for use in severe injuries, mild symptoms of elevated ICP, and healthy volunteers alike. I believe that the techniques developed in this thesis have the potential to lessen the burden of many patients that undergo potentially unnecessary surgery to allow for ICP measurements, and I hope that this work can help to describe the pressure and blood flow regulation in the brain, and improve clinical care and patient outcome. I strongly believe that these points should be motivation enough to carry this work forward, and I see a large potential for clinical application.

Glossary

Acronym	Meaning
ABP	Arterial Blood Pressure
ARI	Autoregulation Index
c	Speed of light in vacuum
c_n	Speed of light in medium
CA	Cerebral Autoregulation
CBF	Cerebral Blood Flow
CBFV	Cerebral Blood Flow Velocity
CBV	Cerebral Blood Volume
CPP	Cerebral Perfusion Pressure
CPP _{opt}	Optimal Cerebral Perfusion Pressure
CrCP	Critical Closing Pressure
CSF	Cerebro-Spinal Fluid
CT	Computer Tomography
CVR	Cerebro-Vascular Resistance to flow
DCS	Diffuse Correlation Spectroscopy

ϵ	Molar extinction coefficient
EVD	External Ventricular Drain
g	Light anisotropy factor
GCS	Glasgow Coma Scale
Hb, Δ Hb	Deoxygenated hemoglobin concentration
HbO, Δ HbO	Oxygenated hemoglobin concentration
HbT, Δ HbT	Total hemoglobin concentration
ICP, Δ ICP	Intracranial Pressure
L	Fluence
λ	Wavelength
LLA	Lower Limit of Autoregulation
MAP	Mean Arterial Blood Pressure
mfp_a	Absorption Mean Free Path
mfp_s	Scattering Mean Free Path
MRI	Magnetic Resonance Imaging
MSC	Magnitude Squared Coherence
μ_a	Absorption coefficient
μ_{eff}	Effective light extinction coefficient
μ_s	Scattering coefficient
μ'_s	Reduced Scattering coefficient
n	Refractive index
NHP	Non-Human Primate

NIRS	Near-Infrared Spectroscopy
NPH	Normal Pressure Hydrocephalus
$\hat{\Omega}$	Direction of wave front propagation
ω	oscillation frequency
P	Light Power
PaCO ₂	Partial Pressure of Carbon-Dioxide in Blood
PaO ₂	Partial Pressure of Oxygen in Blood
Φ	Fluence rate
PI	Pulsatility Index
PRx	Pressure Reactivity Index
ρ	Source detector distance
RoR	Rate of Regulation
SAH	Subarachnoid Hemorrhage
SAS	Subarachnoid Space
SNR	Signal to Noise Ratio
StO ₂	Oxygen Saturation of hemoglobin in tissue
TBI	Traumatic Brain Injury
TCD	Transcranial Doppler sonography
ULA	Upper Limit of Autoregulation

Bibliography

- [1] Centers for Disease Control and Prevention, “Surveillance Report of Traumatic Brain Injury-related Emergency Department Visits, Hospitalizations, and Deaths-United States, 2014.” Centers for Disease Control and Prevention, Tech. Rep., 2019. [Online]. Available: www.cdc.gov/TraumaticBrainInjury
- [2] E. J. Benjamin, M. J. Blaha, S. E. Chiuve, M. Cushman, S. R. Das, R. Deo, S. D. De Ferranti, J. Floyd, M. Fornage, C. Gillespie, C. R. Isasi, M. C. Jim’nez, L. C. Jordan, S. E. Judd, D. Lackland, J. H. Lichtman, L. Lisabeth, S. Liu, C. T. Longenecker, R. H. MacKey, K. Matsushita, D. Mozaffarian, M. E. Mussolino, K. Nasir, R. W. Neumar, L. Palaniappan, D. K. Pandey, R. R. Thiagarajan, M. J. Reeves, M. Ritchey, C. J. Rodriguez, G. A. Roth, W. D. Rosamond, C. Sasson, A. Towfighi, C. W. Tsao, M. B. Turner, S. S. Virani, J. H. Voeks, J. Z. Willey, J. T. Wilkins, J. H. Wu, H. M. Alger, S. S. Wong, and P. Muntner, “Heart Disease and Stroke Statistics’2017 Update: A Report from the American Heart Association,” *Circulation*, vol. 135, no. 10, pp. e146–e603, 3 2017.
- [3] Hydrocephalus Association, “Facts and Stats — Hydrocephalus Association.” [Online]. Available: <https://www.hydroassoc.org/about-us/newsroom/facts-and-stats-2/>
- [4] S. Payne, *Cerebral Autoregulation: Control of Blood Flow in the Brain*. Springer International Publishing, 2016, vol. 1.
- [5] X. Zhang, J. E. Medow, B. J. Iskandar, F. Wang, M. Shokouejinejad, J. Koueik, and J. G. Webster, “Invasive and noninvasive means of measuring intracranial pressure: A review,” *Physiological Measurement*, vol. 38, no. 8, pp. R143–R182, 2017.
- [6] J. B. Rosenberg, A. L. Shiloh, R. H. Savel, and L. A. Eisen, “Non-invasive methods of estimating intracranial pressure,” *Neurocritical Care*, vol. 15, no. 3, pp. 599–608, 2011.
- [7] OpenStax, “Cerebrospinal fluid,” 2016. [Online]. Available: https://commons.wikimedia.org/wiki/File:1317_CFS_Circulation.jpg
- [8] H. Cushing, *Studies in intracranial physiology & surgery; the third circulation, the hypophysics, the gliomas*. London: H. Milford, 1926.
- [9] T. Brinker, E. Stopa, J. Morrison, and P. Klinge, “A new look at cerebrospinal fluid circulation,” *Fluids and Barriers of the CNS*, vol. 11, no. 1, p. 10, 2014. [Online]. Available: <http://fluidsbarrierscns.biomedcentral.com/articles/10.1186/2045-8118-11-10>
- [10] S. W. Bothwell, D. Janigro, and A. Patabendige, “Cerebrospinal fluid dynamics and intracranial pressure elevation in neurological diseases,” *Fluids and Barriers of the CNS*, vol. 16, no. 1, pp. 1–18, 2019. [Online]. Available: <https://fluidsbarrierscns.biomedcentral.com/articles/10.1186/2045-8118-16-1>

//doi.org/10.1186/s12987-019-0129-6

- [11] M. H. Wilson, “Monro-Kellie 2.0: The dynamic vascular and venous pathophysiological components of intracranial pressure,” *Journal of Cerebral Blood Flow and Metabolism*, vol. 36, no. 8, pp. 1338–1350, 2016.
- [12] A. Monro, “Observations on the structure and functions of the nervous system,” *Creech and Johnson*, 1783.
- [13] G. Kellie, *An account of the appearances observed in the dissection of two of three individuals presumed to have perished in the storm of the 3d, and whose bodies were discovered in the vicinity of Leith on the morning of the 4th, November 1821 : with some reflectio.* Edinburgh, 1824.
- [14] N. Stocchetti and A. I. Maas, “Traumatic intracranial hypertension,” *New England Journal of Medicine*, vol. 370, no. 22, pp. 2121–2130, 2014.
- [15] W. D. Freeman, “Raised intracranial pressure,” *Evidence-Based Neurology: Management of Neurological Disorders: Second Edition*, vol. 73, no. Suppl I, pp. 87–92, 2015.
- [16] P. M. Kochanek, R. C. Tasker, N. Carney, A. M. Totten, P. D. Adelson, N. R. Selden, C. Davis-O’Reilly, E. L. Hart, M. J. Bell, S. L. Bratton, G. A. Grant, N. Kissoon, K. E. Reuter-Rice, M. S. Vavilala, and M. S. Wainwright, “Guidelines for the Management of Pediatric Severe Traumatic Brain Injury, Third Edition,” *Pediatric Critical Care Medicine*, vol. 20, no. 3S Suppl 1, pp. S1–S82, 3 2019. [Online]. Available: <http://journals.lww.com/00130478-201903001-00001>
- [17] N. Carney, A. M. Totten, C. O’Reilly, J. S. Ullman, G. W. Hawryluk, M. J. Bell, S. L. Bratton, R. Chesnut, O. A. Harris, N. Kissoon, A. M. Rubiano, L. Shutter, R. C. Tasker, M. S. Vavilala, J. Wilberger, D. W. Wright, and J. Ghajar, “Guidelines for the Management of Severe Traumatic Brain Injury, Fourth Edition,” *Neurosurgery*, vol. 80, no. 1, pp. 6–15, 2017.
- [18] S. L. Bratton, R. M. Chestnut, J. Ghajar, F. F. McConnell Hammond, O. A. Harris, R. Hartl, G. T. Manley, A. Nemecek, D. W. Newell, G. Rosenthal, J. Schouten, L. Shutter, S. D. Timmons, J. S. Ullman, W. Videtta, J. E. Wilberger, and D. W. Wright, “VIII. Intracranial Pressure Thresholds,” *Journal of Neurotrauma*, vol. 24, no. supplement 1, pp. S–55–S–58, 5 2007. [Online]. Available: <https://search-proquest-com.proxy.library.cmu.edu/docview/204453928?accountid=9902http://www.liebertpub.com/doi/10.1089/neu.2007.9988>
- [19] F. Güiza, B. Depreitere, I. Piper, G. Citerio, I. Chambers, P. A. Jones, T.-y. Y. M. Lo, P. Enblad, P. Nillson, B. Feyen, P. Jorens, A. Maas, M. U. Schuhmann, R. Donald, L. Moss, G. Van den Berghe, and G. Meyfroidt, “Visualizing the pressure and time burden of intracranial hypertension in adult and paediatric traumatic brain injury,” *Intensive Care Medicine*, vol. 41, no. 6, pp. 1067–1076, 2015.
- [20] J. Jagannathan, D. O. Okonkwo, H. K. Yeoh, A. S. Dumont, D. Saulle, J. Haizlip, J. T. Barth, J. A. S. Jane, and J. A. J. Jane, “Long-term outcomes and prognostic factors in pediatric patients with severe traumatic brain injury and elevated intracranial pressure.” *Journal of neurosurgery. Pediatrics*, vol. 2, no. 4, pp. 240–249, 10 2008.

- [21] V. Kukreti, H. Mohseni-Bod, and J. Drake, "Management of raised intracranial pressure in children with traumatic brain injury," *Journal of Pediatric Neurosciences*, vol. 9, no. 3, pp. 207–215, 2014. [Online]. Available: <http://www.ncbi.nlm.nih.gov/pmc/articles/PMC4302538/>
- [22] M. Andresen, A. Hadi, L. G. Petersen, and M. Juhler, "Effect of postural changes on ICP in healthy and ill subjects," *Acta Neurochirurgica*, vol. 157, no. 1, pp. 109–113, 2014.
- [23] Z. Czosnyka and M. Czosnyka, "Long-term monitoring of intracranial pressure in normal pressure hydrocephalus and other CSF disorders," *Acta Neurochirurgica*, vol. 159, no. 10, pp. 1979–1980, 10 2017. [Online]. Available: <http://link.springer.com/10.1007/s00701-017-3282-1>
- [24] C. Hawthorne and I. Piper, "Monitoring of intracranial pressure in patients with traumatic brain injury," *Frontiers in Neurology*, vol. 5 JUN, no. July, pp. 1–16, 2014.
- [25] U. Kawoos, R. M. McCarron, C. R. Aufer, and M. Chavko, "Advances in intracranial pressure monitoring and its significance in managing traumatic brain injury," *International Journal of Molecular Sciences*, vol. 16, no. 12, pp. 28 979–28 997, 2015.
- [26] S. Boles, C. Martinez-Rios, D. Tibussek, and D. Pohl, "Infantile Idiopathic Intracranial Hypertension: A Case Study and Review of the Literature," *Journal of Child Neurology*, vol. 34, no. 13, pp. 806–814, 2019.
- [27] M. S. Alshuhri, L. Gallagher, C. McCabe, and W. M. Holmes, "Change in CSF Dynamics Responsible for ICP Elevation After Ischemic Stroke in Rats: a New Mechanism for Unexplained END?" *Translational Stroke Research*, 2019.
- [28] E. Jüttler, P. D. Schellinger, A. Aschoff, K. Zweckberger, A. Unterberg, and W. Hacke, "Clinical review: Therapy for refractory intracranial hypertension in ischaemic stroke," *Critical Care*, vol. 11, no. 5, 2007.
- [29] Johns Hopkins Medicine, "Increased Intracranial Pressure (ICP) Headache." [Online]. Available: <https://www.hopkinsmedicine.org/health/conditions-and-diseases/headache/increased-intracranial-pressure-icp-headache>
- [30] NORD (National Organization for Rare Disorders), "Idiopathic Intracranial Hypertension." [Online]. Available: <https://rarediseases.org/rare-diseases/idiopathic-intracranial-hypertension/>
- [31] M. I. Hirzallah and H. A. Choi, "The Monitoring of Brain Edema and Intracranial Hypertension," *Journal of Neurocritical Care*, vol. 9, no. 2, pp. 92–104, 2016.
- [32] B. R. R. M. Chestnut, G. Clifton, J. Ghajar, D. W. Marion, R. K. Naryan, D. W. Newell, L. H. Pitts, M. J. Rosner, and J. W. Wilberger, "Guidelines for the management of severe head injury," *European Journal of Emergency Medicine*, vol. 3, no. 2, pp. 109–127, 6 1996. [Online]. Available: <http://journals.lww.com/00063110-199606000-00010>
- [33] N. A. Lassen and M. S. Christensen, "Physiology of cerebral blood flow," *Br.J. Anaesth.*, vol. 48, p. 719, 1976.
- [34] B. B. Allen, Y. L. Chiu, L. M. Gerber, J. Ghajar, and J. P. Greenfield, "Age-specific cerebral perfusion pressure thresholds and survival in children and adolescents with severe

- traumatic brain injury,” *Pediatric Critical Care Medicine*, vol. 15, no. 1, pp. 62–70, 2014.
- [35] E. Needham, C. McFadyen, V. Newcombe, A. Synnot, M. Czosnyka, and D. Menon, “Cerebral Perfusion Pressure Targets Individualized to Pressure-Reactivity Index in Moderate to Severe Traumatic Brain Injury: A Systematic Review,” *Journal of Neurotrauma*, vol. 8, p. Epub ahead of print, 6 2016. [Online]. Available: <http://dx.doi.org/10.1089/neu.2016.4450>
- [36] M. E. Lovett, N. F. O’Brien, and J. R. Leonard, “Children With Severe Traumatic Brain Injury, Intracranial Pressure, Cerebral Perfusion Pressure, What Does it Mean? A Review of the Literature,” *Pediatric Neurology*, vol. 94, pp. 3–20, 2019. [Online]. Available: <https://doi.org/10.1016/j.pediatrneurol.2018.12.003>
- [37] Hydrocephalus Association, “Classifications and Causes — Hydrocephalus Association.” [Online]. Available: <https://www.hydroassoc.org/classifications-and-causes/>
- [38] National Institute of Neurological Disorders and Stroke, “Hydrocephalus Fact Sheet.” [Online]. Available: https://www.ninds.nih.gov/Disorders/Patient-Caregiver-Education/Fact-Sheets/Hydrocephalus-Fact-Sheet#3125_2
- [39] Hydrocephalus Association, “Treatment.” [Online]. Available: <https://www.hydroassoc.org/treatment/>
- [40] P. Seners and J. C. Baron, “Revisiting ‘progressive stroke’: incidence, predictors, pathophysiology, and management of unexplained early neurological deterioration following acute ischemic stroke,” *Journal of Neurology*, vol. 265, no. 1, pp. 216–225, 2018.
- [41] D. J. Beard, D. D. McLeod, C. L. Logan, L. A. Murtha, M. S. Imtiaz, D. F. van Helden, and N. J. Spratt, “Intracranial pressure elevation reduces flow through collateral vessels and the penetrating arterioles they supply. A possible explanation for ‘collateral failure’ and infarct expansion after ischemic stroke,” *Journal of Cerebral Blood Flow & Metabolism*, vol. 35, no. 5, pp. 861–872, 2015. [Online]. Available: <http://www.nature.com/doi/10.1038/jcbfm.2015.2>
- [42] A. M. Thabet, M. Kottapally, and J. C. Hemphill, “Management of intracerebral hemorrhage,” *Handbook of Clinical Neurology*, vol. 140, no. 5, pp. 177–194, 2017.
- [43] J. Guillaume and P. Janny, “[Continuous intracranial manometry; importance of the method and first results].” *Revue neurologique*, vol. 84, no. 2, pp. 131–42, 2 1951. [Online]. Available: <http://www.ncbi.nlm.nih.gov/pubmed/14845379>
- [44] N. Lundberg, “Continuous recording and control of ventricular fluid pressure in neurosurgical practice.” *Acta psychiatrica Scandinavica. Supplementum*, vol. 36, no. 149, pp. 1–193, 1960.
- [45] N. Lundberg, H. Troupp, and H. Lorin, “Continuous Recording of the Ventricular-Fluid Pressure in Patients with Severe Acute Traumatic Brain Injury,” *Journal of Neurosurgery*, vol. 22, no. 6, 1965.
- [46] S. C. Meyerson, P. A. Avan, and B. Buki, “Non-Invasive Method and Apparatus for Monitoring Intracranial Pressure,” 2001.
- [47] S. Antes, C. A. Tschan, M. Heckelmann, D. Breuskin, and J. Oertel,

- “Telemetric Intracranial Pressure Monitoring with the Raumedic Neurovent P-tel,” *World Neurosurgery*, vol. 91, pp. 133–148, 2016. [Online]. Available: <http://dx.doi.org/10.1016/j.wneu.2016.03.096>
- [48] P. H. Raboel, J. Bartek, M. Andresen, B. M. Bellander, B. Romner, and J. F. Stover, “Intracranial pressure monitoring: Invasive versus non-invasive methods-A review,” *Critical Care Research and Practice*, vol. 2012, pp. 3–7, 2012. [Online]. Available: <http://downloads.hindawi.com/journals/ccrp/2012/950393.pdf>
- [49] V. Speck, D. Staykov, H. B. Huttner, R. Sauer, S. Schwab, and J. Bardutzky, “Lumbar catheter for monitoring of intracranial pressure in patients with post-hemorrhagic communicating hydrocephalus,” *Neurocritical Care*, vol. 14, no. 2, pp. 208–215, 2011.
- [50] M. Czosnyka, J. D. Pickard, and N. F. O. R. Neurologists, “Monitoring and interpretation of intracranial pressure.” *Journal of neurology, neurosurgery, and psychiatry*, vol. 75, no. 6, pp. 813–21, 6 2004. [Online]. Available: <http://www.ncbi.nlm.nih.gov/pubmed/15145991><http://www.pubmedcentral.nih.gov/articlerender.fcgi?artid=PMC1739058>
- [51] A. Edouard, E. Vanhille, S. Le Moigno, D. Benhamou, and J.-X. Mazoit, “Non-invasive assessment of cerebral perfusion pressure in brain injured patients with moderate intracranial hypertension,” *British Journal of Anaesthesia*, vol. 94, no. 2, pp. 216–221, 2 2005. [Online]. Available: <https://linkinghub.elsevier.com/retrieve/pii/S0007091217357355>
- [52] D. G. Barone and M. Czosnyka, “Brain monitoring: Do we need a hole? An update on invasive and noninvasive brain monitoring modalities,” *The Scientific World Journal*, vol. 2014, 2014.
- [53] D. S. Nag, S. Sahu, A. Swain, and S. Kant, “Intracranial pressure monitoring: Gold standard and recent innovations,” *World Journal of Clinical Cases*, vol. 7, no. 13, pp. 1535–1553, 2019.
- [54] A. Reid, R. J. Marchbanks, D. M. Burge, A. M. Martin, D. E. Bateman, J. D. Pickard, and A. P. Brightwell, “The relationship between intracranial pressure and tympanic membrane displacement,” *British Journal of Audiology*, vol. 24, no. 2, pp. 123–129, 1 1990. [Online]. Available: <https://doi.org/10.3109/03005369009077853><http://www.tandfonline.com/doi/full/10.3109/03005369009077853>
- [55] M. K. Azad, A. Spiewak, R. H. Sandler, K. Manwaring, P. Manwaring, and H. A. Mansy, “Monitoring Intracranial Pressure Using Non-Invasive Brain Stethoscope,” in *SoutheastCon 2018*, vol. 2018-April. IEEE, 4 2018, pp. 1–5. [Online]. Available: <https://ieeexplore.ieee.org/document/8478919/>
- [56] S. Gwer, V. Sheward, A. Birch, R. Marchbanks, R. Idro, C. R. Newton, F. J. Kirkham, J.-p. P. Lin, and M. Lim, “The tympanic membrane displacement analyser for monitoring intracranial pressure in children,” *Child’s Nervous System*, vol. 29, no. 6, pp. 927–933, 2013.
- [57] A. Amini, H. Kariman, A. Arhami Dolatabadi, H. R. Hatamabadi, H. Derakhshanfar, B. Mansouri, S. Safari, and R. Eqtesadi, “Use of the sonographic diameter of optic nerve sheath to estimate intracranial pressure,” *American Journal of Emergency*

- Medicine*, vol. 31, no. 1, pp. 236–239, 1 2013. [Online]. Available: <http://www.ncbi.nlm.nih.gov/pubmed/22944553><http://dx.doi.org/10.1016/j.ajem.2012.06.025>
- [58] C. Robba, G. Santori, M. Czosnyka, F. Corradi, N. Bragazzi, L. Padayachy, F. S. Taccone, and G. Citerio, “Optic nerve sheath diameter measured sonographically as non-invasive estimator of intracranial pressure: a systematic review and meta-analysis,” *Intensive Care Medicine*, vol. 44, no. 8, pp. 1284–1294, 2018. [Online]. Available: <https://doi.org/10.1007/s00134-018-5305-7>
- [59] C. Robba, D. Cardim, M. Czosnyka, F. Abecasis, S. Pezzato, S. Buratti, A. Moscatelli, C. Sortica, F. Racca, P. Pelosi, and F. Rasulo, “Ultrasound non-invasive intracranial pressure assessment in paediatric neurocritical care: a pilot study,” *Child’s Nervous System*, vol. 36, no. 1, pp. 117–124, 1 2020. [Online]. Available: <http://link.springer.com/10.1007/s00381-019-04235-8>
- [60] A. A. Figaji, E. Zwane, A. G. Fieggen, P. Siesjo, and J. C. Peter, “Transcranial Doppler pulsatility index is not a reliable indicator of intracranial pressure in children with severe traumatic brain injury,” *Surgical Neurology*, vol. 72, no. 4, pp. 389–394, 10 2009. [Online]. Available: <http://www.ncbi.nlm.nih.gov/pubmed/19608224><https://linkinghub.elsevier.com/retrieve/pii/S0090301909002249>
- [61] A. Behrens, N. Lenfeldt, K. Ambarki, J. Malm, A. Eklund, and L.-O. Koskinen, “Transcranial Doppler Pulsatility Index: Not an Accurate Method to Assess Intracranial Pressure,” *Neurosurgery*, vol. 66, no. 6, pp. 1050–1057, 2010. [Online]. Available: <http://dx.doi.org/10.1227/01.NEU.0000369519.35932.F2>
- [62] J. Bellner, B. Romner, P. Reinstrup, K.-a. A. Kristiansson, E. Ryding, L. Brandt, P. Index, P. I. Reflects, K.-a. A. Kristiansson, E. Ryding, D. Ph, L. Brandt, D. Ph, J. Bellner, B. Romner, P. Reinstrup, K.-a. A. Kristiansson, E. Ryding, and L. Brandt, “Transcranial Doppler sonography pulsatility index (PI) reflects intracranial pressure (ICP),” *Surgical Neurology*, vol. 62, no. 1, pp. 45–51, 2004.
- [63] C. Thees, M. Scholz, C. Schaller, A. Gass, C. Pavlidis, A. Weyland, and A. Hoeft, “Relationship between intracranial pressure and critical closing pressure in patients with neurotrauma,” *Anesthesiology*, vol. 96, no. 3, pp. 595–599, 2002.
- [64] K.-C. Wu, P. Farzam, F. Sheriff, P. Y. Farzam, S. L. Michaud, A. D. Monk, M. A. Aziz-Sultan, N. Patel, H. Vaitkevicius, M. A. Franceschini, and M. A. Franceschini, “Critical Closing Pressure Measured in Stroke Patients with Diffuse Correlation Spectroscopy and Transcranial Doppler Ultrasound,” in *Biophotonics Congress: Optics in the Life Sciences Congress 2019 (BODA,BRAIN,NTM,OMA,OMP)*. Washington, D.C.: OSA, 4 2019, p. BW4A.4. [Online]. Available: <https://www.osapublishing.org/abstract.cfm?URI=BRAIN-2019-BW4A.4>
- [65] W. B. Baker, A. B. Parthasarathy, K. P. Gannon, V. C. Kavuri, D. R. Busch, K. Abramson, L. He, R. C. Mesquita, M. T. Mullen, J. A. Detre, J. H. Greenberg, D. J. Licht, R. Balu, W. A. Kofke, A. G. Yodh, A. Kofke, and A. G. Yodh, “Noninvasive optical monitoring of critical closing pressure and arteriole compliance in human subjects,” *Journal of Cerebral Blood Flow & Metabolism*, vol. 37, no. 8, pp. 2691–2705, 8 2017.

[Online]. Available: https://journals.sagepub.com/doi/pdf/10.1177/0271678X17709166?casa_token=vwWjeWx1BtIAAAA:eGcIipMR_T7x92QFt4Vov0MZKQ1pvY5_H2e1NeA98gJStow_eD3jT9f32C4tt11XlJf4NfrKn602iwhttp://journals.sagepub.com/doi/10.1177/0271678X17709166

- [66] W. B. Baker, T. M. Flanders, R. Balu, L. He, K. Heye, E. Mahanna Gabrielli, J. J. Flibotte, D. J. Licht, G. G. Heuer, A. G. Yodh, and W. A. Kofke, “Non-invasive optical assessment of intracranial pressure: pilot results in human patients,” in *Diffuse Optical Spectroscopy and Imaging VII*, H. Dehghani and H. Wabnitz, Eds., vol. 11074. SPIE, 7 2019, p. 14. [Online]. Available: <https://www.spiedigitallibrary.org/conference-proceedings-of-spie/11074/2527122/Non-invasive-optical-assessment-of-intracranial-pressure--pilot-results/10.1117/12.2527122.full>
- [67] M. Ursino, “A Mathematical Study of Human Intracranial Hydrodynamics Part 1 - The Cerebrospinal Fluid Pulse Pressure,” *Annals of biomedical engineering*, vol. 16, no. 30, pp. 379–401, 1988.
- [68] K. J. Lee, C. Park, J. Oh, and B. Lee, “Non-invasive detection of intracranial hypertension using a simplified intracranial hemo- and hydro-dynamics model,” *BioMedical Engineering OnLine*, vol. 14, no. 1, p. 51, 2015. [Online]. Available: <http://www.biomedical-engineering-online.com/content/14/1/51>
- [69] A. Fanelli, F. W. Vonberg, K. L. LaRovere, B. K. Walsh, E. R. Smith, S. Robinson, R. C. Tasker, and T. Heldt, “Fully automated, real-time, calibration-free, continuous noninvasive estimation of intracranial pressure in children,” *Journal of Neurosurgery: Pediatrics*, vol. 24, no. 5, pp. 509–519, 2019.
- [70] M. Swoboda, M. G. Hochman, F. J. Fritz, and T. W. . B. R. T. J. S. Gopagoni, Sundeep; Scharf, “Non-invasive intracranial pressure sensor,” pp. 1–38, 2013. [Online]. Available: <https://www.google.com/patents/US20130289422>
- [71] K. P. Budohoski, C. Zweifel, M. Kasprowicz, E. Sorrentino, J. Diedler, K. M. Brady, P. Smielewski, D. K. Menon, J. D. Pickard, P. J. Kirkpatrick, and M. Czosnyka, “What comes first? the dynamics of cerebral oxygenation and blood flow in response to changes in arterial pressure and intracranial pressure after head injury,” *British Journal of Anaesthesia*, vol. 108, no. 1, pp. 89–99, 2012.
- [72] J. B. Fischer, A. Ghouse, S. Tagliabue, F. Maruccia, R. Zucca, U. M. Weigel, J. Sahuquillo, M. A. Poca, and T. Durduran, “Machine learning for the derivation of an intracranial pressure index using the waveform of the cerebral blood flow measured noninvasively using fast diffuse correlation spectroscopy,” *European Conferences on Biomedical Optics, Diffuse Optical Spectroscopy and Imaging VII, Clinical Application of Diffuse Optics, Munich (Germany)*, Tech. Rep., 2019.
- [73] N. A. Lassen, “Cerebral blood flow and oxygen consumption in man.” *Physiological reviews*, vol. 39, no. 2, pp. 183–238, 1959. [Online]. Available: <http://physrev.physiology.org/content/39/2/183>
- [74] M. S. Vavilala, L. A. Lee, K. Boddu, E. Visco, D. W. Newell, J. J. Zimmerman, and A. M. Lam, “Cerebral autoregulation in pediatric traumatic brain injury,” *Pediatric Critical Care*

Medicine, vol. 5, no. 3, pp. 257–263, 2004.

- [75] N. Focus, L. Rangel-Castilla, J. Gasco, H. J. W. Nauta, D. O. Okonkwo, and C. S. Robertson, “Cerebral pressure autoregulation in traumatic brain injury,” *Neurosurgical Focus*, vol. 25, no. 4, p. E7, 2008. [Online]. Available: <http://thejns.org/doi/10.3171/FOC.2008.25.10.E7>
- [76] A. D. Lalou, M. Czosnyka, J. Donnelly, J. D. Pickard, E. Nabbanja, N. C. Keong, M. Garnett, and Z. H. Czosnyka, “Cerebral autoregulation, cerebrospinal fluid outflow resistance, and outcome following cerebrospinal fluid diversion in normal pressure hydrocephalus,” *Journal of Neurosurgery*, vol. 130, no. 1, pp. 154–162, 2019.
- [77] P. Eames, M. Blake, S. Dawson, R. Panerai, and J. Potter, “Dynamic cerebral autoregulation and beat to beat blood pressure control are impaired in acute ischaemic stroke,” *Journal of Neurology, Neurosurgery, and Psychiatry*, vol. 72, no. 4, pp. 467–472, 4 2002. [Online]. Available: <http://www.ncbi.nlm.nih.gov/pmc/articles/PMC1737824/>
- [78] A. Messere and S. Roatta, “Influence of cutaneous and muscular circulation on spatially resolved versus standard Beer-Lambert near-infrared spectroscopy.” *Physiological reports*, vol. 1, no. 7, p. e00179, 2013. [Online]. Available: <http://www.pubmedcentral.nih.gov/articlerender.fcgi?artid=3970749&tool=pmcentrez&rendertype=abstract>
- [79] J. G. Betts, K. A. Young, J. A. Wise, E. Johnson, B. Poe, D. H. Kruse, O. Korol, J. E. Johnson, M. Womble, and P. DeSaix, *Anatomy and Physiology*. Houston, Texas: OpenStax, 2013.
- [80] H. Ito, I. Kanno, H. Iida, J. Hatazawa, E. Shimosegawa, H. Tamura, and T. Okudera, “Arterial fraction of cerebral blood volume in humans measured by positron emission tomography,” *Annals of Nuclear Medicine*, vol. 15, no. 2, pp. 111–116, 2001.
- [81] Lonza Group Ltd, “An Introduction to Primary Endothelial Cells — Lonza.” [Online]. Available: https://bioscience.lonza.com/lonza_bs/CH/en/endothelial-cells
- [82] K. B. Chandran, S. E. Rittgers, and A. P. Yoganathan, *Biofluid Mechanics: The Human Circulation*. Taylor & Francis, 2006. [Online]. Available: <https://books.google.com/books?id=Lm0fUjchxUC>
- [83] A. Sato, K. Terata, H. Miura, K. Toyama, F. R. Loberiza, O. A. Hatoum, T. Saito, I. Sakuma, and D. D. Gutterman, “Mechanism of vasodilation to adenosine in coronary arterioles from patients with heart disease,” *American Journal of Physiology-Heart and Circulatory Physiology*, vol. 288, no. 4, pp. H1633–H1640, 4 2005. [Online]. Available: <https://www.physiology.org/doi/10.1152/ajpheart.00575.2004>
- [84] W. F. Boron and E. L. Boulpaep, *Medical physiology : a cellular and molecular approach*, 2nd ed. Philadelphia, PA : Saunders/Elsevier, 2009. [Online]. Available: http://bvbr.bib-bvb.de:8991/F?func=service&doc_library=BVB01&doc_number=016999707&line_number=0001&func_code=DB_RECORDS&service_type=MEDIA
- [85] N. Toda, K. Ayajiki, and T. Okamura, “Cerebral Blood Flow Regulation by Nitric Oxide: Recent Advances,” *Pharmacological Reviews*, vol. 61, no. 1, pp. 62–97, 3 2009. [Online]. Available: <http://pharmrev.aspetjournals.org/lookup/doi/10.1124/pr.108.000547>

- [86] G. M. Buga, M. E. Gold, J. M. Fukuto, and L. J. Ignarro, "Shear stress-induced release of nitric oxide from endothelial cells grown on beads," *Hypertension*, vol. 17, no. 2, pp. 187–193, 1991.
- [87] A. L. Vazquez, M. Fukuda, and S. G. Kim, "Inhibitory Neuron Activity Contributions to Hemodynamic Responses and Metabolic Load Examined Using an Inhibitory Optogenetic Mouse Model," *Cerebral Cortex*, vol. 28, no. 11, pp. 4105–4119, 2018.
- [88] N. Toda and T. Okamura, "The pharmacology of nitric oxide in the peripheral nervous system of blood vessels," pp. 271–324, 6 2003.
- [89] D. Attwell, A. Mishra, C. N. Hall, F. M. O'Farrell, and T. Dalkara, "What is a pericyte?" *Journal of Cerebral Blood Flow and Metabolism*, vol. 36, no. 2, pp. 451–455, 2016.
- [90] C. N. Hall, C. Reynell, B. Gesslein, N. B. Hamilton, A. Mishra, B. A. Sutherland, F. M. O. Farrell, A. M. Buchan, M. Lauritzen, D. Attwell, F. M. Oâ Farrell, A. M. Buchan, M. Lauritzen, and D. Attwell, "Capillary pericytes regulate cerebral blood flow in health and disease," *Nature*, vol. 508, no. 1, pp. 55–60, 2014. [Online]. Available: <http://dx.doi.org/10.1038/nature13165>
- [91] M. Ter Laan, J. M. Van Dijk, J. W. Elting, M. J. Staal, and A. R. Absalom, "Sympathetic regulation of cerebral blood flow in humans: A review," *British Journal of Anaesthesia*, vol. 111, no. 3, pp. 361–367, 2013. [Online]. Available: <http://dx.doi.org/10.1093/bja/aet122>
- [92] J. M. Murkin, "Cerebral autoregulation: The role of CO₂ in metabolic homeostasis," *Seminars in Cardiothoracic and Vascular Anesthesia*, vol. 11, no. 4, pp. 269–273, 2007.
- [93] E. Carrera, L. K. Lee, S. Giannopoulos, and R. S. Marshall, "Cerebrovascular reactivity and cerebral autoregulation in normal subjects," *Journal of the Neurological Sciences*, vol. 285, no. 1-2, pp. 191–194, 2009. [Online]. Available: <http://dx.doi.org/10.1016/j.jns.2009.06.041>
- [94] S. K. Piechnik, X. Yang, M. Czosnyka, P. Smielewski, S. H. Fletcher, A. L. Jones, and J. D. Pickard, "The continuous assessment of cerebrovascular reactivity: A validation of the method in healthy volunteers," *Anesthesia and Analgesia*, vol. 89, no. 4, pp. 944–949, 1999.
- [95] R. B. Panerai, S. T. Deverson, P. Mahony, P. Hayes, and D. H. Evans, "Effect of CO₂ on dynamic cerebral autoregulation measurement," *Physiological Measurement*, vol. 20, no. 3, pp. 265–275, 1999.
- [96] P. N. Ainslie, L. Celi, K. McGrattan, K. Peebles, and S. Ogoh, "Dynamic cerebral autoregulation and baroreflex sensitivity during modest and severe step changes in arterial PCO₂," *Brain Research*, vol. 1230, pp. 115–124, 2008.
- [97] L. Meng and A. W. Gelb, "Regulation of Cerebral Autoregulation by Carbon Dioxide," *Anesthesiology*, vol. 122, no. 1, pp. 196–205, 1 2015. [Online]. Available: <http://content.wkhealth.com/linkback/openurl?sid=WKPTLP:landingpage&an=00000542-201501000-00033>
- [98] S. Ogoh, H. Nakahara, P. N. Ainslie, and T. Miyamoto, "The effect of oxygen on dynamic

cerebral autoregulation: Critical role of hypocapnia,” *Journal of Applied Physiology*, vol. 108, no. 3, pp. 538–543, 2010.

- [99] D. M. Bailey, K. A. Evans, P. E. James, J. Mceneny, I. S. Young, L. Fall, M. Gutowski, E. Kewley, J. M. Mccord, K. Møller, and P. N. Ainslie, “Altered free radical metabolism in acute mountain sickness: Implications for dynamic cerebral autoregulation and blood-brain barrier function,” *Journal of Physiology*, vol. 587, no. 1, pp. 73–85, 2009.
- [100] H. Katsukawa, Y. Ogawa, K. Aoki, R. Yanagida, and K. Iwasaki, “[Acute mild hypoxia impairment of dynamic cerebral autoregulation assessed by spectral analysis and thigh-cuff deflation].” *Nihon eiseigaku zasshi. Japanese journal of hygiene*, vol. 67, no. 4, pp. 508–513, 2012.
- [101] J. S. Querido, P. N. Ainslie, G. E. Foster, W. R. Henderson, J. R. Halliwill, N. T. Ayas, and A. W. Sheel, “Dynamic cerebral autoregulation during and following acute hypoxia: Role of carbon dioxide,” *Journal of Applied Physiology*, vol. 114, no. 9, pp. 1183–1190, 2013.
- [102] M. Balestreri, M. Czosnyka, L. A. Steiner, M. Hiler, E. A. Schmidt, B. Matta, D. Menon, P. Hutchinson, and J. D. Pickard, “Association between outcome, cerebral pressure reactivity and slow ICP waves following head injury,” *Acta Neurochirurgica, Supplementum*, no. 95, pp. 25–28, 2005.
- [103] M. Balestreri, M. Czosnyka, L. A. Steiner, E. Schmidt, P. Smielewski, B. Matta, J. D. Pickard, C. S. Robertson, L. T. Dunn, and I. R. Chambers, “Intracranial hypertension: What additional information can be derived from ICP waveform after head injury?” *Acta Neurochirurgica*, vol. 146, no. 2, pp. 131–141, 2004.
- [104] M. Czosnyka, C. Miller, P. Le Roux, D. K. Menon, P. Vespa, G. Citerio, M. K. Bader, G. M. Brophy, M. N. Diringer, N. Stocchetti, W. Videtta, R. Armonda, N. Badjatia, J. Boesel, R. Chesnut, S. Chou, J. Claassen, M. De Georgia, A. Figaji, J. Fugate, R. Helbok, D. Horowitz, P. Hutchinson, M. Kumar, M. McNett, A. Naidech, M. Oddo, D. W. Olson, K. O’Phelan, J. Provencio, C. Puppò, R. Riker, C. Robertson, J. M. Schmidt, and F. Taccone, “Monitoring of Cerebral Autoregulation,” *Neurocritical Care*, vol. 21, no. 2, pp. 95–102, 2014.
- [105] B. Jennett and M. Bond, “Assessment of outcome after severe brain damage.” *Lancet (London, England)*, vol. 1, no. 7905, pp. 480–484, 3 1975.
- [106] E. Sorrentino, J. Diedler, M. Kasprowicz, K. P. Budohoski, C. Haubrich, P. Smielewski, J. G. Outtrim, A. Manktelow, P. J. Hutchinson, J. D. Pickard, D. K. Menon, and M. Czosnyka, “Critical thresholds for cerebrovascular reactivity after traumatic brain injury,” *Neurocritical Care*, vol. 16, no. 2, pp. 258–266, 2012.
- [107] M. Jaeger, M. U. Schuhmann, M. Soehle, and J. Meixensberger, “Continuous assessment of cerebrovascular autoregulation after traumatic brain injury using brain tissue oxygen pressure reactivity,” *Critical Care Medicine*, vol. 34, no. 6, pp. 1783–1788, 6 2006.
- [108] J. M. Lam, J. N. Hsiang, and W. S. Poon, “Monitoring of autoregulation using laser Doppler flowmetry in patients with head injury,” *Journal of Neurosurgery*, vol. 86, no. 3, pp. 438–445, 3 1997. [Online]. Available: <http://www.ncbi.nlm.nih.gov/pubmed/9046300>

- [109] R. B. Panerai, V. Kerins, L. Fan, P. M. Yeoman, T. Hope, and D. H. Evans, "Association between dynamic cerebral autoregulation and mortality in severe head injury," *British Journal of Neurosurgery*, vol. 18, no. 5, pp. 471–479, 2004. [Online]. Available: <https://doi.org/10.1080/02688690400012343>
- [110] M. S. Vavilala, N. Tontisirin, Y. Udomphorn, W. Armstead, J. J. Zimmerman, R. Chesnut, and A. M. Lam, "Hemispheric differences in cerebral autoregulation in children with moderate and severe traumatic brain injury," *Neurocritical Care*, vol. 9, no. 1, pp. 45–54, 2008.
- [111] M. S. Vavilala, S. Muangman, N. Tontisirin, D. Fisk, C. Roscigno, P. Mitchell, C. Kirkness, J. J. Zimmerman, R. Chesnut, and A. M. Lam, "Impaired cerebral autoregulation and 6-month outcome in children with severe traumatic brain injury: Preliminary findings," *Developmental Neuroscience*, vol. 28, no. 4-5, pp. 348–353, 2006.
- [112] L. a. Steiner, M. Czosnyka, S. K. Piechnik, P. Smielewski, D. Chatfield, D. K. Menon, J. D. Pickard, L. a. Steiner, M. Czosnyka, M. Czosnyka, S. K. Piechnik, S. K. Piechnik, P. Smielewski, P. Smielewski, D. Chatfield, D. Chatfield, D. K. Menon, D. K. Menon, J. D. Pickard, and J. D. Pickard, "Continuous monitoring of cerebrovascular pressure reactivity allows determination of optimal cerebral perfusion pressure in patients with traumatic brain injury." *Critical care medicine*, vol. 30, no. 4, pp. 733–8, 2002. [Online]. Available: <http://www.ncbi.nlm.nih.gov/pubmed/11940737>
- [113] C. Zweifel, A. Lavinio, L. A. Steiner, D. Radolovich, P. Smielewski, I. Timofeev, M. Hiler, M. Balestreri, P. J. Kirkpatrick, J. D. Pickard, P. Hutchinson, and M. Czosnyka, "Continuous monitoring of cerebrovascular pressure reactivity in patients with head injury," *Neurosurgical Focus*, vol. 25, no. 4, p. E2, 2008. [Online]. Available: <http://thejns.org/doi/10.3171/FOC.2008.25.10.E2>
- [114] S. Momjian, B. K. Owler, Z. Czosnyka, M. Czosnyka, A. Pena, and J. D. Pickard, "Pattern of white matter regional cerebral blood flow and autoregulation in normal pressure hydrocephalus," *Brain*, vol. 127, no. 5, pp. 965–972, 2004.
- [115] Z. H. Czosnyka, M. Czosnyka, P. C. Whitfield, T. Donovan, J. D. Pickard, T. H. Milhorat, W. R. Selman, F. Gjerris, and M. Juhler, "Cerebral autoregulation among patients with symptoms of hydrocephalus," *Neurosurgery*, vol. 50, no. 3, pp. 526–533, 2002.
- [116] S. L. Dawson, M. J. Blake, R. B. Panerai, and J. F. Potter, "Dynamic but not static cerebral autoregulation is impaired in acute ischaemic stroke," *Cerebrovascular Diseases*, vol. 10, no. 2, pp. 126–132, 2000.
- [117] N. P. Saeed, R. B. Panerai, M. A. Horsfield, and T. G. Robinson, "Does stroke subtype and measurement technique influence estimation of cerebral autoregulation in acute ischaemic stroke?" *Cerebrovascular Diseases*, vol. 35, no. 3, pp. 257–261, 2013.
- [118] Z. N. Guo, J. Liu, Y. Xing, S. Yan, C. Lv, H. Jin, and Y. Yang, "Dynamic cerebral autoregulation is heterogeneous in different subtypes of acute ischemic stroke," *PLoS ONE*, vol. 9, no. 3, pp. 1–6, 2014.
- [119] E. R. Atkins, F. G. Brodie, S. E. Rafelt, R. B. Panerai, and T. G. Robinson, "Dynamic cerebral autoregulation is compromised acutely following mild ischaemic stroke but not

- transient ischaemic attack,” *Cerebrovascular Diseases*, vol. 29, no. 3, pp. 228–235, 2010.
- [120] M. J. Aries, J. W. Elting, J. De Keyser, B. P. Kremer, and P. C. Vroomen, “Cerebral autoregulation in stroke: A review of transcranial doppler studies,” *Stroke*, vol. 41, no. 11, pp. 2697–2704, 2010.
- [121] M. Reinhard, S. Rutsch, J. Lambeck, C. Wihler, M. Czosnyka, C. Weiller, and A. Hetzel, “Dynamic cerebral autoregulation associates with infarct size and outcome after ischemic stroke,” *Acta Neurologica Scandinavica*, vol. 125, no. 3, pp. 156–162, 2012.
- [122] K. P. Budohoski, M. Czosnyka, P. J. Kirkpatrick, M. Reinhard, G. V. Varsos, M. Kaspro-
wicz, M. Ząbek, J. D. Pickard, and P. Smielewski, “Bilateral Failure of Cerebral Autoregulation is Related to Unfavorable Outcome After Subarachnoid Hemorrhage,” *Neurocritical Care*, vol. 22, no. 1, pp. 65–73, 2015.
- [123] K. P. Budohoski, M. Czosnyka, and P. J. Kirkpatrick, “The role of monitoring cerebral autoregulation after subarachnoid hemorrhage,” *Neurosurgery*, vol. 62, no. 1, pp. 180–184, 2015.
- [124] J. M. Lam, P. Smielewski, M. Czosnyka, J. D. Pickard, and P. J. Kirkpatrick, “Predicting delayed ischemic deficits after aneurysmal subarachnoid hemorrhage using a transient hyperemic response test of cerebral autoregulation,” *Neurosurgery*, vol. 47, no. 4, pp. 819–826, 2000.
- [125] L. Ma, J. S. Roberts, C. Pihoker, T. L. Richards, D. W. Shaw, K. I. Marro, and M. S. Vavilala, “Transcranial doppler-based assessment of cerebral autoregulation in critically ill children during diabetic ketoacidosis treatment,” *Pediatric Critical Care Medicine*, vol. 15, no. 8, pp. 742–749, 2014.
- [126] L. C. Vianna, S. H. Deo, A. K. Jensen, S. W. Holwerda, M. C. Zimmerman, and P. J. Fadel, “Impaired dynamic cerebral autoregulation at rest and during isometric exercise in type 2 diabetes patients,” *American Journal of Physiology - Heart and Circulatory Physiology*, vol. 308, no. 7, pp. 681–687, 2015.
- [127] J. A. Claassen and R. Zhang, “Cerebral autoregulation in Alzheimer’s disease,” *Journal of Cerebral Blood Flow and Metabolism*, vol. 31, no. 7, pp. 1572–1577, 2011.
- [128] A. Abeelen, J. Lagro, A. Beek, and J. Claassen, “Impaired Cerebral Autoregulation and Vasomotor Reactivity in Sporadic Alzheimer’s Disease,” *Current Alzheimer Research*, vol. 11, no. 1, pp. 11–17, 2014.
- [129] M. Reinhard, T. Müller, M. Roth, B. Guschlbauer, J. Timmer, and A. Hetzel, “Bilateral severe carotid artery stenosis or occlusion - Cerebral autoregulation dynamics and collateral flow patterns,” *Acta Neurochirurgica*, vol. 145, no. 12, pp. 1053–1060, 2003.
- [130] M. Reinhard, M. Roth, T. Müller, B. Guschlbauer, J. Timmer, M. Czosnyka, and A. Hetzel, “Effect of carotid endarterectomy or stenting on impairment of dynamic cerebral autoregulation,” *Stroke*, vol. 35, no. 6, pp. 1381–1387, 2004.
- [131] F. Urbano, F. Roux, J. Schindler, and V. Mohsenin, “Impaired cerebral autoregulation in obstructive sleep apnea,” *Journal of Applied Physiology*, vol. 105, no. 6, pp. 1852–1857, 2008.

- [132] N. Nasr, A. P. L. Traon, M. Czosnyka, M. Tiberge, E. Schmidt, and V. Larrue, "Cerebral autoregulation in patients with obstructive sleep apnea syndrome during wakefulness," *European Journal of Neurology*, vol. 16, no. 3, pp. 386–391, 2009.
- [133] E. Khandelwal, A. K. Jaryal, and K. K. Deepak, "Cardiovascular autonomic functions & cerebral autoregulation in patients with orthostatic hypotension." *The Indian journal of medical research*, vol. 134, no. 4, pp. 463–469, 10 2011.
- [134] A. J. Ocon, M. S. Medow, I. Taneja, D. Clarke, and J. M. Stewart, "Decreased upright cerebral blood flow and cerebral autoregulation in normocapnic postural tachycardia syndrome," *American Journal of Physiology - Heart and Circulatory Physiology*, vol. 297, no. 2, pp. 664–673, 2009.
- [135] P. M. Patel and J. C. Drummond, *Cerebral Physiology and the Effects of Anesthetic Drugs*, eighth ed. Elsevier Inc., 2010. [Online]. Available: <http://dx.doi.org/10.1016/B978-0-7020-5283-5.00017-5>
- [136] M. K. Loushin, "The effects of anesthetic agents on cardiac function," *Handbook of Cardiac Anatomy, Physiology, and Devices*, pp. 171–180, 2005.
- [137] S. Strebel, A. M. Lam, B. Matta, T. S. Mayberg, R. Aaslid, and D. W. Newell, "Dynamic and Static Cerebral Autoregulation during Isoflurane, Desflurane, and Propofol Anesthesia," *Anesthesiology*, vol. 83, no. 7, pp. 66–76, 1995. [Online]. Available: <http://anesthesiology.pubs.asahq.org/article.aspx?articleid=1951112>
- [138] A. Dagal and A. M. Lam, "Cerebral autoregulation and anesthesia," *Current Opinion in Anaesthesiology*, vol. 22, no. 5, pp. 547–552, 2009.
- [139] W. M. Armstead, "Cerebral Blood Flow Autoregulation and Dysautoregulation," *Anesthesiol Clin.*, vol. 34, no. 3, pp. 465–477, 2016. [Online]. Available: <http://doi.org/10.1016/j.anclin.2016.04.002>
- [140] D. L. de Jong, T. Tarumi, J. Liu, R. Zhang, and J. A. Claassen, "Lack of linear correlation between dynamic and steady-state cerebral autoregulation," *Journal of Physiology*, vol. 595, no. 16, pp. 5623–5636, 2017.
- [141] F. P. Tiecks, A. M. Lam, R. Aaslid, and D. W. Newell, "Comparison of Static and Dynamic Cerebral Autoregulation Measurements," *Stroke*, vol. 26, no. 6, pp. 1014 LP – 1019, 6 1995. [Online]. Available: <http://stroke.ahajournals.org/cgi/doi/10.1161/01.STR.26.6.1014><http://stroke.ahajournals.org/content/26/6/1014.abstract>
- [142] T. Numan, A. R. Bain, R. L. Hoiland, J. D. Smirl, N. C. Lewis, and P. N. Ainslie, "Static autoregulation in humans: a review and reanalysis," *Medical engineering & physics*, vol. 36, no. 11, pp. 1487–1495, 2014. [Online]. Available: <http://dx.doi.org/10.1016/j.medengphy.2014.08.001>
- [143] L. Xiong, X. Liu, T. Shang, P. Smielewski, J. Donnelly, Z.-n. N. Guo, Y. Yang, T. Leung, M. Czosnyka, R. Zhang, J. Liu, K. S. Wong, K. Sing, L. Vol, L. Xiong, X. Liu, T. Shang, P. Smielewski, J. Donnelly, Z.-n. N. Guo, Y. Yang, T. Leung, M. Czosnyka, R. Zhang, J. Liu, and K. S. Wong, "Impaired cerebral autoregulation: Measurement and application to stroke," *Journal of Neurology, Neurosurgery and Psychiatry*, vol. 88, no. 6, pp. 520–

531, 2017.

- [144] R. Aaslid, K. F. Lindegaard, W. Sorteberg, and H. Nornes, "Cerebral autoregulation dynamics in humans," *Stroke*, vol. 20, no. 1, pp. 45–52, 1989.
- [145] C. A. Giller, "The Frequency-Dependent Behavior of Cerebral Autoregulation," *Neurosurgery*, vol. 27, no. 3, pp. 362–368, 1990. [Online]. Available: <https://doi.org/10.1227/00006123-199009000-00004https://academic.oup.com/neurosurgery/article-abstract/27/3/362/2753586?redirectedFrom=fulltext>
- [146] R. Zhang, J. H. Zuckerman, C. A. Giller, and B. D. Levine, "Transfer function analysis of dynamic cerebral autoregulation in humans," *American Journal of Physiology-Heart and Circulatory Physiology*, vol. 274, no. 1, pp. H233–H241, 1 1998. [Online]. Available: <https://www.physiology.org/doi/10.1152/ajpheart.1998.274.1.H233>
- [147] A. A. Birch, M. J. Dirnhuber, R. Hartley-Davies, F. Iannotti, and G. Neil-Dwyer, "Assessment of Autoregulation by Means of Periodic Changes in Blood Pressure," *Stroke*, vol. 26, no. 5, pp. 834–837, 1995.
- [148] A. S. Meel-van den Abeelen, D. M. Simpson, L. J. Y. Wang, C. H. Slump, R. Zhang, T. Tarumi, C. A. Rickards, S. Payne, G. D. Mitsis, K. Kostoglou, V. Marmarelis, D. Shin, Y.-c. C. Tzeng, P. N. Ainslie, E. Gommer, M. Müller, A. C. Dorado, P. Smielewski, B. Yelicich, C. Puppo, X. Liu, M. Czosnyka, C.-y. Y. Wang, V. Novak, R. B. Panerai, and J. A. H. R. Claassen, "Between-centre variability in transfer function analysis, a widely used method for linear quantification of the dynamic pressure-flow relation: The CARNet study," *Medical Engineering and Physics*, vol. 36, no. 5, pp. 620–627, 2014. [Online]. Available: <http://dx.doi.org/10.1016/j.medengphy.2014.02.002>
- [149] J. A. Claassen, A. S. Meel-van den Abeelen, D. M. Simpson, R. B. Panerai, and international Cerebral Autoregulation Research Network (CARNet), "Transfer function analysis of dynamic cerebral autoregulation: A white paper from the International Cerebral Autoregulation Research Network." *Journal of cerebral blood flow and metabolism : official journal of the International Society of Cerebral Blood Flow and Metabolism*, vol. 36, no. 4, pp. 665–80, 2016. [Online]. Available: <http://www.ncbi.nlm.nih.gov/pubmed/26782760>
- [150] C. D. Fraser, K. M. Brady, C. J. Rhee, R. B. Easley, K. Kibler, P. Smielewski, M. Czosnyka, D. W. Kaczka, D. B. Andropoulos, C. Rusin, C. D. F. Iii, K. M. Brady, C. J. Rhee, R. B. Easley, K. Kibler, P. Smielewski, M. Czosnyka, D. W. Kaczka, D. B. Andropoulos, and C. Rusin, "The frequency response of cerebral autoregulation." *Journal of applied physiology (Bethesda, Md. : 1985)*, vol. 115, no. May 2013, pp. 52–6, 2013. [Online]. Available: <http://www.ncbi.nlm.nih.gov/pubmed/23681909>
- [151] J. M. Kainerstorfer, A. Sassaroli, K. T. Tgavalekos, and S. Fantini, "Cerebral autoregulation in the microvasculature measured with near-infrared spectroscopy," *Journal of Cerebral Blood Flow & Metabolism*, vol. 35, no. 6, pp. 959–966, 2015. [Online]. Available: <http://www.nature.com/doi/10.1038/jcbfm.2015.5>
- [152] R. L. Grubb, "Effects of increased intracranial pressure on cerebral blood volume, blood flow, and oxygen utilization in monkeys," *Journal of neurosurgery*, vol. 43, no. 4, pp.

385–398, 1975.

- [153] W. Xu, P. Gerety, T. Aleman, J. Swanson, and J. Taylor, “Noninvasive methods of detecting increased intracranial pressure,” *Child’s Nervous System*, vol. 32, no. 8, pp. 1371–1386, 8 2016. [Online]. Available: <http://link.springer.com/10.1007/s00381-016-3143-x>
- [154] M. Harary, R. G. Dolmans, and W. B. Gormley, “Intracranial pressure monitoring—review and avenues for development,” *Sensors (Switzerland)*, vol. 18, no. 2, pp. 3–7, 2018.
- [155] S. Fantini, A. Sassaroli, K. T. Tgavalekos, and J. Kornbluth, “Cerebral blood flow and autoregulation: current measurement techniques and prospects for noninvasive optical methods,” *Neurophotonics*, vol. 3, no. 3, p. 31411, 2016. [Online]. Available: <http://neurophotonics.spiedigitallibrary.org/article.aspx?doi=10.1117/1.NPh.3.3.031411>
<http://dx.doi.org/10.1117/1.NPh.3.3.031411>
- [156] J.-p. P. A. H. Jantzen, “Prevention and treatment of intracranial hypertension,” *Best Practice and Research: Clinical Anaesthesiology*, vol. 21, no. 4, pp. 517–538, 2007.
- [157] R. B. Panerai, S. L. Dawson, and J. F. Potter, “Linear and nonlinear analysis of human dynamic cerebral autoregulation,” *American Journal of Physiology - Heart and Circulatory Physiology*, vol. 277, no. 3 Pt 2, pp. H1089–H1099, 1999.
- [158] R. B. Panerai, “Nonstationarity of dynamic cerebral autoregulation,” *Medical Engineering and Physics*, vol. 36, no. 5, pp. 576–584, 2014. [Online]. Available: <http://dx.doi.org/10.1016/j.medengphy.2013.09.004>
- [159] M. Czosnyka, P. Smielewski, P. Kirkpatrick, R. J. Laing, D. Menon, and J. D. Pickard, “Continuous assessment of the cerebral vasomotor reactivity in head injury.” *Neurosurgery*, vol. 41, no. 1, pp. 11–19, 7 1997.
- [160] R. Steinmeier, R. P. Hofmann, C. Bauhuf, U. Hübner, and R. Fahlbusch, “Continuous cerebral autoregulation monitoring by cross-correlation analysis,” *Journal of Neurotrauma*, vol. 19, no. 10, pp. 1127–1138, 2002.
- [161] P. M. Lewis, P. Smielewski, J. D. Pickard, and M. Czosnyka, “Dynamic cerebral autoregulation: Should intracranial pressure be taken into account?” *Acta Neurochirurgica*, vol. 149, no. 6, pp. 549–555, 2007. [Online]. Available: <http://search.proquest.com/docview/755004934?accountid=9902>
- [162] C. Zweifel, G. Castellani, M. Czosnyka, A. Helmy, A. Manktelow, E. Carrera, K. M. Brady, P. J. Hutchinson, D. K. Menon, J. D. Pickard, and P. Smielewski, “Noninvasive monitoring of cerebrovascular reactivity with near infrared spectroscopy in head-injured patients,” *J Neurotrauma*, vol. 27, no. 11, pp. 1951–1958, 2010. [Online]. Available: <http://www.ncbi.nlm.nih.gov/pubmed/20812789>
http://online.liebertpub.com/doi/abs/10.1089/neu.2010.1388?url%7B_%7Dver=Z39.88-2003%7B&%7Ddrfr%7B_%7Ddid=ori:rid:crossref.org%7B&%7Ddrfr%7B_%7Ddat=cr%7B_%7Dpub=pubmed%7B&%7Dhttp://www.ncbi.nlm.nih.gov/pubmed
- [163] K. M. Brady and C. M. Mery, “Cerebral autoregulation: Making sense of the nonsensical,” *Journal of Thoracic and Cardiovascular Surgery*, vol. 154, no. 3, pp.

- 1045–1046, 2017. [Online]. Available: <http://dx.doi.org/10.1016/j.jtcvs.2017.05.074>
- [164] M. Nitzan, A. Romem, and R. Koppel, “Pulse oximetry: Fundamentals and technology update,” *Medical Devices: Evidence and Research*, vol. 7, no. 1, pp. 231–239, 2014.
- [165] S. Fantini, A. Ruesch, and J. M. Kainerstorfer, “Noninvasive Optical Studies of the Brain: Contributions From Systemic Physiology,” *Neurophotonics and Biomedical Spectroscopy*, pp. 25–52, 1 2019. [Online]. Available: <https://www.sciencedirect.com/science/article/pii/B9780323480673000020>
- [166] I. J. Bigio and S. Fantini, *Quantitative Biomedical Optics: Theory, Methods, and Applications*, 1st ed. New York, NY, USA: Cambridge University Press, 2016.
- [167] M. I. Mishchenko, *Electromagnetic Scattering by Particles and Particle Groups: An Introduction*. New York: Cambridge University Press, 2014. [Online]. Available: https://books.google.com/books?id=oy84AwAAQBAJhttps://www.researchgate.net/publication/325376252_Electromagnetic_Scattering_by_Particles_and_Particle_Groups_An_Introduction
- [168] W. Cheong, S. Prahl, and A. Welch, “A review of the optical properties of biological tissues,” *IEEE Journal of Quantum Electronics*, vol. 26, no. 12, pp. 2166–2185, 1990. [Online]. Available: <http://ieeexplore.ieee.org/document/64354/>
- [169] J. S. You, C. K. Hayakawa, and V. Venugopalan, “Frequency domain photon migration in the δ -P1 approximation: Analysis of ballistic, transport, and diffuse regimes,” *Physical Review E - Statistical, Nonlinear, and Soft Matter Physics*, vol. 72, no. 2, pp. 22–25, 2005.
- [170] J. B. Fishkin, S. Fantini, M. J. vandeVen, and E. Gratton, “Gigahertz photon density waves in a turbid medium: Theory and experiments,” *Physical Review E - Statistical Physics, Plasmas, Fluids, and Related Interdisciplinary Topics*, vol. 53, no. 3, pp. 2307–2319, 1996.
- [171] F. Martelli, M. Bassani, L. Alianelli, L. Zangheri, and G. Zaccanti, “Accuracy of the diffusion equation to describe photon migration through an infinite medium: Numerical and experimental investigation,” *Physics in Medicine and Biology*, vol. 45, no. 5, pp. 1359–1373, 2000.
- [172] F. Jobsis, “Noninvasive, infrared monitoring of cerebral and myocardial oxygen sufficiency and circulatory parameters,” *Science*, vol. 198, no. 4323, pp. 1264–1267, 12 1977. [Online]. Available: <https://www.sciencemag.org/lookup/doi/10.1126/science.929199>
- [173] A. Sassaroli and S. Fantini, “Comment on the modified Beer–Lambert law for scattering media,” *Physics in Medicine and Biology*, vol. 49, no. 14, pp. N255–N257, 2004. [Online]. Available: <http://stacks.iop.org/0031-9155/49/i=14/a=N07?key=crossref.6f4c20272e6aff52ece7fc4cbcecacbb>
- [174] J. Steinbrink, H. Wabnitz, H. Obrig, A. Villringer, and H. Rinneberg, “Determining changes in NIR absorption using a layered model of the human head,” *Physics in Medicine and Biology*, vol. 46, no. 3, pp. 879–896, 2001.
- [175] A. Torricelli, A. Pifferi, L. Spinelli, R. Cubeddu, F. Martelli, S. Del Bianco, and G. Za-

- ccanti, “Time-resolved reflectance at null source-detector separation: Improving contrast and resolution in diffuse optical imaging,” *Physical Review Letters*, vol. 95, no. 7, pp. 2–5, 2005.
- [176] S. Fantini, M. A. Franceschini, J. B. Fishkin, B. Barbieri, and E. Gratton, “Quantitative determination of the absorption spectra of chromophores in strongly scattering media: a light-emitting-diode based technique,” *Applied Optics*, vol. 33, no. 22, p. 5204, 1994.
- [177] F. Bevilacqua, A. J. Berger, A. E. Cerussi, D. Jakubowski, and B. J. Tromberg, “Broadband absorption spectroscopy in turbid media by combined frequency-domain and steady-state methods,” *Applied Optics*, vol. 39, no. 34, p. 6498, 2000.
- [178] A. Cerussi, N. Shah, D. Hsiang, A. Durkin, J. Butler, and B. J. Tromberg, “In vivo absorption, scattering, and physiologic properties of 58 malignant breast tumors determined by broadband diffuse optical spectroscopy,” *Journal of Biomedical Optics*, vol. 11, no. 4, p. 044005, 2006.
- [179] S. R. Arridge, M. Cope, and D. T. Delpy, “The theoretical basis for the determination of optical pathlengths in tissue: Temporal and frequency analysis,” *Physics in Medicine and Biology*, vol. 37, no. 7, pp. 1531–1560, 1992.
- [180] S. Fantini, “Dynamic model for the tissue concentration and oxygen saturation of hemoglobin in relation to blood volume, flow velocity, and oxygen consumption: Implications for functional neuroimaging and coherent hemodynamics spectroscopy (CHS),” *NeuroImage*, vol. 85, pp. 202–221, 2014. [Online]. Available: <http://dx.doi.org/10.1016/j.neuroimage.2013.03.065>
- [181] —, “A new hemodynamic model shows that temporal perturbations of cerebral blood flow and metabolic rate of oxygen cannot be measured individually using functional near-infrared spectroscopy,” *Physiological Measurement*, vol. 35, no. 1, pp. N1–N9, 1 2014.
- [182] S. Fantini, D. Hueber, M. a. Franceschini, E. Gratton, W. Rosenfeld, P. G. Stubblefield, D. Maulik, and M. R. Stankovic, “Non-invasive optical monitoring of the newborn piglet brain using continuous-wave and frequency-domain spectroscopy,” *Physics in medicine and biology*, vol. 44, no. 6, pp. 1543–1563, 1999.
- [183] S. Prahl, “Optical Absorption of Hemoglobin,” 1999. [Online]. Available: <https://omlc.org/spectra/hemoglobin/index.html>
- [184] D. A. Boas and A. G. Yodh, “Spatially varying dynamical properties of turbid media probed with diffusing temporal light correlation,” *J. Opt. Soc. Am.*, vol. 14, no. 1, pp. 192–215, 1997.
- [185] R. C. Mesquita, T. Durduran, G. Yu, E. M. Buckley, M. N. Kim, C. Zhou, R. Choe, U. Sunar, and A. G. Yodh, “Direct measurement of tissue blood flow and metabolism with diffuse optics,” *Philosophical Transactions of the Royal Society A: Mathematical, Physical and Engineering Sciences*, vol. 369, no. 1955, pp. 4390–4406, 2011.
- [186] T. Durduran and A. G. Yodh, “Diffuse correlation spectroscopy for non-invasive, micro-vascular cerebral blood flow measurement,” *NeuroImage*, vol. 85, p. 5163, 2014. [Online]. Available: <http://dx.doi.org/10.1016/j.neuroimage.2013.06.017>

- [187] B. J. Ackerson, R. L. Dougherty, N. M. Reguigui, and U. Nobbmann, "Correlation transfer - Application of radiative transfer solution methods to photon correlation problems," *Journal of Thermophysics and Heat Transfer*, vol. 6, no. 4, pp. 577–588, 10 1992. [Online]. Available: <https://arc.aiaa.org/doi/10.2514/3.11537>
- [188] R. Dougherty, B. Ackerson, N. Reguigui, F. Dorri-Nowkooorani, and U. Nobbmann, "Correlation transfer: Development and application," *Journal of Quantitative Spectroscopy and Radiative Transfer*, vol. 52, no. 6, pp. 713–727, 12 1994. [Online]. Available: <https://linkinghub.elsevier.com/retrieve/pii/002240739490037X>
- [189] R. A. J. Groenhuis, H. A. Ferwerda, and J. J. Ten Bosch, "Scattering and absorption of turbid materials determined from reflection measurements 1: Theory," *Applied Optics*, vol. 22, no. 16, p. 2456, 1983.
- [190] D. A. Boas and A. K. Dunn, "Laser speckle contrast imaging in biomedical optics," *Journal of Biomedical Optics*, vol. 15, no. 1, p. 011109, 2010.
- [191] W. Heeman, W. Steenbergen, G. M. van Dam, and E. C. Boerma, "Clinical applications of laser speckle contrast imaging: a review," *Journal of Biomedical Optics*, vol. 24, no. 08, p. 1, 2019.
- [192] P.-A. Lemieux and D. J. Durian, "Investigating non-Gaussian scattering processes by using nth -order intensity correlation functions," *Journal of the Optical Society of America A*, vol. 16, no. 7, p. 1651, 1999.
- [193] E. M. Buckley, N. M. Cook, T. Durduran, M. N. Kim, C. Zhou, R. Choe, G. Yu, S. Schultz, C. M. Sehgal, D. J. Licht, P. H. Arger, M. E. Putt, H. H. Hurt, and A. G. Yodh, "Cerebral hemodynamics in preterm infants during positional intervention measured with diffuse correlation spectroscopy and transcranial Doppler ultrasound," *Optics Express*, vol. 17, no. 15, p. 12571, 2009.
- [194] G. Yu, T. F. Floyd, T. Durduran, C. Zhou, J. Wang, J. A. Detre, and A. G. Yodh, "Validation of diffuse correlation spectroscopy for muscle blood flow with concurrent arterial spin labeled perfusion MRI," *Optics Express*, vol. 15, no. 3, p. 1064, 2007.
- [195] S. A. Carp, G. P. Dai, D. A. Boas, M. A. Franceschini, and Y. R. Kim, "Validation of diffuse correlation spectroscopy measurements of rodent cerebral blood flow with simultaneous arterial spin labeling MRI; towards MRI-optical continuous cerebral metabolic monitoring," *Biomedical Optics Express*, vol. 1, no. 2, p. 553, 2010.
- [196] E. M. Buckley, A. B. Parthasarathy, P. E. Grant, M. A. Franceschini, A. G. Yodh, and M. A. Franceschini, "Diffuse correlation spectroscopy for measurement of cerebral blood flow: future prospects," *Neurophotonics*, vol. 1, no. 1, p. 011009, 2014. [Online]. Available: <http://neurophotonics.spiedigitallibrary.org/article.aspx?doi=10.1117/1.NPh.1.1.011009>
- [197] A. Kampfl, B. Pfausler, D. Denchev, H. P. Jaring, and E. Schmutzhard, "Near infrared spectroscopy (NIRS) in patients with severe brain injury and elevated intracranial pressure. A pilot study." *Acta neurochirurgica. Supplement*, vol. 70, pp. 112–114, 1997.
- [198] A. Ruesch, S. Schmitt, J. Yang, M. A. Smith, and J. M. Kainerstorfer, "Fluctuations in intracranial pressure can be estimated non-invasively using near-infrared spectroscopy

in non-human primates,” *Journal of Cerebral Blood Flow & Metabolism*, vol. 0, no. 0, p. 0271678X1989135, 11 2019. [Online]. Available: <https://doi.org/10.1177/0271678X19891359><http://journals.sagepub.com/doi/10.1177/0271678X19891359>

- [199] A. Ruesch, J. Yang, S. Nelson, M. A. Smith, and J. M. Kainerstorfer, “Frequency dependent hemodynamic response to intracranial pressure changes,” *Optical Tomography and Spectroscopy of Tissue XIII*, vol. 10874, no. March, p. 50, 3 2019. [Online]. Available: <https://www.spiedigitallibrary.org/conference-proceedings-of-spie/10874/2510113/Frequency-dependent-hemodynamic-response-to-intracranial-pressure-changes/10.1117/12.2510113.full>
- [200] A. Ruesch, S. Schmitt, J. Yang, D. Acharya, J. Rakkar, M. S. Wolf, M. M. McDowell, E. C. Tyler-Kabara, R. S. B. Clark, M. A. Smith, and others, “Intracranial pressure estimated non-invasively in non-human primates and pediatric critical care (Conference Presentation),” in *Neural Imaging and Sensing 2020*, vol. 11226. International Society for Optics and Photonics, 2020, p. 112261J.
- [201] A. Ruesch, J. Yang, S. Schmitt, D. Acharya, M. A. Smith, and J. M. Kainerstorfer, “Estimating intracranial pressure using pulsatile cerebral blood flow measured with diffuse correlation spectroscopy,” *Biomedical Optics Express*, vol. 11, no. 3, p. 1462, 2020. [Online]. Available: <https://doi.org/10.1364/BOE.386612>
- [202] A. Ruesch, S. Schmitt, M. A. Smith, and J. M. Kainerstorfer, “Combined NIRS and DCS measurements of cerebral hemodynamics during intracranial and blood pressure changes (Conference Presentation),” in *Dynamics and Fluctuations in Biomedical Photonics XV*, vol. 10493. International Society for Optics and Photonics, 2018, p. 104930H.
- [203] A. Ruesch, J. Yang, D. Acharya, S. Schmitt, D. Issar, M. A. Smith, and J. M. Kainerstorfer, “Diffuse correlation spectroscopy for intracranial pressure estimation through cardiac pulse waveform analysis,” in *European Conference on Biomedical Optics*. Optical Society of America, 2019, p. 11074_20.
- [204] T. W. Parks and J. H. McClellan, “Chebyshev Approximation for Nonrecursive Digital Filters with Linear Phase,” *IEEE Transactions on Circuit Theory*, vol. 19, no. 2, pp. 189–194, 1972.
- [205] R. Kohavi, “A Study of Cross-Validation and Bootstrap for Accuracy Estimation and Model Selection,” in *International Joint Conference on Artificial Intelligence (IJCAI)*. Morgan Kaufmann, 1995, pp. 1137–1143.
- [206] Z. Drmac, S. Gugercin, and C. Beattie, “Quadrature-Based Vector Fitting: Implications For H2 System Approximation,” *Journal on Scientific Computing*, vol. 37, no. 2, pp. A625–A652, 3 2014. [Online]. Available: <http://arxiv.org/abs/1403.4655><http://dx.doi.org/10.1137/14096151><http://arxiv.org/abs/1403.4655><http://dx.doi.org/10.1137/14096151>
- [207] R. A. Weerakkody, M. Czosnyka, C. Zweifel, G. Castellani, P. Smielewski, K. Brady, J. D. Pickard, and Z. Czosnyka, “Near Infrared Spectroscopy as Possible Non-invasive Monitor of Slow Vasogenic ICP Waves,” *Acta Neurochirurgica Supplementum*, vol. 114, pp. 181–185, 2012. [Online]. Available: <http://www.springerlink.com/index/10.1007/>

- [208] G. D. Mitsis, M. J. Poulin, P. A. Robbins, and V. Z. Marmarelis, “Nonlinear modeling of the dynamic effects of arterial pressure and CO₂ variations on cerebral blood flow in healthy humans,” *IEEE Transactions on Biomedical Engineering*, vol. 51, no. 11, pp. 1932–1943, 11 2004.
- [209] S. Fantini, M.-A. Franceschini, J. S. Maier, S. A. Walker, B. B. Barbieri, and E. Gratton, “Frequency-domain multichannel optical detector for noninvasive tissue spectroscopy and oximetry,” *Optical Engineering*, vol. 34, no. 1, p. 32, 1995. [Online]. Available: <http://opticalengineering.spiedigitallibrary.org/article.aspx?doi=10.1117/12.183988%5Cnhttp://www.ncbi.nlm.nih.gov/pubmed/133>
- [210] D. J. Davies, Z. Su, M. T. Clancy, S. J. E. Lucas, H. Dehghani, A. Logan, and A. Belli, “Near-Infrared Spectroscopy in the Monitoring of Adult Traumatic Brain Injury: A Review,” *Journal of Neurotrauma*, vol. 44, no. 0, p. 150417112024001, 2015. [Online]. Available: <http://online.liebertpub.com/doi/10.1089/neu.2014.3748>
- [211] X. Hu and M. Bergsneider, “Morphological clustering and analysis of intracranial pressure pulses (mocaip),” *IEEE Transactions on Biomedical Engineering*, vol. 56, no. 3, pp. 696–705, 2009. [Online]. Available: <https://www.google.com/patents/US20110201961>
- [212] E. Carrera, D.-J. Kim, G. Castellani, C. Zweifel, Z. Czosnyka, M. Kaspruwicz, P. Smielewski, J. D. Pickard, and M. Czosnyka, “What Shapes Pulse Amplitude of Intracranial Pressure?” *Journal of Neurotrauma*, vol. 27, no. 2, pp. 317–324, 2010. [Online]. Available: <http://www.liebertonline.com/doi/abs/10.1089/neu.2009.0951>
- [213] A. Ruesch, J. Yang, D. Acharya, S. Schmitt, D. Issar, M. A. Smith, and J. M. Kainerstorfer, “Diffuse correlation spectroscopy for intracranial pressure estimation through cardiac pulse waveform analysis,” in *Diffuse Optical Spectroscopy and Imaging VII*, H. Dehghani and H. Wabnitz, Eds., vol. 11074, no. July. SPIE, 2019, p. 20. [Online]. Available: <https://www.spiedigitallibrary.org/conference-proceedings-of-spie/11074/2527187/Diffuse-correlation-spectroscopy-for-intracranial-pressure-estimation-through-cardiac-pulse/10.1117/12.2527187.full>
- [214] F. Pedregosa, G. Varoquaux, A. Gramfort, V. Michel, B. Thirion, O. Grisel, and others, “Scikit-learn: Machine Learning in {P}ython,” *Journal of Machine Learning Research*, vol. 12, pp. 2825–2830, 2011.
- [215] A. Criminisi and J. Shotton, *Decision forests for computer vision and medical image analysis*. Springer, 2 2013. [Online]. Available: <http://research.microsoft.com/apps/pubs/default.aspx?id=185223>
- [216] L. E. O. Breiman, “Random Forests,” *Machine Learning*, vol. 45, no. 1, pp. 5–32, 2001. [Online]. Available: <http://dx.doi.org/10.1023/A%3A1010933404324http://link.springer.com/article/10.1023/A:1010933404324>
- [217] S. Wager, T. Hastie, and B. Efron, “Confidence Intervals for Random Forests: The Jackknife and the Infinitesimal Jackknife,” *Journal of Machine Learning Research*, vol. 15, pp. 1625–1651, 2014. [Online]. Available: <http://jmlr.org/papers/volume15/wager14a/wager14a.pdf>

- [218] G. V. Varsos, A. G. Kolias, P. Smielewski, K. M. Brady, V. G. Varsos, P. J. Hutchinson, J. D. Pickard, and M. Czosnyka, “A noninvasive estimation of cerebral perfusion pressure using critical closing pressure,” *Journal of Neurosurgery*, vol. 123, no. 3, pp. 638–648, 9 2015. [Online]. Available: <http://thejns.org/doi/10.3171/2014.10.JNS14613>
- [219] D. Cardim, C. Robba, M. Bohdanowicz, J. Donnelly, B. Cabella, X. Liu, M. Cabeleira, P. Smielewski, B. Schmidt, and M. Czosnyka, “Non-invasive Monitoring of Intracranial Pressure Using Transcranial Doppler Ultrasonography: Is It Possible?” *Neurocritical Care*, vol. 25, no. 3, pp. 473–491, 12 2016. [Online]. Available: https://www.ncbi.nlm.nih.gov/pmc/articles/PMC5138275/pdf/12028_2016_Article_258.pdf